Short-Pulse and Long-Pulse PLL-based Frequency Stabilization of MW-Class Gyrotrons with Diode-Type MIG

Zur Erlangung des akademischen Grades eines

DOKTORS DER INGENIEURWISSENSCHAFTEN
(Dr.-Ing.)

von der KIT-Fakultät für
Elektrotechnik und Informationstechnik
des Karlsruher Instituts für Technologie (KIT)

genehmigte

DISSERTATION

von

M.Sc. Laurent Krier
geb. in Luxembourg

Tag der mündlichen Prüfung:	07.03.2024
Hauptreferent:	Prof. Dr.-Ing. John Jelonnek
Korreferent:	Prof. Dr. Robert Wolf

Kurzfassung

Gyrotrons sind Elektronenvakuumröhren, die Millimeterwellen im Frequenzbereich von 30 GHz bis 200 GHz mit Ausgangsleistungen im Megawattbereich (MW) erzeugen. Aufgrund variabler Betriebsbedingungen und Rauschen schwankt die Ausgangsfrequenz von Hochleistungsgyrotrons, was eine Herausforderung für Anwendungen darstellt, die präzise und stabile Betriebsfrequenzen erfordern. Beispiele hierfür sind die Plasmadiagnostik mittels kollektiver Thomson-Streuung (CTS) und die direkte Ionenheizung mit Schwebungswellen. Die Schwebungswellen werden dabei aus der Differenzfrequenz, welche der Ionenzyklotronfrequenz entspricht, von zwei Gyrotrons erzeugt. In dieser Arbeit wird gezeigt, dass die Frequenz eines Hochleistungsgyrotrons mit einem Elektronenstrahlerzeuger in Diodenausführung mittels einer Phasenregelschleife (PLL) stabilisiert werden kann.

Die Ausgangsfrequenz des Gyrotrons wird durch Änderung der Beschleunigungsspannung gesteuert, die zwischen der Anode und der Kathode des Elektronenstrahlerzeugers anliegt. Für einen festen Arbeitspunkt wird die Frequenzabhängigkeit von der Beschleunigungsspannung linearisiert und das Gyrotron wird als spannungsgesteuerter Oszillator betrachtet. Es wird ein PLL-System entwickelt, das die Frequenz über die Beschleunigungsspannung regelt. Das PLL-System wird experimentell an den Gyrotrons der Elektronen-Zyklotron-Resonanzheizung (ECRH) am Wendelstein 7-X (W7-X) Stellarator demonstriert.

Bei Experimenten mit langen Pulsen (> 5 s) wird die Gyrotronfrequenz erfolgreich zwischen 1 s bis zum Ende des Pulses stabilisiert. Das PLL-System verringert die Frequenzveränderungen im MHz-Bereich, welche im freilaufenden Betrieb beobachtet werden, erheblich. Das Frequenzspektrum weist ein ausgeprägtes

Maximum bei der eingestellten Frequenz auf und es wird eine volle -20 dB Bandbreite von unter 100 kHz erreicht. Das verbleibende Frequenzrauschen, das auf Schwankungen der Kathodenspannungsversorgung zurückzuführen ist, erscheint als Seitenbänder bei 3,3 kHz und 135 kHz neben der Hauptfrequenz. Im Gegensatz dazu erstreckt sich das Frequenzspektrum ohne die Frequenzstabilisierung über ein Frequenzband mit einer vollen -20 dB-Bandbreite über 1 MHz aus, ohne dass es ein deutlich erkennbares Maximum bei einer Frequenz gibt.

Die CTS-Diagnostik am W7-X Stellarator benötigt einen frequenzstabilisierten Betrieb eines 140 GHz ECRH-Gyrotrons bei 174 GHz für eine Pulsdauer von 9 ms. Der Betrieb bei 174 GHz wird theoretisch und experimentell untersucht. In den Experimenten wird eine Ausgangsleistung von 300 kW bei 174 GHz erreicht. Die größte Herausforderungen für eine Frequenzstabilisierung bei einer Pulsdauer von 9 ms stellt der 30 MHz Frequenzabfall dar, der durch die Ausdehnung des Resonators aufgrund von Erwärmung und durch die Neutralisierung der Elektronenstrahlraumladung entsteht. Das PLL-System wirkt dem Frequenzabfall erfolgreich entgegen. Darüber hinaus ist es möglich mit dem PLL-Systems eine gewünschte Gyrotronfrequenz präzise einzustellen und genau an das Kerbfilters des CTS-Empfängers anzupassen.

Abstract

Gyromonotron oscillators, also known as gyrotrons, are electron vacuum tubes capable of generating millimeter-wave (mm-wave) radiation in the frequency range from 30 GHz up to 200 GHz with output power levels in the megawatt (MW) range. The output frequency of MW-class gyrotron fluctuates due to varying operating conditions and noise, posing challenges to applications which require well defined and stable operating frequencies. Examples are the Collective Thomson Scattering (CTS) diagnostic and direct ion heating with beat waves generated by two gyrotrons. In this thesis, a novel approach is presented, demonstrating the feasibility of stabilizing the frequency of MW-class gyrotrons with a diode-type Magnetron Injection Gun (MIG) by using a Phase-Locked Loop (PLL) system.

The gyrotron output frequency is controlled by changing the accelerating voltage, which is applied between the anode and cathode of the diode-type MIG. For a fixed operating point, the frequency dependence on the accelerating voltage is linearized, and the gyrotron is considered as Voltage Controlled Oscillator (VCO). A PLL system is developed that controls the accelerating voltage with the high-voltage body power supply, and its capabilities are experimentally demonstrated with the Electron Cyclotron Resonance Heating (ECRH) gyrotrons at the Wendelstein 7-X (W7-X) stellarator.

In long-pulse experiments (> 5 s), the gyrotron frequency is successfully stabilized after 1 s until the end of the pulse. The PLL system significantly reduces long-term frequency drifts in the MHz range observed in the free-running operation, where no PLL system is implemented. The frequency spectrum has a distinct main peak at the set frequency, and a full -20 dB bandwidth of below 100 kHz is achieved. The remaining short-term frequency noise, attributed to cathode power supply

fluctuations, appears as sidebands at 3.3 kHz and 135 kHz from the main peak. In contrast, without the frequency stabilization, the gyrotron frequency spectrum spreads over a band of frequencies with a full -20 dB bandwidth higher than 1 MHz, lacking a distinct peak at a single frequency.

To demonstrate its viability, the PLL system is implemented for the CTS diagnostic at the W7-X stellarator, which requires a frequency stabilized operation of a 140 GHz ECRH gyrotron at 174 GHz for a pulse duration of 9 ms. The operation at 174 GHz is theoretically and experimentally investigated, and an output power of 300 kW is achieved at 174 GHz in the experiments. Overcoming main challenges related to short-pulse frequency stabilization, the developed PLL system effectively counteracts the 30 MHz frequency drift observed for a duration of 9 ms, caused by cavity expansion due to heating and by electron beam space charge neutralization. In addition, the precision of the PLL system in matching the gyrotron frequency to the notch filter of the CTS receiver allows to reduce the notch filter bandwidth, which improves the CTS measurements.

Contents

Abbreviations

ADC	Analog-to-Digital Converter
CMC	Compensating Main Coil
CTS	Collective Thomson Scattering
CVD	Chemical Vapor Deposition
CW	Continuous Wave
DC	Direct Current
ECCD	Electron Cyclotron Current Drive
ECRH	Electron Cyclotron Resonance Heating
FADIS	FAst DIrectional Switch
FFT	Fast Fourier Transform
FPGA	Field-Programmable Gate Array
FTA	Frequency Time Analyzer
GTC	Gun Trim Coil
HMC	High-field Main Coil
HPS	Hard Processor System
IBW	Ion Bernstein Wave
ICRH	Ion Cyclotron Resonance Heating
IF	Intermediate Frequency
IHM	Institute for Pulsed Power and Microwave Technology
IPP	Max-Planck-Institute for Plasma Physics
KIT	Karlsruhe Insitute of Technology
LMC	Lower Main Coil
LNA	Low Noise Amplifier
LO	Local Oscillator
LP	Long-Pulse

LPL	Long-Pulse Load
MIG	Magnetron Injection Gun
mm-wave	millimeter-wave
NBI	Neutral Beam Injection
OP	Operational Phase
PD	Phase Detector
PFD	Phase Frequency Detector
PI filter	Proportional-Integral filter
PLL	Phase-Locked Loop
PS	Power Supply
PSM	Pulse Step Modulation
SNR	Signal-to-Noise Ratio
SoC	System on Chip
SP	Short-Pulse
SPL	Short-Pulse Load
TE	Transverse Electric
TEM	Transverse Electric Magnetic
TM	Transverse Magnetic
UMC	Upper Main Coil
VCO	Voltage Controlled Oscillator
W7-X	Wendelstein 7-X

Symbols

Latin Letters

b	Magnetic compression ratio
$\boldsymbol{B}$	Magnetic field vector
B	Magnetic field strength
B_{cav}	Magnetic field strength at cavity center
c	Speed of light in vacuum
d_{W}	Window thickness
e	Elementary charge
E_{E}	Electric field at emitter
$\boldsymbol{F}_{\mathrm{L}}$	Lorentz force
f_{c}	Electron cyclotron frequency
f_{IF}	Intermediate frequency
f_{LO}	Local Oscillator frequency
f_{vco}	VCO frequency
I_{beam}	Beam current
I_{GTC}	GTC current
I_{HMC}	HMC current
I_{MC}	LMC, UMC and CMC current
$J'_m(x)$	Derivative of the m^{th} Bessel function
K_{I}	Integral gain
K_{P}	Proportional gain
K_{pd}	Phase detector gain
K_{pfd}	Phase frequency detector gain

K_{vco}	Voltage Controlled Oscillator gain
k	Wavenumber
k_z	Transverse wavenumber
$k_{\perp}$	Magnitude of the wave vector in transverse plane
m_{e}	Electron rest mass
q	Electric charge
Q	Quality factor
Q_{diff}	Quality factor of diffraction losses
Q_{ohm}	Quality factor of ohmic losses
R	Reflectivity
r_{c}	Caustic radius of a TE mode
r_{g}	Guiding center radius
r_{L}	Larmor radius
r_{w}	Waveguide radius
r_{cav}	Cavity midsection radius
s	Electron cyclotron harmonic
s_{ctrl}	Control signal
s_{gyro}	Gyrotron mm-wave signal
s_{IF}	Intermediate frequency signal
s_{ref}	Reference signal
s_{vco}	VCO signal
U_{acc}	Accelerating voltage
U_{body}	Body voltage
U_{cath}	Cathode voltage
U_{dep}	Depression voltage
U_{mod}	Modulation anode voltage
$\boldsymbol{v}$	Velocity vector
v	Magnitude of velocity vector
$\boldsymbol{v}_{\parallel}$	Parallel velocity component
$v_{\parallel}$	Magnitude of parallel velocity component
$\boldsymbol{v}_{\perp}$	Transversal velocity component
$v_{\perp}$	Magnitude of transversal velocity component
W_{kin}	Kinetic energy

Greek Letters

α	Pitch factor
$\chi_{m,n}$	n^{th} root of $J'_m(x)$
ϵ	Dielectric permittivity
ϵ_0	Dielectric permittivity in vacuum
η_{neut}	Space charge neutralization
γ	Relativistic Lorentz factor
Ω_{c}	Electron cyclotron angular frequency
ω_{em}	Angular frequency of an electromagnetic wave
ϕ_{E}	Angle between magnetic field at emitter and emitter surface

1 Introduction

As the worldwide energy consumption grows [1], scientists are conducting research to find new energy sources. With climate change [2], one of the major challenges of the current century is to find alternative, emission-free and continuously working energy generation. Nuclear fusion promises to be a nearly in-exhaustive, emission-free energy source. Over the last decades, a major effort has been made to harness the huge potential of nuclear fusion energy.

One possible concept for a fusion power plant is to burn a plasma in toroidal magnetic confinement devices, such as the tokamak or the stellarator [3]. In these devices, the deuterium-tritium fuel for the fusion reaction is heated to extremely high temperatures (in the range of 100 million °C) such that it transitions from a gas into a plasma. In fusion experiments, there is significant focus on researching the generation of a stable fusion plasma for future fusion power plants.

Electron Cyclotron Resonance Heating (ECRH) is a heating method that uses electromagnetic waves in the millimeter-wave (mm-wave) regime to heat the electrons in the plasma. Reaching the required plasma temperatures requires powerful mm-wave sources. Currently, the only device that is capable to deliver continuously high output power in the required mm-wave regime is the gyrotron [4], which is an electron vacuum tube.

Due to varying operating conditions and noise, the output frequency of the gyrotron changes over time. There are applications that greatly benefit from a much more stable frequency. For instance, the probing beam for Collective Thomson Scattering (CTS) diagnostic requires a stable frequency [5], and direct ion heating with beat waves requires precisely setting the frequency of two gyrotrons [6].

The gyrotron can be considered as Voltage Controlled Oscillator (VCO). Phase-Locked Loops (PLLs) [7] compare the phase and frequency of a VCO with a stable reference, and apply a correction voltage to the VCO to counter any unwanted frequency variations. Frequency stabilization with PLLs for low- and medium-power gyrotrons with a triode-type Magnetron Injection Gun (MIG) has already been achieved in [8], [9]. However, the frequency stabilization of megawatt (MW)-class gyrotrons with diode-type MIG has not yet been demonstrated. Compared to low-power gyrotrons, MW-class gyrotrons have higher frequency drifts due to the cavity expansion from heating. Furthermore, a faster control of the accelerating voltage is more complex due to the higher gyrotron capacitance from the larger size. In this thesis, the frequency stabilization with a PLL for MW-class gyrotrons with diode-type MIG is presented.

1.1 Nuclear Fusion

In a nuclear fusion reaction, two light nuclei collide, resulting in a heavier nucleus and excess energy. A number of reactions are possible through this mechanism, depending on the choice of light nuclei. The most promising reaction for future fusion power plants is the fusion of deuterium (D) and tritium (T) into helium (He) and a neutron (n) [10]:

$$^{2}\mathrm{D} + {}^{3}\mathrm{T} \rightarrow {}^{4}\mathrm{He} + \mathrm{n} \tag{1.1}$$

The total energy gained from this reaction is 17.6 MeV, which is carried by the helium (3.5 MeV) and the neutron (14.1 MeV).

A major challenge for a fusion reactor lies in achieving the collisions of the nuclei. To fuse together, the positively charged nuclei need to overcome the repulsive Coulomb force between them until the strong nuclear force binds them together. For this, the nuclei need high kinetic energy, which — for the D-T fusion reaction — requires temperatures in the range of 100 million °C [11]. At such high temperatures, the deuterium-tritium fuel of the reactants becomes a plasma with freely moving electrons and positively charged ions.

Achieving the plasma temperatures in magnetic confinement fusion devices requires a powerful heating system. Possible heating methods include:

- Ohmic heating (only for start-up of tokamaks) [12]
- Neutral Beam Injection (NBI) [13]
- Ion Cyclotron Resonance Heating (ICRH) [14]
- Electron Cyclotron Resonance Heating (ECRH) [15]

Plasma heating with ECRH uses electromagnetic waves to transfer energy to the electrons in the plasma based on the cyclotron interaction. The required frequency of the electromagnetic wave for ECRH is directly linked to the magnetic field strength in the plasma. An advantage of ECRH is the low-loss transmission of the mm-wave radiation by using either waveguides [16] or quasi-optical systems [17], which allow the mm-wave sources to be placed further away from the plasma vessel. Another advantage of the mm-wave regime is the good coupling of the electromagnetic waves into the plasma and the localized power deposition in the plasma through remote steering launchers [18]. Additionally, the high power density of ECRH results in a lower size of the ports into the plasma vessel [15]. Furthermore, heat deposition in the plasma is localized with ECRH, and the location of the power deposition in the plasma can be controlled by steering the launching mirrors of the mm-wave radiation.

Currently, the largest ECRH system in operation is installed at the Wendelstein 7-X (W7-X) stellarator in Greifswald, Germany. It is designed to deliver up to 10 MW heating power at 140 GHz for 30 minutes [15]. The W7-X ECRH system will be upgraded to 15 MW [19]. In Cardache, France, the world´s largest tokamak project ITER is currently under construction. Its ECRH system will provide 20 MW into the plasma at 170 GHz [20].

Heating a fusion plasma with ECRH requires powerful mm-wave sources [15], [21]. Until now, the only device that can deliver high Continuous Wave (CW) output power in the required frequency range at high efficiency (target for ITER: 50 %) is the gyrotron oscillator (gyromontron), which belongs to the family of gyro-devices [22]. While plasma heating through ECRH is the main application, MW-class gyrotrons also have other fusion-related applications such as non-inductive Electron Cyclotron Current Drive (ECCD) [23], plasma stability control [24] and CTS plasma diagnostic [5].

1.2 The Wendelstein 7-X Stellarator

The W7-X stellarator is a fusion experiment, which is located at the Max-Planck-Institute for Plasma Physics (IPP) in Greifswald, Germany. The main purpose of W7-X is to demonstrate the viability of the stellarator concept for a fusion power plant [25]–[27]. W7-X is designed and optimized for steady-state operation [28], [29], and its major objective is to maintain a continuous plasma discharge up to 30 minutes.

The main feature of W7-X is its magnetic coil system, which generates the toroidal and poloidal magnetic field. The uniqueness of the magnetic coil system are fifty non-planar superconducting magnetic coils. The shape of the non-planar magnetic coils is calculated such that the resulting magnetic field geometry complies seven requirements [30]. Additionally, twenty planar coils allow to adjust the rotational transform and change the radial position of the plasma [31]. The nominal magnetic field strength on axis is 2.5 T [27]. The magnetic field has a five-fold symmetry [31], and the plasma vessel consists of five nominally identical modules [29].

Two heating methods are currently in use at W7-X: ECRH and Neutral Beam Injection (NBI). ECRH is the main heating system and is designed to provide a total power of 10 MW for thirty minutes [32], [33]. During the Operational Phase (OP) 1.2 in 2019, the ECRH system delivered a total power of 7.6 MW and the

NBI system 3.6 MW [34]. Additionally, an Ion Cyclotron Resonance Heating (ICRH) system is being commissioned to be installed that will provide 1 MW [35].

The ECRH system at W7-X consists of ten MW-class gyrotrons. It operates at the second electron cyclotron harmonic of the plasma, which corresponds with a nominal magnetic field strength of 2.5 T in the plasma to a frequency of 140 GHz. Nine of the ten W7-X gyrotrons were manufactured by *THALES* in France [36], which are designated as TH1507 gyrotrons. The TH1507 gyrotrons were designed by the Institute for Pulsed Power and Microwave Technology (IHM) at Karlsruhe Insitute of Technology (KIT). An additional gyrotron was manufactured by *CPI* in the USA [37], which is designated as VGT8141A gyrotron. As the ECRH system is designed to accommodate twelve gyrotrons, two more gyrotrons can be added to the ECRH-plant. Furthermore, a 1.5 MW gyrotron is in development [38]. With the upgrade to twelve gyrotrons and with replacing existing gyrotrons by gyrotrons with power levels above 1 MW, the ECRH system will deliver a total power of 15 MW [19].

The structure of the W7-X ECRH system is shown in Figure 1.1. The gyrotrons are located in the two gyrotrons halls 1 and 5, corresponding to the respective module 1 and 5 of the plasma vessel. Each gyrotron hall has the capacity for six gyrotrons. The gyrotron positions are labeled alphabetically from A to F with the number 1 or 5 denoting the gyrotron hall. The W7-X labels and gyrotron serial number is shown in Table 1.1. The two free positions are reserved for future gyrotrons. During OP 1.2 and OP 2.1, the CTS receiver was located at the F5 position.

The mm-wave power from the gyrotrons is transmitted via a full quasi-optical system to the plasma vessel [39], [40]. After the mm-wave beam exits the gyrotron, it is transmitted through a tunnel from the gyrotron hall into the beam duct, where the quasi-optical transmission line to the W7-X plasma vessel is located [33].

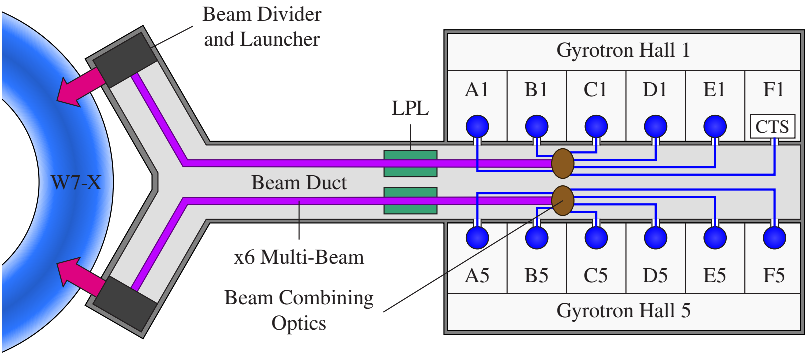

Figure 1.1: ECRH system with gyrotrons, CTS receiver and multi-beam transmission line to the W7-X plasma vessel. The gyrotron mm-wave beam can also be directed into a Long-Pulse Load (LPL) instead of into the plasma vessel.

Table 1.1: W7-X gyrotron labels and corresponding serial numbers

Label	Serial Number	Label	Serial Number
A1	TH1507 SN7i	A5	TH1507 SN5i
B1	TH1507 Maquette	B5	TH1507 SN2i
C1	TH1507 SN1	C5	TH1507 SN4
D1	TH1507 SN6	D5	Reserved
E1	TH1507 SN8	E5	VGT8141A SN3
F1	Reserved	F5	TH1507 SN3

The transmission line has single-beam and multi-beam components. The single-beam section consists of matching optics and polarizers to correct the mm-wave beam of each gyrotron. In addition, each gyrotron has a Short-Pulse Load (SPL) into which their mm-wave beam can be directed. The SPLs can be used for experiments with a maximal pulse length of 100 ms.

A special feature of the transmission system are two multi-beam sections. The individual mm-wave beams are combined through beam combining optics into two multi-beams; each multi-beam section is designed to transmit six individual beams from the respective gyrotron hall (1 and 5). The multi-beams are transmitted via mirrors to the W7-X plasma vessel. At the plasma vessel, the multi-beams are divided into the individual gyrotron mm-wave beams, which are transmitted via launchers into the plasma vessel.

Two Long-Pulse Loads (LPLs) are located in the beam duct for each multi-beam. A gyrotron mm-wave beam can be directed into the LPL, which permits long-pulse gyrotron experiments without transmitting the mm-wave into the W7-X plasma vessel.

1.3 Applications for MW-Class Gyrotrons in Fusion

Today, the main application for MW-class gyrotron is limited to plasma heating and localized plasma stabilization. Precisely controlling the gyrotron frequency would allow more elaborated transmission systems of the mm-wave beam to the plasma with fast directional switches. Moreover, the frequency stabilization of MW-class gyrotrons significantly improves measurements with the CTS diagnostic, or even possible new applications such as direct ion heating with beat waves could emerge from it.

Fast Directional Switch

The FAst DIrectional Switch (FADIS) is a narrow-band diplexer that directs a high-power mm-wave beam to one of two output channels [41], [42]. The switching is controlled electronically by small frequency variation of the mm-wave beam. Thus, the mm-wave beam direction can be switched by changing the set frequency of a frequency stabilized gyrotron. The advantage of such a switch is that no mechanical parts are required, which makes it ideal for mm-wave switches at the plasma vessel. For example, FADIS could be used in ECRH systems to share the installed power between different types of launchers or different applications [43]. Experimental results with FADIS presented in [44] show that frequency-controlled gyrotrons are required for real-world applications.

CTS Diagnostic

The bandwidth of the gyrotron mm-wave beam is important for the CTS diagnostic. A notch filter cuts out the gyrotron signal to protect the sensitive CTS receiver from the high-power gyrotron radiation. Therefore, the bandwidth of the notch filter depends on the gyrotron bandwidth. The narrower the gyrotron bandwidth, the narrower the notch filter bandwidth, and less information of the received CTS spectrum is cut out. This significantly improves the CTS diagnostic accuracy and enables the measurement of plasma parameters such as impurity concentration. Depending on the notch filter bandwidth, the following improvements can be achieved for CTS measurements at W7-X:

- A notch filter bandwidth of below 100 MHz results in a significant increase in precision of the bulk ion and fast ion measurements.
- A notch filter bandwidth of below 50 MHz allows accurate measurements of Ion Bernstein Wave (IBW) of the main plasma species (Hydrogen, Deuterium and Helium).
- Further reducing the notch filter bandwidth to below 10 MHz with a gyrotron linewidth narrower than 0.5 MHz allows IBW measurements of impurities.
- Finally, a notch filter bandwidth of below 1 MHz and gyrotron linewidth below 100 kHz makes plasma turbulence measurements possible [45].

Direct Ion Heating with Beat Waves

By introducing direct ion heating with beat waves, a new fusion-related application could arise from frequency stabilized gyrotrons. With frequency stabilized gyrotrons, the exact output frequency can be precisely set. Overlapping the mm-wave beams of two gyrotrons with each having a different frequency creates power modulations with a beat frequency at the overlap region. The beat frequency is the difference between the two gyrotron frequencies. If the beat frequency is the same as the ion cyclotron frequency in the plasma, direct ion heating using two gyrotrons operating at the ECRH frequency is possible [6], [46], [47]. Because the energy transfer is only in the one-per-mille range, it is unlikely to use this method as main ion cyclotron plasma heating. However, it could be used for the generation of energetic minority ions. Until now, such experiments have not been possible due to the lack of frequency control of MW-class gyrotrons.

1.4 Motivation

Gyrotrons are oscillators used to generate mm-wave radiation at a single frequency. However, due to changing operating conditions, the output frequency of gyrotrons is not a single frequency, as there are frequency variations. Specifically for megawatt-class gyrotrons, the frequency drift in the hundreds of MHz range during the first 1 s of a gyrotron pulse is caused by cavity expansion due to heating and electron beam neutralization [48]. Moreover, for pulse lengths longer than 1 s, the frequency drift is in the MHz range [49].

Ongoing research is conducted on three existing methods to frequency stabilize gyrotrons [50]:

- Reflected wave from non-resonant or resonant loads [51]–[53]
- Injection locking [21], [54]–[60]
- Phase-Locked Loop [7], [55]

Phase-Locked Loops (PLLs) using Phase Frequency Detectors (PFDs) to compare the frequency of a VCO with the stable frequency of a given reference are widely used circuits for frequency control [61] and can also be used on gyrotrons. The gyrotron frequency depends on several operating parameters, such as the accelerating voltage, the magnetic field strength at the cavity or the pitch factor. Thus, the gyrotron can be considered as VCO for the PLL circuit. During operation, the gyrotron frequency can be actively changed with the accelerating voltage for gyrotrons with a diode-type MIG or with the pitch factor for gyrotrons with a triode-type MIG [8].

A major challenge is that the gyrotron PLL circuit actively changes the gyrotron operation. Particularly, controlling the frequency with the accelerating voltage also changes the output power. Additionally, the control parameter with which the gyrotron frequency is changed must be controlled fast enough to sufficiently suppress the frequency drifts. The advantage of a PLL circuit is that it can be used on existing gyrotrons and does not need a specific gyrotron design. For instance, injection locking requires a suitable launcher in the gyrotron [62], [63].

The promising potential to stabilize the frequency of a low- to medium-power gyrotron via the modulation anode voltage of a triode-type MIG using a PLL was demonstrated in [8] and [9]. The output frequency was stabilized to a bandwidth below 1 Hz with 100 W and below 2 Hz with 25 kW, respectively. Compared to low-power and medium-power gyrotrons, MW-class gyrotrons have higher frequency drifts due to the larger cavity expansion from ohmic wall losses and higher noise in the high-power high-voltage supplies. Furthermore, a faster control of the accelerating voltage is more complex due to the higher gyrotron capacitance from the larger size [55]. Until now, no PLL-based frequency stabilization circuit has been implemented for MW-class gyrotrons with a diode-type MIG. In this thesis, the advantage of such a frequency stabilization system is exemplary demonstrated on the gyrotrons at the W7-X stellarator.

The scope of this thesis is to design and implement a PLL-based frequency control circuit for MW-class gyrotrons. The experimental validation of the PLL circuit is performed with the gyrotrons at the W7-X stellarator. For the first time, it is shown that the frequency of MW-class gyrotrons can be stabilized with a PLL circuit. Furthermore, this thesis focuses on the applications of frequency-stabilized MW-class gyrotrons. Specifically, at W7-X, the newly developed CTS diagnostic at 174 GHz demands a stable gyrotron frequency to ensure precise measurements of fast ion velocity distribution function. The possibility of conducting experiments for direct ion heating with beat waves is also being considered, and specific experiments are conducted to demonstrate the feasibility of the PLL frequency control circuit for these applications.

1.5 Structure of This Thesis

This thesis is organized as follows. In Chapter 2, the gyrotron theory of operation is presented, and the fundamentals for a frequency stabilization with a PLL are given.

In Chapter 3, the implementation of the PLL circuit for MW-class gyrotrons is presented. The operating parameters that affect the gyrotron frequency are identified, and simulation results demonstrating how the frequency dependence of the W7-X TH1507 gyrotron on different parameters are presented. The PLL is theoretically investigated, and a model is established to analyze the PLL circuit for MW-class gyrotrons.

In Chapter 4, the operation of a W7-X ECRH gyrotron for the CTS diagnostic is investigated. Increasing the Signal-to-Noise Ratio (SNR) of the CTS receiver requires a probing beam with a frequency between 170 GHz to 180 GHz. A new 7 T magnetic system has been procured to allow the operation of a TH1507 gyrotron at the required CTS frequency. Experiments are conducted to demonstrate the successful operation for the CTS diagnostic.

In Chapter 5, experiments are conducted with the W7-X gyrotrons using the implemented PLL circuit. The experimental setup is explained, and frequency stabilization experiments with the gyrotrons from manufacturer *THALES* and *CPI* are conducted. Specific experiments are performed to use thePLL circuit for its intended applications at W7-X (CTS diagnostic and experiments with direct ion heating through beat waves from two gyrotrons).

To extend the PLL circuit, the change to a triode-type MIG is considered in Chapter 6. Theoretical investigations are conducted to determine the frequency dependence on voltage of the modulation anode with a triode-type MIG for future W7-X gyrotrons. Finally, a conclusion and outlook is given in Chapter 7.

2 Fundamentals

This chapter presents the fundamentals for a frequency stabilization of MW-class gyrotrons with a PLL system. A general overview on gyrotron theory of operation is presented, and the electron beam – electromagnetic wave interaction is explained. The gyrotron key components are described. Furthermore, the fundamentals to stabilize the frequency of a VCO with a PLL is given.

2.1 Gyrotron Theory of Operation

The main part of the gyrotron is the interaction region, where an annular electron beam interacts with an electromagnetic wave, and the electrons transfer their kinetic energy to the electromagnetic wave. The interaction takes place in a weakly inhomogeneous waveguide, which forms a resonator. In this thesis, gyrotrons with a hollow cylindrical waveguide structure are considered, and the interaction region is referred to as the cavity. The electrons interact with Transverse Electric (TE) modes in the cavity.

In Figure 2.1, the structure of a gyrotron with a diode-type MIG is shown. The magnetic system consists of three superconducting magnets (main coil, compensating coil and gun coil) and generates the static magnetic field. The magnetic field strength along the z axis, which is in line with the gyrotron axial direction, is also shown in Figure 2.1. The magnetic field strength has its maximum value at the center of the cavity. The MIG generates an annular electron beam by thermal emission. The electric potential difference between cathode and anode accelerates the electrons. The emitted electrons are guided by the external static magnetic

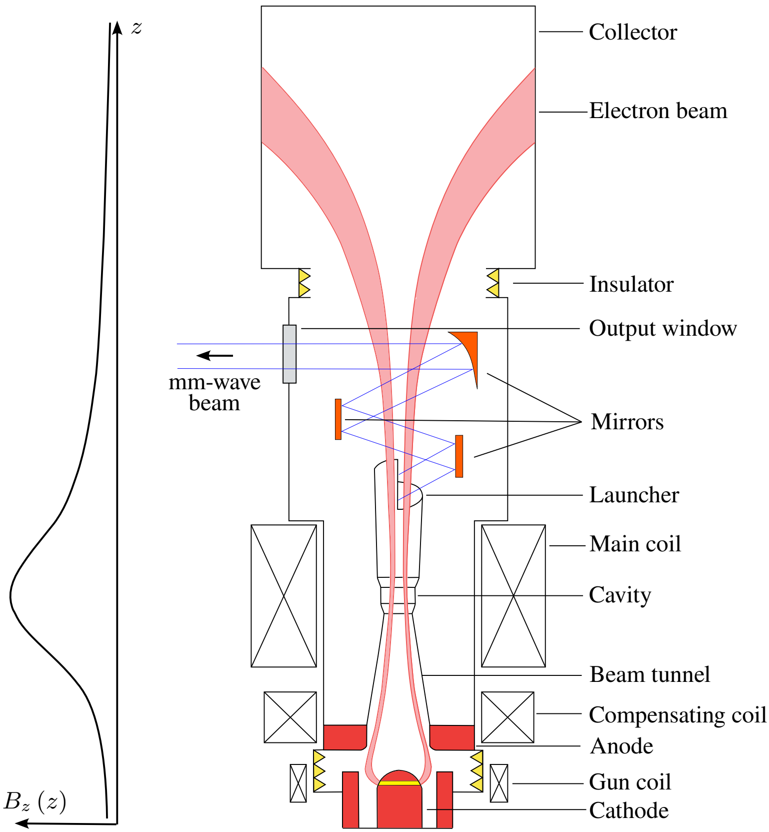

Figure 2.1: Gyrotron Structure

field through the beam tunnel into the cavity. There, the electrons interact with a Transverse Electric (TE) mode. The electrons transfer part of their transverse kinetic energy to the TE mode. Finally, the electron beam passes through the launcher to the collector.

The excited TE mode needs to exit the gyrotron in a suitable way for the subsequent external transmission line. In high-power gyrotrons, the mm-wave exits the gyrotron via a quasi-optical system. At the launcher, the TE mode is converted into the Gaussian fundamental Transverse Electric Magnetic (TEM) mode. After being reflected by mirrors, the resulting Gaussian $\mathrm{TEM}_{0,0}$ mode exits the gyrotron radially through a diamond window.

2.1.1 Electron Beam Kinetics

The MIG generates an annular electron beam in which electrons gyrate around the static magnetic field lines. The annular electron beam is described mathematically, and the important electron beam parameters for the interaction in the cavity are elaborated. Furthermore, other effects such as the electrostatic voltage depression and the electron space charge neutralization are explained.

Electron Motion in a Static Magnetic Field

The trajectory of a charged particle in electric and magnetic fields is governed by the Lorentz force $\boldsymbol{F}_\mathrm{L}$:

$$\boldsymbol{F}_\mathrm{L} = q\left(\boldsymbol{E} + \boldsymbol{v} \times \boldsymbol{B}\right) \tag{2.1}$$

where $\boldsymbol{E}$ and $\boldsymbol{B}$ are, respectively, the electric and magnetic vector fields, and q and $\boldsymbol{v}$ are, respectively, the charge and velocity vector of the particle.

The trajectory of an electron moving in a static magnetic field (without an electric field) is a helical path [64]. The electron follows the magnetic field lines with a circular motion in the transverse plane to the magnetic field line. The velocity vector of the electron is divided into two components: $\boldsymbol{v}_{||}$ and $\boldsymbol{v}_{\perp}$:

$$\boldsymbol{v} = \boldsymbol{v}_{||} + \boldsymbol{v}_{\perp} \tag{2.2}$$

The subscripts $||$ and $\perp$ denote components parallel and transverse to the static magnetic field. In the gyrotron cavity, the direction of the static magnetic field is in the z-direction, in line with the axial direction.

The electrons gyrate with the electron cyclotron frequency f_c [65]:

$$f_\mathrm{c} = \frac{\Omega_\mathrm{c}}{2\pi} = \frac{eB}{2\pi\gamma m_\mathrm{e}} \approx 28 \frac{B}{\gamma} \frac{\mathrm{GHz}}{\mathrm{T}} \tag{2.3}$$

where $e = 1.602 \times 10^{-19}$ C is the elementary charge, $m_\mathrm{e} = 9.109 \times 10^{-31}$ kg is the rest mass of an electron and B is the magnitude of the static magnetic field. The relativistic Lorentz factor γ is calculated with [66]:

$$\gamma = \frac{1}{\sqrt{1 - \frac{v^2}{c^2}}} = 1 + \frac{W_\mathrm{kin}}{m_\mathrm{e}c^2} \approx 1 + \frac{W_\mathrm{kin}}{511\,\mathrm{keV}} \tag{2.4}$$

where $c = 299\,792\,458$ m/s is the speed of light in vacuum, v is the magnitude of the electron velocity and W_kin is the kinetic energy of the electron.

The radius of the circular motion is the Larmor radius r_L and is calculated with [67]:

$$r_\mathrm{L} = \frac{\gamma m_\mathrm{e} v_\perp}{eB} \tag{2.5}$$

An important electron beam parameter is the pitch factor α, which is the ratio of the transverse to the parallel velocity magnitudes [65]:

$$\alpha = \frac{v_\perp}{v_\parallel} \tag{2.6}$$

For the interaction with the electromagnetic wave, the kinetic energy of the transverse component is relevant, and a high α leads to possible higher interaction efficiency [68]. In gyrotrons, typical values for α are between 1.1 to 1.3 [18].

A cross-section of the annular electron beam is shown in Figure 2.2. The center of an electron cyclotron orbit is called the guiding center. The MIG generates an annular hollow electron beam in which multiple electron cyclotron orbits are distributed on a circle. The radius on which the guiding centers of the different cyclotron orbits are located is the guiding center radius r_g. The electrons each have an initial phase with which they rotate. In Figure 2.2, the initial phases of the electrons are randomly distributed.

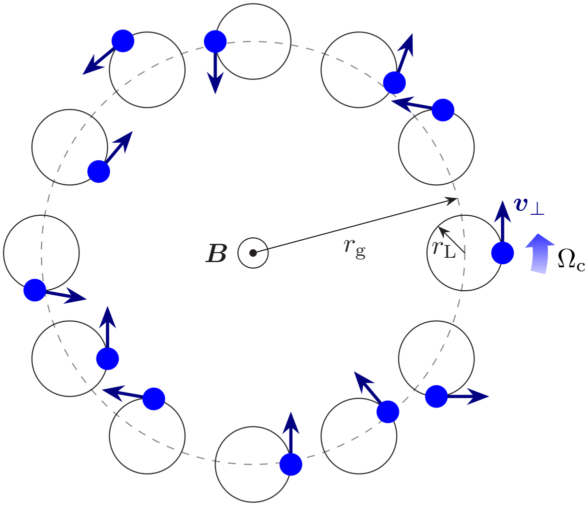

Figure 2.2: Cross-section of the annular electron beam. The centers of the electron cyclotron orbits with Larmor radius r_L are distributed on the guiding center radius r_g

In a real MIG, the electrons are not emitted at the same position and do not have exactly the same velocity. To take statistical variations into account, the electron beam parameters are described with their mean and spread values [64]. In the following notation, the mean value of a beam parameters x is denoted with $\overline{x}$ and its spread value with Δx. The spread values for the pitch factor, Lorentz factor and kinetic energy are calculated with [18]:

$$\Delta\alpha = \frac{1}{\overline{\alpha}}\sqrt{\frac{1}{N}\sum_{n=1}^{N}\left(\alpha_n - \overline{\alpha}\right)^2} \tag{2.7}$$

$$\Delta\gamma = \frac{1}{\overline{\gamma}}\sqrt{\frac{1}{N}\sum_{n=1}^{N}\left(\gamma_{,n} - \overline{\gamma}\right)^2} \tag{2.8}$$

$$\Delta W_\mathrm{kin} = \frac{1}{\overline{W}_\mathrm{kin}}\sqrt{\frac{1}{N}\sum_{n=1}^{N}\left(W_{\mathrm{kin},n} - \overline{W}_\mathrm{kin}\right)^2} \tag{2.9}$$

where N is the total number of electrons. The spread for the guiding center radius is uniformly distributed and is defined as

$$\Delta r_{\mathrm{g}} = \frac{r_{\mathrm{g,max}} - r_{\mathrm{g,min}}}{2\overline{r}_{\mathrm{g}}} \tag{2.10}$$

where $r_{\mathrm{g,max}}$ and $r_{\mathrm{g,min}}$ are respectively the maximum and minimum r_{g} from all electrons.

Adiabatic Approximation

The electron motion from the MIG to the cavity is considered under the adiabatic approximation, which is only valid for small variations of the magnetic field [69]. Along the electron trajectory through the beam tunnel, the field strength from the static magnetic field increases until it reaches its peak value at the center of the cavity. According to the adiabatic approximation, the adiabatic moment is invariant [70], [71]:

$$\frac{(\gamma m_{\mathrm{e}} v_{\perp})^2}{B} = \text{constant} \tag{2.11}$$

With constant Lorentz factor γ, if the magnetic field strength increases, $v_{\perp}$ also increases to keep the adiabatic moment constant. Because the electron kinetic energy does not change (the entire beam tunnel is at the same electric potential), $v_{\|}$ decreases (Equation 2.2), and the pitch factor increases.

Additionally, the increasing static magnetic field results in a compression of the field lines. Since the electrons follow the magnetic field lines, the guiding center radius of the electrons decreases to the cavity center. According to the Bush theorem [72], [73], the magnetic compression ratio b is

$$b = \frac{B_{\mathrm{cav}}}{B_{\mathrm{E}}} = \left(\frac{r_{\mathrm{g,E}}}{r_{\mathrm{g,cav}}}\right)^2 \tag{2.12}$$

where B_{E} is the magnetic field strength at the emitter and $r_{\mathrm{g,E}}$ and $r_{\mathrm{g,cav}}$ the guiding center radii at the emitter and the center of the cavity, respectively.

Voltage Depression

The electrons are accelerated in the electron gun with the accelerating voltage U_{acc}. The electron space charge counteracts the accelerating voltage, and therefore, the electrons do not experience the full accelerating voltage, but a decreased (or depressed) voltage. The resulting voltage from the electron space charge is called depression voltage U_{dep} and is estimated for ideal vacuum conditions with [74]

$$U_{\mathrm{dep}} = \frac{I_{\mathrm{beam}}}{2\pi\epsilon_0 v_{\|}} \ln\left(\frac{r_{\mathrm{w}}}{r_{\mathrm{g}}}\right) \tag{2.13}$$

The resulting kinetic energy for the electrons is

$$W_{\mathrm{kin}} = -e\left(U_{\mathrm{acc}} + U_{\mathrm{dep}}\right) \tag{2.14}$$

and

$$\gamma = 1 + \frac{-e\left(U_{\mathrm{acc}} + U_{\mathrm{dep}}\right)}{m_{\mathrm{e}}c^2} \tag{2.15}$$

Space Charge Neutralization

The estimation for the depression voltage in Equation 2.13 is only valid for an ideal vacuum inside the gyrotron. Although the gyrotron has an ultra-high vacuum of $< 1 \times 10^{-6}$ mbar [75], some residual gas is still present. During the gyrotron operation, the electron beam ionizes the residual gas. The positively charged ions are attracted to the electron beam. As a result, the electron beam space charge is partially neutralized, which reduces the depression voltage [76], [77].

The neutralization η_{neut} indicates how much the space charge is neutralized. A value of 0 % means that the electron beam is not neutralized and a value of 100 % means that the electron beam is fully neutralized. The neutralization affects the depression voltage and the neutralized depression voltage $\tilde{U}_{\mathrm{dep}}$ is calculated with

$$\tilde{U}_{\mathrm{dep}} = (1 - \eta_{\mathrm{neut}}) U_{\mathrm{dep}} \tag{2.16}$$

where U_{dep} is the non-neutralized depression voltage and is calculated with Equation 2.13.

The neutralization process takes some time. At the start of a pulse, the electron beam is not neutralized. After full ionization of the gas, the final value for the neutralization is reached. Basic neutralization time estimations yield a time in the order of 400 ms [78]. Therefore, for Short-Pulse (SP) operation (< 100 ms), neutralization does not need to be considered. However, for Long-Pulse (LP) ($>$ 1 s) or CW operation, the neutralization needs to be considered [79].

2.1.2 Interaction Mechanism

A detailed description of the gyrotron interaction mechanism is presented in [64], [65], [67], [69]. When the frequency of the electromagnetic wave ω_{em} is equal to the electron cyclotron frequency Ω_{c} in its reference frame, the electron experiences a constant electric field. Some electrons are accelerated and gain energy from the electromagnetic wave, while other electrons are decelerated and transfer energy to the electromagnetic wave. The acceleration or deceleration of an electron depends on the phase position of the electron cyclotron motion relative to the rotating electric field, which is shown in Figure 2.3.

If the frequency of the electromagnetic wave is slightly higher than the electron cyclotron frequency, the electrons lag behind the electric field. Electrons in the decelerating phase decrease their kinetic energy and become lighter. With Equation 2.3, their electron cyclotron frequency increases. The difference between Ω_{c} and ω_{em} decreases, and Ω_{c} approaches ω_{em}. Thus, the decelerated electrons

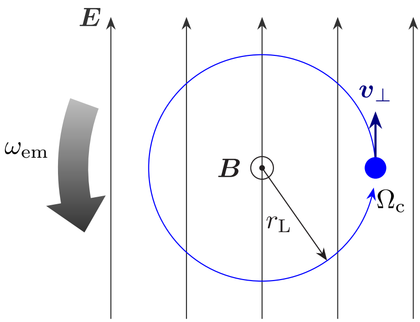

(a) Electron is in the decelerating phase and loses kinetic energy

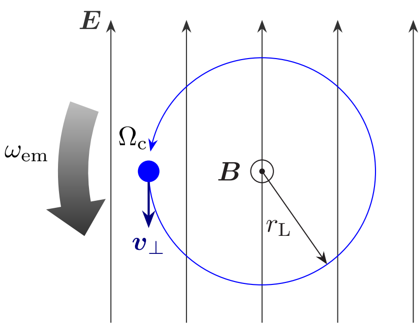

(b) Electron is in the accelerating phase and gains kinetic energy

Figure 2.3: Electrons in the decelerating or accelerating phase depending on the angle between the transverse velocity vector $\boldsymbol{v}_\perp$ of the electron and the electric field vector E of an electromagnetic wave

remain longer in the favorable deceleration phase. Conversely, the electrons in the accelerating phase increase their kinetic energy and become heavier. Their electron cyclotron frequency decreases, which also increases the difference between ω_{em} and Ω_{c}. This results in accelerated electrons leaving the less favorable accelerating phase faster until they reach the decelerating phase. Overall, the electrons are accumulated in the decelerating phase. This mechanism is called phase bunching [67].

The initial phase of the electron cyclotron motion is randomly distributed among the electrons that enter the interaction region. On average, as many electrons are in the decelerating phase as in the accelerating phase, and no net energy is transferred from the electron beam to the electromagnetic wave. Due to phase bunching, a net energy transfer from the electron beam to the electromagnetic wave is achieved.

The condition for which the electromagnetic wave is synchronized with the electron motion is called the resonance condition [80]:

$$\omega_{\mathrm{em}} \simeq s\Omega_{\mathrm{c}} + k_z v_{\|} \tag{2.17}$$

where ω_{em} is the angular frequency of the electromagnetic wave, k_z is the component of the wavevector of the electromagnetic wave parallel to the external static magnetic field, $v_{\|}$ is the electron velocity component parallel to the external static magnetic field. The term $k_z v_{\|}$ accounts for the frequency Doppler shift due to the moving electrons. The positive natural number s denotes the harmonic of the electron cyclotron frequency.

2.1.3 Key Components

After the description of the electron beam and the explanation of the gyrotron interaction, the different key components of a MW-class gyrotron are presented.

Magnetron Injection Gun

The Magnetron Injection Gun (MIG) generates the annular electron beam. Two types of conventional MIGs exist: diode-type MIG and triode-type MIG. In Figure 2.4, the structure of both MIG types is shown [81].

The main components of the diode-type MIG are the cathode and the anode. The electric potential of the anode is higher than the one of the cathode, and electrons in the cathode are attracted to the anode. The electrons leave the heated emitter

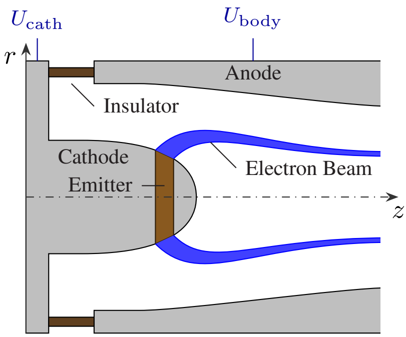

(a) Diode-type MIG

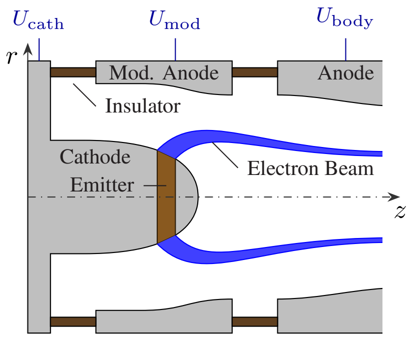

(b) Triode-type MIG

Figure 2.4: Structure of diode-type and triode-type Magnetron Injection Guns (MIGs) [81]. The applied voltages are the cathode voltage U_{cath}, body voltage U_{body} and modulation anode voltage U_{mod}.

ring on the cathode by thermionic emission [82]. The beam current I_{beam} depends on the temperature of the emitter, and the saturated emission current density is given by the Richardson–Dushman equation [83] including the Schottky effect [22].

The potential difference between the cathode and anode is the accelerating voltage U_{acc}. In Figure 2.4, the cathode is on the potential U_{cath}, and the anode is on the potential U_{body}. The accelerating voltage is calculated with [49]:

$$U_{\mathrm{acc}} = U_{\mathrm{cath}} - U_{\mathrm{body}} \tag{2.18}$$

The accelerating voltage is negative. In the following, absolute values for the accelerating voltage are used and the negative sign is implied.

The transverse velocity of the electrons at the emitter $v_{\perp \mathrm{E}}$ is calculated with [65]:

$$v_{\perp \mathrm{E}} = \frac{E_{\mathrm{E}} \cos\left(\phi_{\mathrm{E}}\right)}{\gamma_{\mathrm{E}} B_{\mathrm{E}}} \tag{2.19}$$

where ϕ_E is the angle between the magnetic field at the emitter and the emitter surface, γ_E is the Lorentz factor at the emitter and E_E the electric field strength at the emitter. With Equation 2.11 and Equation 2.12, the transverse velocity at the cavity $v_{\perp\,\mathrm{cav}}$ is:

$$v_{\perp\,\mathrm{cav}} = \frac{b^{\frac{3}{2}} E_\mathrm{E} \cos\left(\phi_\mathrm{E}\right)}{\gamma_\mathrm{cav} B_\mathrm{cav}} \tag{2.20}$$

where γ_cav is the Lorentz factor at the cavity.

Triode-type MIGs have an additional modulation anode that can have a different potential U_mod than the anode potential [84], [85]. With the modulation anode, it is possible to change the electric field at the emitter surface without changing the kinetic energy of the electrons at the center of the cavity [81]. This additional degree of freedom allows to change independently the pitch factor and guiding center radius of the electron beam at the cavity.

Cavity

In hollow cylindrical waveguides, TE and Transverse Magnetic (TM) modes are the eigenmode solutions of the Maxwell's equation for the electric and magnetic fields due to the constraints of the boundary conditions [86]. The gyrotron interaction requires a phase velocity of the electromagnetic wave that is much higher than the electron axial velocity [64]. Therefore, modes are excited near their cut-off frequency. The interaction is efficient with TE modes, because they only have transverse electric field components. The angular frequency is related to the wavenumber k through

$$\omega = ck = c\sqrt{{k_\perp}^2 + {k_z}^2} \tag{2.21}$$

where $k_\perp$ is the transverse wavenumber and k_z the axial wavenumber. In a hollow cylindrical waveguide, the transverse wavenumber $k_\perp$ of a $\mathrm{TE}_{m,n}$ mode is:

$$k_\perp = \frac{\chi_{m,n}}{r_\mathrm{w}} \tag{2.22}$$

where $\chi_{m,n}$ is the n^{th} root of $J'_m(x)$, $J'_m(x)$ is the derivative of the m^{th} Bessel function and r_w is the radius of the waveguide.

The cut-off frequency is the frequency under which a $\text{TE}_{m,n}$ mode cannot propagate through the waveguide and is calculated with Equation 2.21 and Equation 2.22 for $k_z = 0$:

$$f_\text{cut} = \frac{c}{2\pi}\frac{\chi_{m,n}}{r_\text{w}} \tag{2.23}$$

The caustic radius of a $\text{TE}_{m,n}$ modes is defined as [65]

$$r_\text{c} = \frac{m}{\chi_{m,n}} r_\text{w} \tag{2.24}$$

The typical structure of the gyrotron cavity is illustrated in Figure 2.5. The cavity consists of a downtaper, a midsection and an uptaper. The midsection of the cavity has a constant radius r_cav.

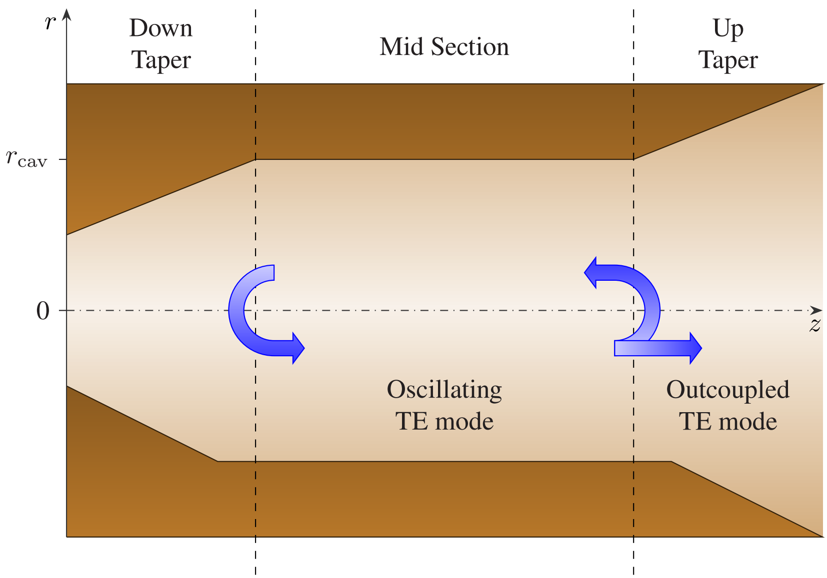

Figure 2.5: Gyrotron cavity structure

The downtaper at the entrance of the cavity reflects the excited TE mode back into the midsection. As the cavity radius decreases, the cut-off frequency of the TE mode increases. The point at which the cut-off frequency is greater than the excited frequency is where the TE mode is reflected.

The uptaper at the end of the cavity couples out a part of the oscillating TE mode. Since the uptaper results in a changing characteristic impedance, part of the TE mode is reflected back into the cavity and part of it is transmitted to the launcher. Therefore, the cavity is a resonator with diffraction losses, which are accounted for with the diffraction quality factor Q_{diff}.

In a real cavity, the wall is not perfectly conducting and ohmic losses occur inside the wall. The total quality factor of the cavity without the electron beam is [18]:

$$\frac{1}{Q} = \frac{1}{Q_{\mathrm{diff}}} + \frac{1}{Q_{\mathrm{ohm}}} \tag{2.25}$$

where Q_{diff} and Q_{ohm} are the quality factor for diffraction and the ohmic losses, respectively. The calculations for Q_{diff} and Q_{ohm} is described in [69].

The coupling of the electron beam with a specific $\mathrm{TE}_{m,n}$ mode depends on the guiding center radius of the electron beam. The coupling factor for co-rotating modes is defined as [87]

$$G_{m,n} = \frac{J_{m-1}\left(k_{\perp,m,n} r_{\mathrm{g}}\right)}{J_m\left(\chi_{m,n}\right)\sqrt{\pi\left(\chi_{m,n}^2 - m^2\right)}} \tag{2.26}$$

The optimal guiding center radius for the electron beam is where the coupling factor reaches its maximum value and is calculated with:

$$r_{\mathrm{g,opt}} = r_{\mathrm{cav}} \frac{\chi_{m-1,1}}{\chi_{m,n}} \tag{2.27}$$

Quasi-Optical Output System

The quasi-optical output system system decouples the electromagnetic wave from the electron beam, and is described in detail in [88]. The quasi-optical system comprises the launcher and several mirrors. The launcher converts the operating $\mathrm{TE}_{m,n}$ mode, which propagates in a cylindrical waveguide, into a linear polarized Gaussian $\mathrm{TEM}_{0,0}$ mode. A summary and comparison between different launcher designs is given in [89]. The resulting Gaussian mode is transmitted quasi-optically via a mirror system to the gyrotron window. The electromagnetic wave exits the gyrotron radially.

Output Window

After the conversion into a Gaussian like beam, the electromagnetic wave exits the gyrotron through a window. In high-power gyrotrons, the window requires low loss tangents and high thermal conductivity to allow the cooling system to remove the heat from the losses. Diamond windows have the most suitable characteristics for high-power gyrotrons. They are produced with the Chemical Vapor Deposition (CVD) process [90].

In conventional high-power gyrotrons, the out-coupling of the electromagnetic wave is based on the resonant window principle. Since the window has a different dielectric permittivity ϵ than the inside and outside of the gyrotron, the electromagnetic wave is reflected at when the electromagnetic wave enters the window and when it exits the window. If the window thickness has the same length as half of the wavelength of the electromagnetic wave, the reflected waves interfere destructively at the entrance of the window. Thus, the window is resonant and transparent for the electromagnetic wave. This also applies if the window lengths is multiples of half of the wavelength.

The frequencies at which the window is resonant are [90]:

$$f_{\mathrm{res}} = n \frac{c}{2\sqrt{\epsilon_r'} d_{\mathrm{W}}} \tag{2.28}$$

where n is a positive natural number, ϵ_r' the real part of the complex dielectric permittivity $\epsilon_r = \epsilon_r' \left(1 - j \tan\left(\delta\right)\right)$ of the window material, $\tan\left(\delta\right)$ the loss angle of the window material, and d_W the window thickness. For diamond windows, $\epsilon_r' \approx 5.67$ and $\tan\left(\delta\right) \approx 2 \times 10^{-5}$ to 3×10^{-5} [90].

If the electromagnetic wave has a different frequency, part of it is reflected at the window. The amount which is reflected back is called reflection R and is defined as [91], [92]:

$$R = \frac{R_0\left(1 - 2T_0 \cos\left(2\beta_\epsilon d_\mathrm{W}\right)\right) T_0^2}{1 - 2R_0 T_0 \cos\left(2\beta_\epsilon d_\mathrm{W} - 2\phi\right) + R_0^2 T_0^2} \tag{2.29}$$

where $R_0 = |\rho|^2$, $\phi = \arg\left(\rho\right)$ and $T_0 = e^{-2\alpha_\epsilon d_\mathrm{W}}$, α_ϵ and β_ϵ are the respective attenuation and phase constant of an electromagnetic wave, while ρ is the complex reflection factor. They are calculated for a TEM wave by [92]:

$$\alpha_\epsilon = \frac{1}{2} k_0 \sqrt{\epsilon_r'} \tan\left(\delta\right) \tag{2.30}$$

$$\beta_\epsilon = k_0 \sqrt{\epsilon_r'} \sqrt{\frac{1}{2} + \frac{1}{2}\sqrt{\tan\left(\delta\right)^2 + 1}} \tag{2.31}$$

$$\rho = \frac{1 - \sqrt{\epsilon_r}}{1 + \sqrt{\epsilon_r}} \tag{2.32}$$

Collector

After the separation from the electromagnetic wave, the electrons continue their trajectory to the collector and hit the collector wall. Since the electrons have some remaining kinetic energy after the interaction in the cavity, the collector wall heats up. Therefore, cooling of the collector wall is required. To further prevent thermal damage to the collector, a magnetic system sweeps the electron beam in axial and transverse direction such that the electrons hit the entire collector wall homogeneously [93]–[95].

After the interaction, some of the remaining electron kinetic energy can be recovered by operating the gyrotron with a depressed collector. The principle is to decelerate the electrons with a voltage at the collector. With a single-stage depressed collector, the collector is at a different electric potential than the anode and body of the gyrotron. Thus, the electrons do not experience the full accelerating voltage U_{acc} at the collector and are slowed down. With single-stage depressed collector, the total efficiency of high-power gyrotrons can be increased to up to 50 % [96]. Ongoing research is conducted on multi-stage depressed collectors to further increase the total gyrotron efficiency [97], [98].

2.2 Phase-Locked Loops for Frequency Stabilization

Phase-Locked Loop (PLL) systems [99] are widely used to control and stabilize the output frequency of VCOs. The general principle of a PLL is shown in Figure 2.6 [7]. A PLL consist of four components:

- **Voltage Controlled Oscillator (VCO)**: The frequency f_{vco} of the VCO signal s_{vco} linearly depends on its input voltage.
- **N-divider**: The N-divider divides the phase and frequency of the VCO: $f_{\mathrm{vco,N}} = \frac{f_{\mathrm{vco}}}{N}$
- **Phase Detector (PD)**: The PD compares the phase of the reference signal s_{ref} with $s_{\mathrm{vco,N}}$. The output is an error signal s_{err} that is proportional to the phase difference of the two input signals.
- **Loop Filter**: The loop filter determines the stability of the control loop. It filters the error signal from the PD and its output s_{ctrl} controls the VCO frequency. In conventional PLLs, the loop filter is a Proportional-Integral filter (PI filter).

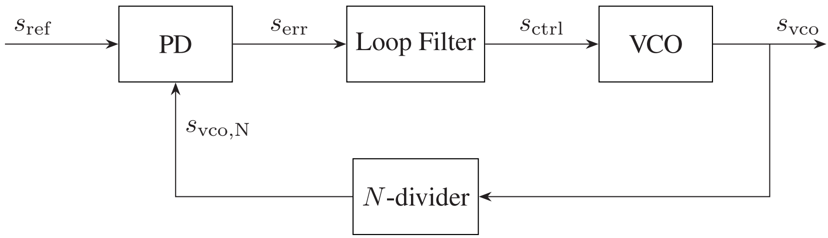

Figure 2.6: General principle of a PLL

If the VCO has a different phase than the reference signal, the PD outputs an error signal. After filtering of the error signal s_{err}, the loop filter applies the control voltage s_{ctrl} to the VCO such that the phase of the VCO equals the phase of the reference signal.

For the VCO, the instantaneous frequency f is defined as the derivative of its instantaneous phase ϕ [100]:

$$f = \frac{1}{2\pi}\frac{d}{dt}\phi(t) \tag{2.33}$$

The PLL is also used for frequency stabilization. With the PLL from Figure 2.6, the frequency of a VCO will always be controlled such that its frequency equals to:

$$f_{\mathrm{set}} = N f_{\mathrm{ref}} \tag{2.34}$$

where f_{set} is the desired set frequency of the VCO. The set frequency can be changed with the N-divider or the reference frequency.

Two categories of PLLs exist based on the N-divider type:

- Integer-N PLLs [101]
- Fractional-N PLLs [102]

2.2.1 Linear Control Theory of PLLs

The fundamentals on linear PLL theory are described in [7], [61]. In the following, the PLL is analyzed with linear control theory to investigate the stability of the control system and to determine the optimal control parameters. While the linear theory is only valid if the frequency of the VCO and reference signal are the same, the results give useful insights on the dynamics and stability of the real implemented PLL.

To determine the stability of the PLL control system, the open loop transfer function is investigated in the Laplace domain. For the linear PLL, the transfer functions of the PD, loop filter and VCO are determined. The transfer function of the N-divider has a constant gain

$$H_N(s) = \frac{1}{N} \tag{2.35}$$

The output of the PD is a signal that is proportional to the phase difference between the reference and the VCO. Thus, the transfer function of the PD is the constant gain K_{pd}:

$$H_{\mathrm{pd}}(s) = K_{\mathrm{pd}} \tag{2.36}$$

For the PI filter, the transfer function is

$$H_{\mathrm{PI}}(s) = K_{\mathrm{P}} + K_{\mathrm{I}}\frac{1}{s} = \frac{K_{\mathrm{P}}s + K_{\mathrm{I}}}{s} \tag{2.37}$$

where K_{P} is the proportional gain and K_{I} the integral gain of the PI filter. As the VCO integrates the phase, the VCO transfer function is

$$H_{\mathrm{vco}}(s) = K_{\mathrm{vco}}\frac{1}{s} \tag{2.38}$$

where K_{vco} is the VCO gain. The output frequency of the VCO is

$$f_{\mathrm{vco}} = \frac{1}{2\pi}K_{\mathrm{vco}}u_{\mathrm{in}} \tag{2.39}$$

where u_{in} is the input voltage of the VCO.

The open loop transfer function of the ideal PLL is the multiplication of the transfer functions of its three components:

$$\begin{aligned} H_{\mathrm{ol}}(s) &= H_{\mathrm{pd}}(s)\, H_{\mathrm{PI}}(s)\, H_{\mathrm{vco}}(s)\, H_N(s) \\ &= \frac{K_{\mathrm{pd}} K_{\mathrm{vco}} \left(K_{\mathrm{P}} s + K_{\mathrm{I}}\right)}{N s^2} \\ &= K \frac{s + \omega_{\mathrm{I}}}{s^2} \end{aligned} \tag{2.40}$$

where K is the total proportional gain

$$K = \frac{K_{\mathrm{pfd}} K_{\mathrm{vco}} K_{\mathrm{P}}}{N} \tag{2.41}$$

and

$$\omega_{\mathrm{I}} = \frac{K_{\mathrm{I}}}{K_{\mathrm{P}}} \tag{2.42}$$

The stability of the closed loop is analyzed in the bode diagram of the open loop transfer function [7]. An example of the bode diagram for H_{ol} is shown in Figure 2.7 with $f_K = \frac{K}{2\pi} = 16\,\mathrm{kHz}$ and $f_{\mathrm{I}} = \frac{w_{\mathrm{I}}}{2\pi} = 1\,\mathrm{kHz}$. At frequencies below f_{I}, the amplitude of H_{ol} decreases with a slope of $-40\,\mathrm{dB}$ per decade, and for frequencies higher than f_{I}, the slope of the amplitude is $-20\,\mathrm{dB}$ per decade. At f_K, the amplitude has $0\,\mathrm{dB}$. The phase of H_{ol} starts for low frequencies at $-180°$ and rises to $-90°$.

Stability of the closed loop is determined when the amplitude of H_{ol} crosses $0\,\mathrm{dB}$ [61]. A phase of H_{ol} below $-180°$ results in a positive feedback. For amplitudes higher than $0\,\mathrm{dB}$, positive feedback guarantees instability of the closed loop. The phase margin is defined as the difference between the phase at the $0\,\mathrm{dB}$ crossing point and $-180°$, and a negative phase margin results in an unstable closed loop. In Figure 2.7, the phase margin is 87°.

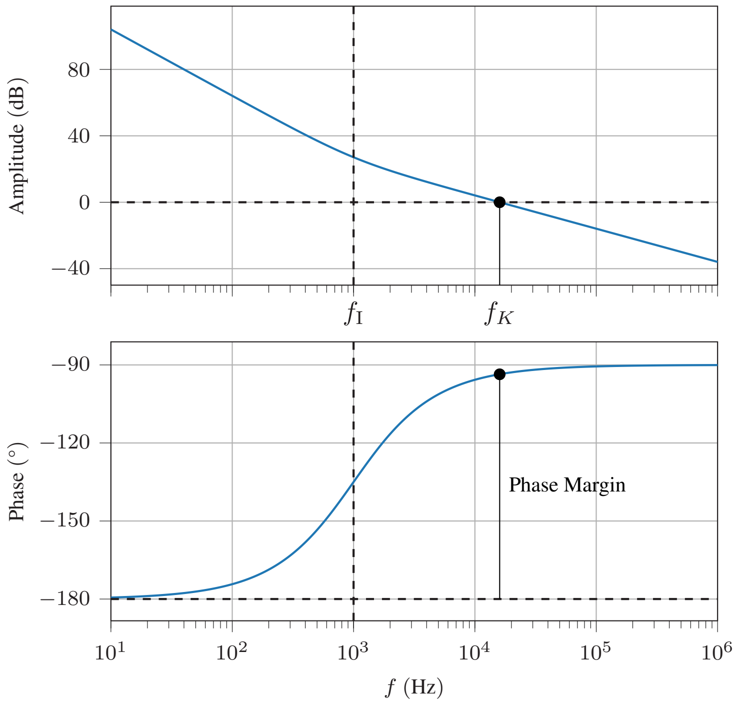

Figure 2.7: Bode diagram of the ideal PLL open loop transfer function

For an ideal PLL, the phase of H_{ol} is never below 180°. Therefore, the ideal PLL is always stable. However, real PLLs contain components with lowpass characteristics that introduce phase shifts such that the phase of the open loop transfer function becomes lower than −180°.

With the loop filter parameters K_{P} and K_{I}, f_{K} and f_{I} can be set to desired values. In addition, f_K is a measure of how quickly the PLL reacts to frequency noise of the VCO [61]. When designing a real PLL, K_{P} and K_{I} are chosen such that f_K is high enough to counteract all unwanted frequency changes and such that a sufficient phase margin for a stable closed loop is achieved.

2.2.2 Frequency Down Conversion

The mm-wave signal of the gyrotron needs to be down converted to a more suitable Intermediate Frequency (IF) range in which conventional PDs can operate. The down conversion with a mixer requires a frequency stable Local Oscillator (LO) at a fixed frequency f_{LO}. With low side injection, the resulting IF frequency of the VCO frequency f_{vco} is [18]:

$$f_{\mathrm{IF}} = f_{\mathrm{vco}} - f_{\mathrm{LO}} \tag{2.43}$$

The VCO signal is

$$s_{\mathrm{vco}} = \cos\left(2\pi f_{\mathrm{vco},0} t + K_{\mathrm{vco}} u_{\mathrm{in}} t\right) \tag{2.44}$$

where u_{in} is the input voltage of the VCO and $f_{\mathrm{vco},0}$ the frequency at which the VCO oscillates with 0 V input voltage. The LO generates a signal s_{LO} at a single frequency with phase noise ϕ_{noise}:

$$s_{\mathrm{LO}} = \cos\left(2\pi f_{\mathrm{LO}} t + \phi_{\mathrm{noise}}\right) \tag{2.45}$$

An ideal mixer multiplies the two signals. The mixer output signal is

$$\begin{aligned} s_{\mathrm{mixer}} &= \cos\left(2\pi f_{\mathrm{LO}} t + \phi_{\mathrm{noise}}\right) \cos\left(2\pi f_{\mathrm{vco},0} t + K_{\mathrm{vco}} u_{\mathrm{in}} t\right) \\ &= \frac{1}{2}\Bigg(\cos\Big(2\pi\left(f_{\mathrm{LO}} - f_{\mathrm{vco},0} t\right) + \phi_{\mathrm{noise}} - K_{\mathrm{vco}} u_{\mathrm{in}} t\Big) \\ &\qquad + \cos\Big(2\pi\left(f_{\mathrm{LO}} + f_{\mathrm{vco},0}\right) t + \phi_{\mathrm{noise}} - K_{\mathrm{vco}} u_{\mathrm{in}} t\Big)\Bigg) \end{aligned} \tag{2.46}$$

The cosine term with $f_{\mathrm{LO}} + f_{\mathrm{vco},0}$ has a high frequency content. This content can be suppressed with a lowpass filter. With Equation 2.43, the mixer output is

$$\frac{1}{2}\cos\left(2\pi f_{\mathrm{IF},0} + K_{\mathrm{vco}} u_{\mathrm{in}} t - \phi_{\mathrm{noise}}\right) \tag{2.47}$$

which contains the wanted phase information needed for the PLL and the unwanted phase noise of the LO.

With the frequency down conversion, the set frequency for the VCO is given by:

$$f_{\text{set}} = f_{\text{LO}} + N f_{\text{ref}} \tag{2.48}$$

2.2.3 Phase Frequency Detectors

A multitude of PDs are available for PLL systems [103]. PDs are optimal if the VCO frequency and set frequency are the same. The pull-in range is defined as the maximal frequency difference with which the PLL can still pull the VCO frequency onto the set frequency [7]. PLL systems with a PD have a finite pull-in range. For gyrotrons, the difference from the oscillating frequency and the set frequency may be several MHz. Therefore, PDs are unsuitable for gyrotron frequency stabilization.

Phase Frequency Detectors (PFDs) [104] not only detect phase differences, but also frequency differences. If the VCO frequency is the same as the set frequency, the PFD output is proportional to the phase difference between VCO and reference. If the VCO frequency is different from the set frequency, the PFD guarantees that the VCO reaches the set frequency. PLL systems with a PFD have theoretically an infinite pull-in range, and are therefore suitable for gyrotron PLLs.

The schematic of a PFD is shown in Figure 2.8 [7]. The PFD uses digital logic components. Two D-flipflops are triggered with the rising edges of the reference signal s_{ref} and the VCO signal s_{vco}, respectively. Therefore, a sinusoidal signal needs to be transformed into a rectangular waveform that is suitable to trigger the D-flipflop.

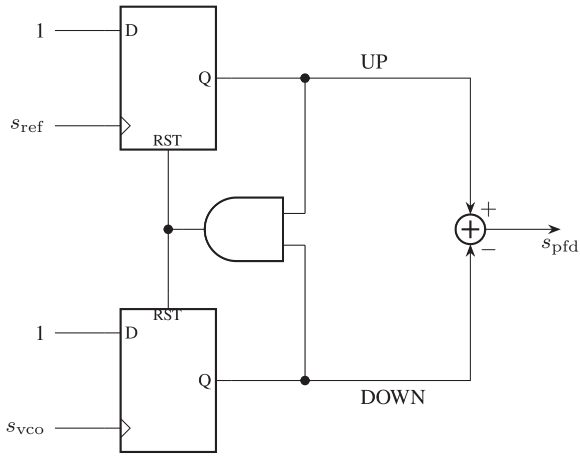

Figure 2.8: Principle of Phase Frequency Detector

The PFD detects the time difference Δt between the rising edges of the s_{ref} and s_{vco}. If reference and VCO have the same frequency, relating the time difference to the reference period results in the phase difference of the two signals:

$$\Delta\phi = 2\pi\frac{\Delta t}{T_{\mathrm{ref}}} = 2\pi\frac{t_{\mathrm{ref},\uparrow} - t_{\mathrm{vco},\uparrow}}{T_{\mathrm{ref}}} \tag{2.49}$$

where $t_{\mathrm{ref},\uparrow}$ and $t_{\mathrm{vco},\uparrow}$ are the points in time at which the reference and VCO have a rising edge, respectively.

The time difference Δt is encoded in the pulse lengths of the UP and DOWN signals. The separation into UP and DOWN signals allows to distinguish between positive (VCO leads the reference) and negative (VCO lags behind the reference) phase differences. Thus, the full range with which the PFD captures the phase difference correctly is from -2π to 2π. Due to phase wrapping, phase differences larger than 2π are mapped onto the -2π to 2π range, leading to cycle slipping (Section 2.2.4).

If the reference and VCO signal have the same frequency and a phase offset, the PFD outputs pulses, where the length of the pulse is proportional to the phase difference. If the VCO lags behind the reference, only DOWN pulses are generated and if the VCO leads the reference, only UP pulses are generated. By taking the average of the pulses, a signal that is directly proportional to the phase difference is obtained. The UP and DOWN signal indicate into which direction (faster or slower) the VCO needs to be changed to result in zero phase difference with the reference.

If the frequency of the VCO frequency is higher than the reference frequency, the UP signal is much longer high and has a non-linear dependence on the frequency difference. The same applies for the DOWN signal, if the VCO frequency is lower than the reference frequency.

2.2.4 Cycle Slipping

The linear theory described in Section 2.2.1 only applies if the VCO is already phase-locked onto the reference [7]. Cycle slipping is a nonlinear effect [105], and occurs if reference and VCO have different frequencies. It increases the time until the VCO frequency is locked onto the set frequency.

In Figure 2.9, the dependence of the PFD output on the phase difference between the VCO and the reference is shown. The output is linear from -2π to 2π. If the phase difference is outside of this range, phase wrapping occurs, leading to cycle slipping. For example, a phase difference of $\frac{5}{2}\pi$ is the same as $\frac{1}{2}\pi$.

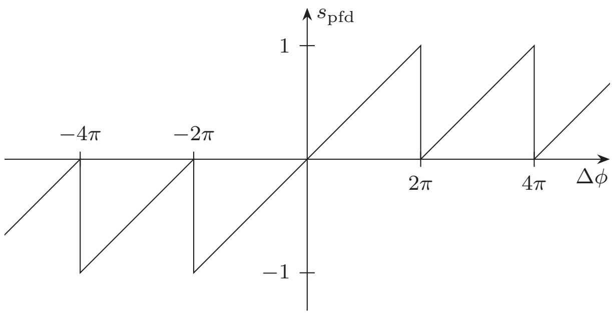

Figure 2.9: Dependence of PFD output on phase difference between VCO and reference

3 Phase-Locked Loop for MW-Class Gyrotrons

To use a PLL system on MW-class gyrotrons, the frequency behavior of the gyrotron on different operating parameters is analyzed in this chapter. At a fixed operating point, the gyrotron frequency dependence on the accelerating voltage can be linearized. Thus, the gyrotron can be considered as a VCO for the PLL system.

The theory of PLL frequency stabilization from Section 2.2 is applied for MW-class gyrotrons. The required components for the PLL system are characterized, and a PLL system for the W7-X gyrotrons is designed. Finally, the implementation of the frequency stabilization system for the W7-X gyrotrons is presented.

3.1 The Gyrotron as Voltage Controlled Oscillator

Determining the exact frequency of the excited $\mathrm{TE}_{m,n}$ mode requires solving the self-consistent gyrotron differential equations [65], [67]. This section analyzes the relevant operating parameters that change the excited frequency for the frequency stabilization control system.

The gyrotron is a non-isochronous oscillator [106], and the oscillation frequency depends on the oscillation amplitude. The electric field amplitude at the cavity determines how much the electrons are decelerated or accelerated [67]. Thus, the phase bunching mechanism not only depends on the initial frequency difference between the electromagnetic wave frequency and electron cyclotron frequency, but also on the electric field amplitude in the interaction region.

The parameters that directly influence the interaction mechanism are presented. However, these interaction parameters cannot be directly controlled and depend on other external operating parameters, which can be used by a control system to change the frequency. The frequency dependence on the different parameters is investigated with simulations on the TH1507 gyrotron. Furthermore, the frequency noise during the gyrotron operation is described, and the frequency down shift at the start of a pulse is explained.

3.1.1 Frequency of the Excited TE Mode

The frequency of the excited $TE_{m,n}$ mode depends on:

- Cavity geometry
- Electron beam parameters

An important parameter of the cavity geometry is the radius of the cavity midsection r_{cav} (Section 2.1.3), which changes the cut-off frequency of the excited $TE_{m,n}$ mode (Equation 2.22 and Equation 2.23). The cavity midsection radius cannot be actively controlled during operation.

For the electron beam parameters at the cavity, the frequency depends on

- Electron cyclotron resonance frequency
- Electron pitch factor
- Electron beam current

The electron cyclotron resonance frequency mainly influences the frequency of the excited $TE_{m,n}$ mode through the resonance condition as described by Equation 2.17. The magnetic field at the cavity and the electron kinetic energy change the electron cyclotron resonance frequency independently (Equation 2.3). Therefore, the magnetic field strength and the electron kinetic energy could be used to control the gyrotron frequency. The other electron beam parameters, which are the pitch factor and the beam current, influence the interaction mechanism, and could also be used for a frequency control system.

3.1.2 Control Parameters to Change the Frequency

The parameters in Section 3.1.1 cannot be directly controlled during gyrotron operation and depend on other external parameters. In the following, the relevant operating parameters are presented, and their suitability for use in a frequency control system is discussed.

The accelerating voltage changes the electron kinetic energy (Equation 2.15) and the pitch factor (Equation 2.20). The influence of the accelerating voltage on the electron kinetic energy, pitch factor and excited frequency is investigated for diode-type MIGs in Section 3.1.3. The high-voltage power supplies that are connected to the cathode and to the anode generate the accelerating voltage (Equation 2.18). These can be used for frequency control.

In diode-type MIGs, the electric field at the emitter E_{E} and U_{acc} cannot be changed independently, whereas in triode-type MIGs, the E_{E} depends on the modulation anode voltage, which can be independently varied by changing the potential on the modulation anode (as described in Section 2.1.3 and Figure 2.4). Thus, a frequency stabilization by changing the pitch factor is only possible for gyrotrons with a triode-type MIG.

The magnetic field strength at the cavity depends on the magnet coil current. The major challenge is the large time constant of the superconducting magnetic system. The speed with which the coil current can be changed is determined by the large inductance of the superconducting magnet [107]. The time scale to change the magnetic field is in the range of 40 mT/s [108], [109].

Due to the thermionic emission in MIGs, the beam current mainly depends on the emitter temperature [82]. The emitter is heated with a filament, and the filament temperature is controlled with the filament current I_{F}. Changing the gyrotron frequency with variation of filament current is unsuitable, as I_{F} changes the emitter temperature on a slow time scale [110]. Specifically, reducing the temperature causes high time delays, because no active cooling of the emitter is employed. In addition, two other effects cause changes of the electron beam current, which lead to changes of the gyrotron output frequency:

- Due to the Schottky effect [22], [82], the electric field at the emitter changes the beam current.
- Emission cooling [111], [112] reduces the temperature of the emitter and the beam current.

3.1.3 Simulations on Gyrotron Frequency Dependence

The frequency dependence on the electron beam parameters is investigated by simulating the W7-X-gyrotron TH1507 designed by KIT and manufactured by *THALES* [36]. The simulations are calculated with the code package *EURIDICE* [113], which is a time-dependent, multimode and self-consistent interaction code. Because the frequency dependence of the main operating mode $\mathrm{TE}_{28,8}$ is investigated, interaction simulations are conducted in this section only with the $\mathrm{TE}_{28,8}$, without consideration of other competitive modes.

In each simulation, the influence of the following parameters on the frequency of the operating TE mode is analyzed:

- Static magnetic field strength
- Electron kinetic energy
- Electron pitch factor
- Accelerating voltage

After the simulation has reached a stable point, an average of the last 150 µs is calculated for the excited frequency values. The output power at the end of the cavity for the different operating parameters is also shown.

Table 3.1: Operating point for interaction simulations with *EURIDICE*

Magnetic Field	B_{cav}	5.60	T
Kinetic Energy	W_{kin}	80	keV
Beam Current	I_{beam}	40	A
Pitch Factor	α	1.3	
Guiding Center Radius	r_{g}	10.1	mm

The operating point for the simulations is based on [36]. The input parameters for the simulation are shown in Table 3.1. For the following simulations, the corresponding parameter is swept, while the other parameters are kept constant.

Furthermore, simulations of the frequency dependence on the accelerating voltage are conducted. The electron gun is simulated with the code package *ESRAY* [114] to obtain the electron beam parameters, which are used for the interaction calculations with *EURIDICE*.

Sweep of Static Axial Magnetic Field Strength

For the simulations, the maximal field strength in the cavity is varied and the magnetic field profile is scaled accordingly with *EURIDICE*. In Figure 3.1, the power and frequency for different magnetic field strengths is shown. The magnetic field strength was swept between 5.59 T to 5.65 T. The frequency dependence is approximated linearly, which results in a slope of 1.05 MHz/mT. The output power also changes with the magnetic field, and a change in frequency of 60 MHz results in a power change of 400 kW.

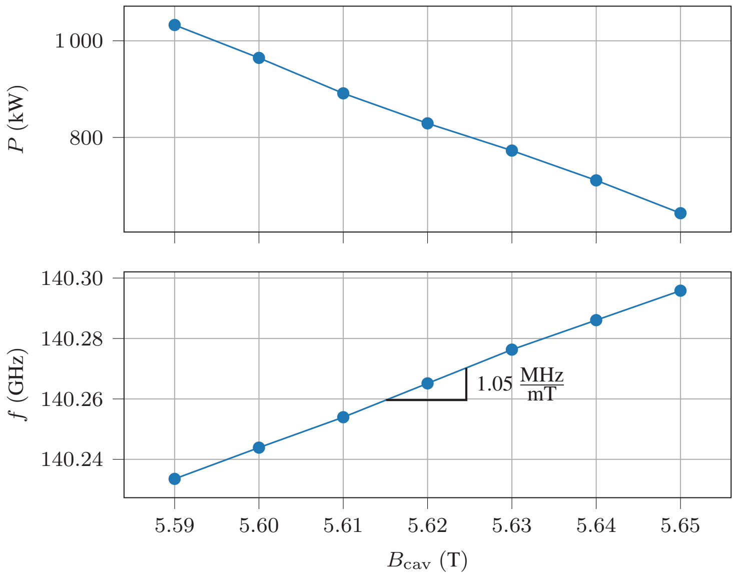

Figure 3.1: Calculated power and excited frequency with *EURIDICE* for different magnetic field strengths B_{cav} at the cavity

Sweep of Electron Kinetic Energy

The kinetic energy is swept between 70 keV to 82 keV. In Figure 3.2, the power and frequency for different kinetic energy values is shown. The frequency dependence on small changes of the kinetic energy is linear with a slope of −9.90 MHz/keV. The output power also depends on the kinetic energy. Changing the frequency with the kinetic energy by 10 MHz results in a power change of 150 kW.

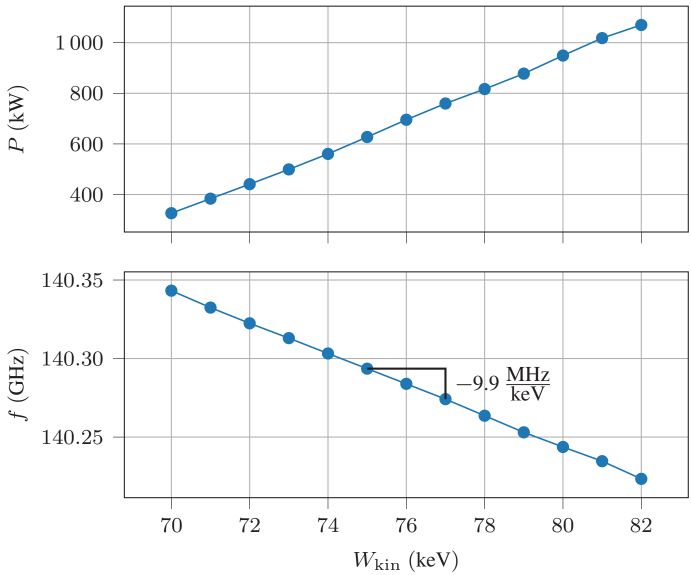

Figure 3.2: Calculated power and frequency of the $TE_{28,8}$ mode with *EURIDICE* for different electron kinetic energy values W_{kin}

Sweep of Electron Pitch Factor

The pitch factor α is swept between 1.2 to 1.5. For the simulation, the parameters from Table 3.1 were taken. In Figure 3.3, the power and exited frequency for different kinetic energy values are shown. A linear regression results in a slope of 166 MHz per unit of α. The output power varies by 40 kW for a frequency change of 10 MHz, which are lower power variations as with the kinetic energy.

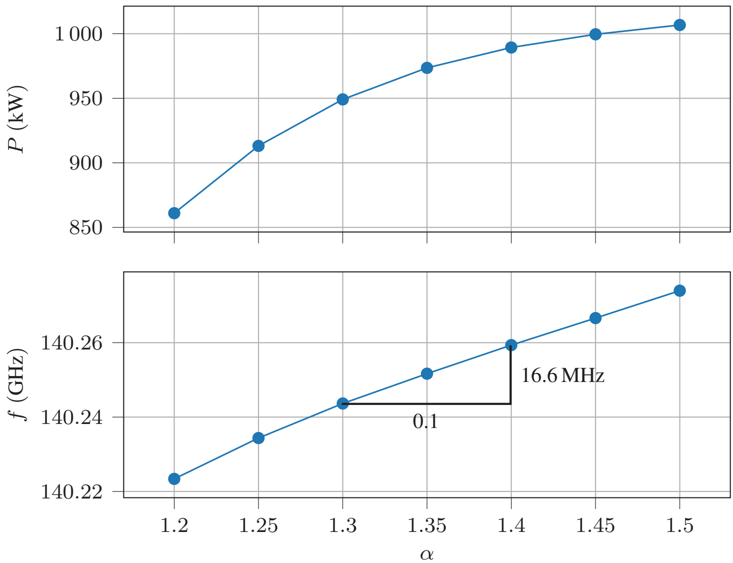

Figure 3.3: Calculated power and frequency of the $TE_{28,8}$ mode with *EURIDICE* for different pitch factor values α

Sweep of Accelerating Voltage

The simulation studies made in the previous sections are interaction parameters and influence independently the gyrotron frequency. The accelerating voltage is an external operating parameter, and changes not only the electron kinetic energy, but also the pitch factor (Equation 2.20). Specifically, in gyrotrons with diode-type a MIG, the pitch factor cannot be varied independently. Therefore, the total influence of the accelerating voltage on the frequency through the electron kinetic energy and pitch factor is examined.

The electron beam parameters are calculated with *ESRAY* and are given as input into *EURIDICE*. The magnet coil currents are calculated such that the same electron beam parameters and magnetic field as in Table 3.1 are achieved. In Figure 3.4, the kinetic energy, pitch factor, power and exited frequency for different accelerating voltages are shown.

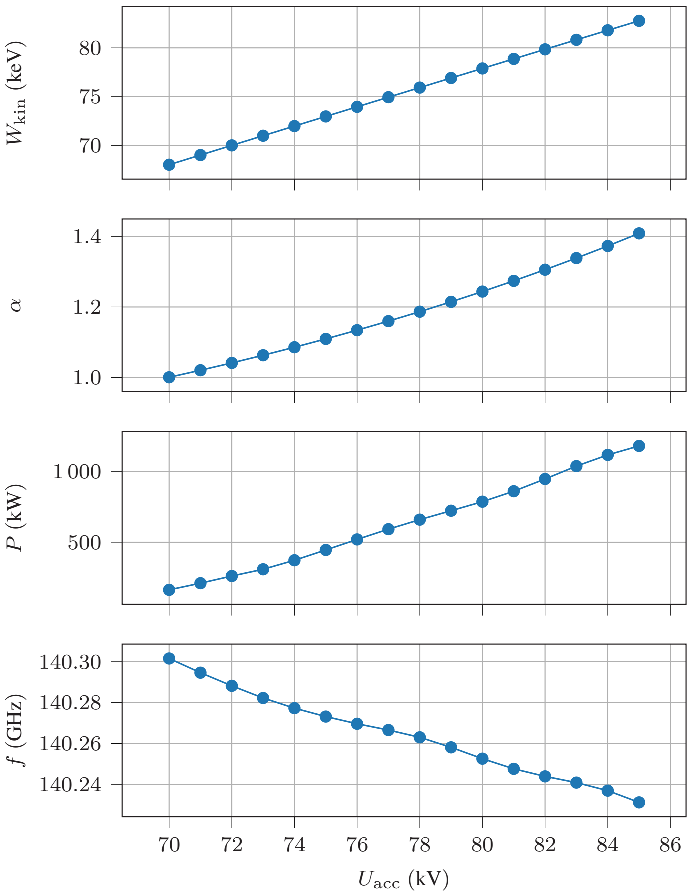

Figure 3.4: Calculated electron beam parameters (with *ESRAY*), power and frequency of the $\mathrm{TE}_{28,8}$ mode (with *EURIDICE*) for different accelerating voltages

Both, kinetic energy and pitch factor, depend on the accelerating voltage. The frequency dependence on the kinetic energy has a negative slope (Figure 3.2), while the one on the pitch factor has a positive slope (Figure 3.3). For the frequency dependence on the accelerating voltage in Figure 3.4, the changes from kinetic energy (negative slope, Figure 3.2) and pitch factor (positive slope, Figure 3.3) counter each other. But the frequency change from the kinetic energy dominates and the resulting slope on the accelerating voltage is also negative. The frequency dependence on the accelerating can still be linearized for small changes. A linear regression results in a slope of $-4.44\,\mathrm{MHz/kV}$.

3.1.4 Frequency Noise of Gyrotrons

Under ideal conditions, the electron beam parameters and cavity radius remain constant during the gyrotron pulse, and the excited TE mode oscillates at exactly one frequency, resulting in a single peak at the specific frequency in the spectrum. In a real MIG, the electrons do not have all exactly the same parameters (as described in Section 2.1.1). With consideration of a statistical distribution of the electron beam parameters (spread), the frequency spectrum of the excited TE mode changes. In the spectrum, the spread of the electron beam parameters results in a broadening of the frequency peak and a higher phase noise.

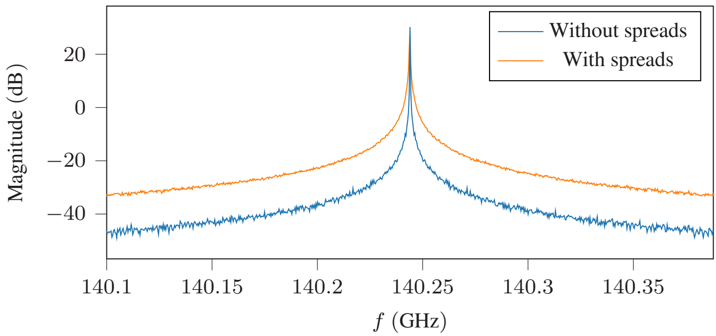

Figure 3.5: Spectrum of the excited $TE_{28,8}$ mode calculated with *EURIDICE* for the TH1507 gyrotron. The spectra are calculated without (blue) and with (orange) spreads of the electron beam parameters, and are constant over the simulation time.

The broadening of the frequency peak due the spread of the electron beam parameters is exemplary shown in Figure 3.5. The excitation of the $TE_{28,8}$ mode is simulated using *EURIDICE* without and with consideration of spread values for the electron beam parameters. The simulation parameters are shown in Table 3.2.

Table 3.2: Parameters used for the calculation with *EURIDICE* of the frequency spectrum. The $TE_{28,8}$ mode is excited in the TH1507 gyrotron

B_{cav}	(T)	5.60			
I_{beam}	(A)	40			
$\overline{r}_{\mathrm{g}}$	(mm)	10.1	Δr_{g}	(%)	1.60
$\overline{\alpha}$		1.3	$\Delta\alpha$	(%)	5.0
$\overline{\gamma}$		1.157	$\Delta\gamma$	(%)	0.01
$\overline{W}_{\mathrm{kin}}$	(keV)	80.0			

In Figure 3.5, the calculated spectra from *EURIDICE* are shown. The calculated spectrum without the spread of the electron beam parameters has a clear main peak at a single frequency. Larger spreads of the electron beam parameters result in larger phase noise. A clear main peak at a specific frequency is still present.

The statistical distribution of the electron beam parameters does not consider a change of their average values over time, which happens under real conditions during a gyrotron pulse. These parameter variations over time result in an unwanted frequency modulation and frequency shifts, and deteriorate the long-term frequency behavior.

The operating parameter changes over time result from noise of the gyrotron auxiliary components such as power supplies. For example, the noise in the power supply for the cathode voltage results in variations of the kinetic energy of the electrons.

The depression voltage (Equation 2.13) changes the electron kinetic energy and depends on the electron beam neutralization (as described by Equation 2.16). Therefore, changes in the neutralization cause noise in the gyrotron frequency. Furthermore, the cavity midsection radius changes over time due to heating from ohmic losses, leading to unwanted frequency shifts. In the following, the influence of the cavity midsection radius and electron beam neutralization on the gyrotron frequency is investigated for the TH1507 gyrotrons with *EURIDICE*. For the simulations, the operating point from Table 3.1 is used.

Change of Cavity Midsection Radius

To change the cavity midsection radius, the existing cavity geometry of the TH1507 gyrotron is scaled such that the cavity midsection radius corresponds to the desired radius. In Figure 3.6, the excited frequency for different cavity radii is shown. The cavity radius is swept from -10 µm to 10 µm around its nominal value of 20.48 mm. The frequency dependence on small changes of the cavity radius can approximated linearly for the operating point. A linear regression results in a slope of -6.5 MHz/µm. Already changes in the µm range result in frequency variations in the MHz range. To achieve a frequency stability of 1 MHz during a free-running operation, the cavity radius cannot vary more than 154 nm.

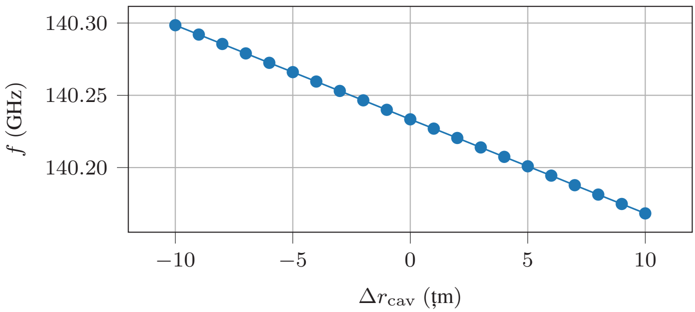

Figure 3.6: Frequency of the $TE_{28,8}$ mode for different cavity radii $r_{\mathrm{cav}} = 20.48\,\mathrm{mm} + \Delta r_{\mathrm{cav}}$

Change of Electron Beam Neutralization

In Figure 3.7, the excited frequency for different neutralization levels η_{neut} of the electron beam is shown. The electron beam parameters are calculated with *ESRAY* for the neutralization levels between 0 % to 85 %, and the frequency of the $TE_{28,8}$ is calculated with interaction simulations using *EURIDICE*. An increase of the neutralization of 10 % results in a decrease of the frequency of 9 MHz.

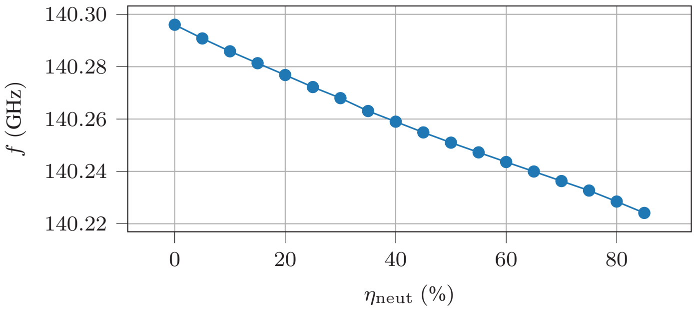

Figure 3.7: Excited frequency for different electron beam neutralization levels η_{neut}

3.1.5 Frequency Down Shift at Gyrotron Start-Up

At the beginning of a pulse, two phenomena occur inside the gyrotron which lead to a large frequency down shift in the range of hundreds of MHz [48]:

- Cavity expansion due to wall heating
- Space charge neutralization of the electron beam

Because the gyrotron cavity wall is not an ideal conductor, ohmic losses occur inside the cavity wall, as soon as the TE mode is excited. The ohmic losses heat the cavity wall, which leads to expansion of the cavity wall and to an increased cavity wall radius. A cooling system is installed inside the gyrotron to prevent the cavity wall from overheating. However, specifically at the beginning of a pulse, the cooling system needs time to react to the sudden temperature change of the cavity wall. The cavity wall radius increases until the cooling system cools down the cavity wall such that an equilibrium is reached.

The gyrotron frequency decreases with an increase of the cavity radius (as described in Section 3.1). Therefore, the frequency shifts to lower frequencies until the cavity wall radius stops increasing, which is after several hundreds of ms.

Another parameter that changes during the gyrotron start-up is the electron beam neutralization. Immediately at the start of the pulse, no ions are inside the gyrotron and the electron beam is not neutralized. As some residual gas is inside the gyrotron (Section 2.1.1), the residual gas gets ionized. The ions neutralize the electron space charge, leading to a lower depression voltage and a higher electron kinetic energy [78].

Due to the electron beam neutralization, the electron kinetic energy increases over time (until the maximal neutralization is reached). As described in Section 3.1, the gyrotron frequency decreases with an increase of the electron kinetic energy. The frequency down shift from the electron beam neutralization is in the range of tens of MHz.

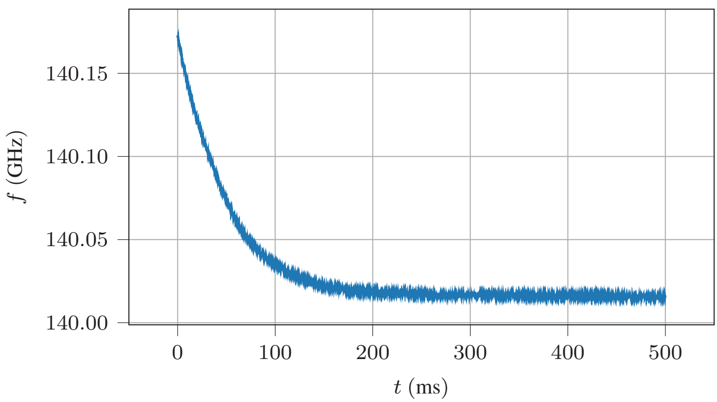

Figure 3.8: Frequency down shift of the VGT8141A gyrotron from manufacturer *CPI* during the first 500 ms of a pulse

Typically, the duration of both effects is in the hundreds of ms range and the frequency down shift is in the range of hundreds of MHz. In Figure 3.8, an example of the frequency down shift is shown. The frequency curve is measured experimentally for the VGT8141A gyrotron from manufacturer *CPI*. The

VGT8141A gyrotron is operated at an accelerating voltage of 80 kV with a beam current of 40 A. During the first 200 ms the frequency shifts exponentially from 140.175 GHz to 140.025 GHz.

3.1.6 Summary

The gyrotron frequency dependence on different parameters is analyzed. It is shown that noise in the operating parameters, thermal expansion of the cavity or different vacuum conditions lead to unwanted frequency variations of the free-running gyrotron. Stabilizing the gyrotron frequency with an external control system requires an operating parameter that can be controlled fast enough to counter these frequency variations.

The most suitable parameter for a frequency stabilization system of gyrotrons with a diode-type MIG is the accelerating voltage. Simulation on the TH1507 gyrotron show that for a fixed operating point, the gyrotron frequency can be approximated with a linear dependence on small variations of the accelerating voltage. Thus, for a PLL-based frequency stabilization system, the gyrotron can be modeled as VCO.

3.2 Design of the PLL System for W7-X Gyrotrons

Although the gyrotron can be approximated as a VCO, the ideal PLL described in Figure 2.6 can not be directly used as a frequency stabilization system for MW-class gyrotrons. To determine the control parameters for the PLL system, the high-voltage Power Supply (PS) system at W7-X is characterized.

The accelerating voltage of the gyrotron is controlled with: (i) the body PS and (ii) the cathode power PS. The cathode PS provides the current of the electron beam, which is in the range of 40 A. The body PS changes the potential of the gyrotron body, and needs to provide the currents that charge the capacity of the gyrotron body as well as the cable capacity between the body PS and gyrotron. At W7-X, the body voltage can be faster controlled than the cathode voltage, because the high-power cathode PS also provides the electron beam current, which is up to 50 A. Therefore, the gyrotron frequency is controlled via the body PS.

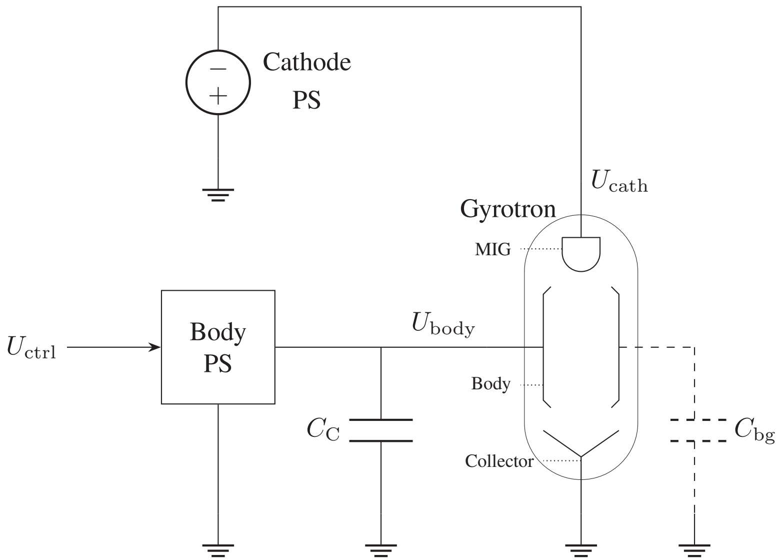

Figure 3.9: Structure of the power supplies for the W7-X gyrotrons. For the body PS, the gyrotron can be viewed as a capacitive load with the capacitance C_{bg}.

The structure of the high-voltage PS system is shown in Figure 3.9, and a detailed description is presented in [115], [116]. For the PLL system, the body PS is modulated with U_{ctrl}. The total capacitance seen from the body PS limits the speed with which the body PS can modulate the body voltage U_{body}. The gyrotron is a capacitive load for the body PS. The total capacitance C_{tot} is the cable capacitance C_{C} in parallel with the gyrotron body capacitance C_{bg}:

$$C_{\mathrm{tot}} = C_{\mathrm{C}} + C_{\mathrm{bg}} \tag{3.1}$$

The cable capacitance at W7-X is rated with 50 pF/m. With a length of 9 m from the body PS to the gyrotron, the total cable capacitance is 450 pF.

To calculate control parameters for the PLL system, the gyrotron capacitance is determined, and the body PS is characterized. Furthermore, the final PLL system is simulated with the optimal control parameters. Finally, the noise of the cathode PS is characterized, since it adds noise to the PLL system.

3.2.1 Determination of the Gyrotron Capacity

Considering the electric components that describe the PLL system, a limiting part of the gyrotron operation is the capacity between gyrotron body and ground. A greater capacity needs higher current to charge it to the required voltage level. In combination with the current limit given by the body PS, the gyrotron capacity limits the speed with which the accelerating voltage can be changed.

The capacitance of the W7-X TH1507 gyrotron is theoretically investigated with the *FEMM* software [117]. *FEMM* is a finite element solver for 2D and axisymmetric electrostatic problems. With *FEMM*, the charges on the cathode, anode and components on ground potential are calculated for the geometry of the TH1507 gyrotron. The potentials are set to: $U_{\mathrm{cath}} = -55\,\mathrm{kV}$ and $U_{\mathrm{body}} = 25\,\mathrm{kV}$. The capacitance between body and ground is

$$C_{\mathrm{bg}} = \frac{Q_{\mathrm{body}} - Q_{\mathrm{ground}}}{2\left(U_{\mathrm{body}} - U_{\mathrm{ground}}\right)} \tag{3.2}$$

where $U_{\mathrm{ground}} = 0\,\mathrm{V}$. The obtained values for the charges from *FEMM* are:

$$\begin{aligned} Q_{\mathrm{body}} &= 3.12\,\mu\mathrm{C} \\ Q_{\mathrm{cath}} &= -1.71\,\mu\mathrm{C} \\ Q_{\mathrm{ground}} &= -1.41\,\mu\mathrm{C} \end{aligned}$$

With Equation 3.2, the body-to-ground capacity is C_{bg} is 90 pF.

The calculated gyrotron capacity is lower than the capacitance of the cable, which is 450 pF. Therefore, the cable capacitance is more significant for the body PS than the gyrotron body capacitance. If a faster control of the body voltage is required for the PLL system, a fast amplifier could be placed in series with the body PS directly at the gyrotron such that the cable capacitance is avoided.

3.2.2 Characterization of the Body Power Supply

The Institut für Plasmaforschung (IPF) at Universität Stuttgart designed and implemented the body PS for W7-X gyrotrons using a high-voltage amplifier in vacuum-tube technology. It serves the dual purpose of stabilizing the noise of the cathode PS and modulating the accelerating voltage for gyrotron output power modulation. A detailed description of the design and implementation of the body PS can be found in [115], [116].

For the frequency stabilization system, the dynamics of the body PS are investigated. A *PSpice* model of the W7-X body PS is available and described in detail in [115]. To analyze the transfer function of the body PS, a bode diagram is calculated using the *PSpice* model. In the simulation, a sinusoidal signal with 1 V amplitude is applied to the input of the body PS. The output voltage body PS is modulated in the range between 79 kV to 80 kV, corresponding to a gain of 1000 (60 dB).

The resulting bode diagram for amplitude and phase are shown in Figure 3.10. At low frequencies, the body PS has the set gain of 60 dB and no phase offset is between the input and the output voltage. The body PS exhibits lowpass characteristics, and the gain significantly decreases for high frequencies. The −3 dB cutoff frequency is 20 kHz, which is also described in [116].

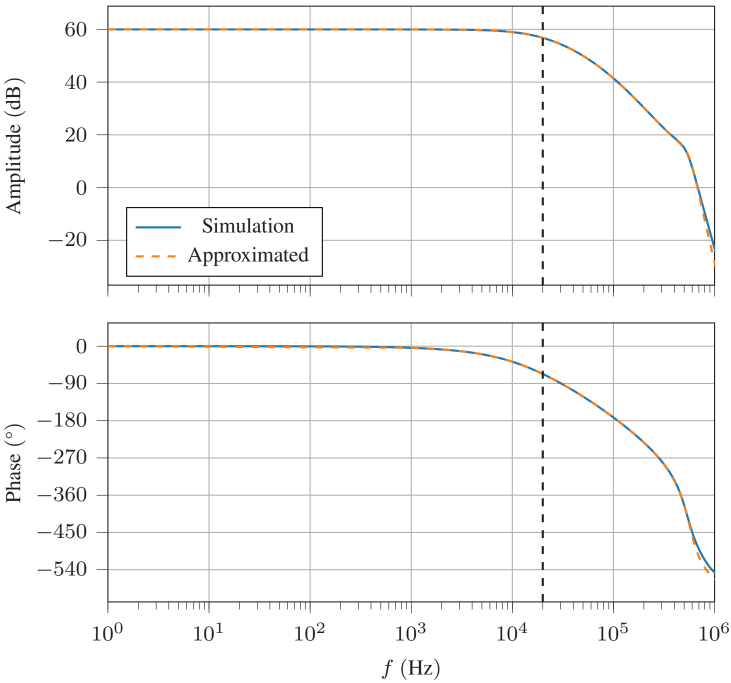

Figure 3.10: Bode diagram of the body power supply obtained with *PSpice* simulation

The transfer function of the body PS is approximated by a linear seventh order system, and the coefficients are determined by curve fitting. The approximated transfer function is shown in Figure 3.10. Differences between simulated and approximated transfer functions only occur at higher frequencies (> 500 kHz) and are negligible for the dynamics of the PLL.

3.2.3 Calculation of Control Parameters

With the approximation of the body PS transfer function in Section 3.2.2, a stability analysis of the W7-X gyrotrons is conducted to determine the loop filter parameters K_P and K_I for the PLL system. The W7-X gyrotrons are approximated as VCOs with the gain determined in Section 3.1.3. With the body PS, the PLL open loop transfer function is given by

$$\begin{aligned} H_{\mathrm{ol}}(s) &= H_{\mathrm{pfd}} H_{\mathrm{PI}} H_{\mathrm{bodyPS}} H_{\mathrm{vco}} \\ &= \frac{K_{\mathrm{pfd}} K_{\mathrm{vco}} \left(K_{\mathrm{P}} s + K_{\mathrm{I}}\right)}{s^2} H_{\mathrm{bodyPS}} \end{aligned} \tag{3.3}$$

Similar to Section 2.2.1, K is defined as

$$K = \frac{K_{\mathrm{pfd}} K_{\mathrm{vco}} K_{\mathrm{P}} K_{\mathrm{b}}}{N} \tag{3.4}$$

with the given gain factor $K_{\mathrm{b}} = 1000$. As long as $f_K = \frac{K}{2\pi}$ is smaller than the 3-dB cut-off frequency of the body PS (20 kHz), f_K is the frequency at which the open loop function crosses 0 dB. In Figure 3.10, the phase of the body PS transfer function drops significantly. Therefore, values for f_K higher than 20 kHz are unsuitable and result in an unstable control system.

For the calculation of the loop filter parameters during the experiments, first f_K is chosen. With K_{pfd} and K_{vco} known, K_{P} is calculated. Then, f_{I} is chosen for sufficient phase margin. K_{I} is calculated with Equation 2.42. An example is shown in Figure 3.11 with $f_K = 10$ kHz and different values for f_{I}. The fast drop of the phase after 20 kHz due to the body PS is significant and limits the values for f_K and f_{I}.

3.2.4 Simulation of the PLL System with Body Power Supply

Using *Simulink* [118] and *PSpice* [119], the full gyrotron PLL system with the body PS is simulated in time domain and the step response to a 1 MHz jump is investigated. Co-simulations with *Simulink* and *PSpice* using the body PS model are conducted. The PLL system is modeled in *Simulink* with the PFD from Section 2.2.3. The gyrotron is modeled as VCO. To restrain the requirements

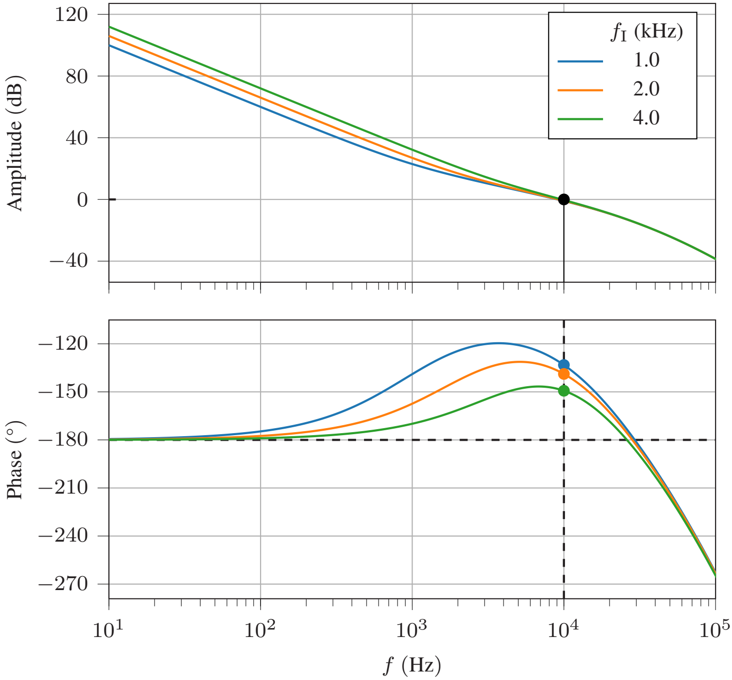

Figure 3.11: Bode diagram of the open loop transfer function of the gyrotron PLL including the body power supply. The dots in the phase plot are the phase margins for different values of f_I with $f_K = 10\,\mathrm{kHz}$.

on the temporal resolution of the simulations, the gyrotron VCO operates in the MHz regime instead of 140 GHz. For the dynamic behavior of control system, the frequency down conversion is not relevant and only the dynamics of the gyrotron VCO K_vco are necessary (Section 2.2.2). The loop filter parameters are calculated with Equation 3.4 and Equation 2.42 for specific f_K and f_I.

In Figure 3.12, the step response of the gyrotron VCO frequency to a 1 MHz jump of the reference signal is shown. The control loop parameters are $f_K = 16\,\mathrm{kHz}$ and $f_\mathrm{I} = 4\,\mathrm{kHz}$. The reference signal changes its frequency from 1 MHz to 2 MHz at 0 s. The body PS changes its voltage correspondingly such that the gyrotron VCO follows the frequency change of the reference. The step response

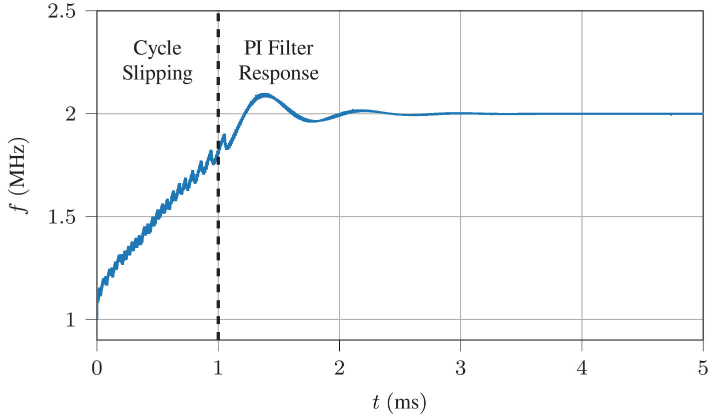

Figure 3.12: Step response of the gyrotron PLL system with the loop parameters $f_K = 16\,\text{kHz}$ and $f_\text{I} = 4\,\text{kHz}$

shows typical PI filter characteristics superimposed with cycle slipping behavior (as described in Section 2.2.4) during the first 1 ms. With the chosen control parameters, the VCO frequency fully settles on the set frequency after 3 ms.

Larger values for f_K or f_I increase the time until the VCO frequency reaches the reference frequency. However, during the simulations, larger values for f_K or f_I result in an unstable control system with the VCO frequency never settling on the reference frequency, but oscillating around it. This is also expected from linear PLL analysis in Section 3.2.3, where larger control parameter values result in unsuitable phase margins and in an unstable control system.

3.2.5 Characterization of the Cathode Power Supply

The cathode PS is built on the Pulse Step Modulation (PSM) technology [120] and was manufactured by *Ampegon Power Electronics AG*. The cathode PS is designed to deliver up to 65 kV with a current of 50 A in continuous operation.

With the PSM technology, multiple identical power supply modules output a high Direct Current (DC) voltage. These modules are switched, which introduces high-frequency noise.

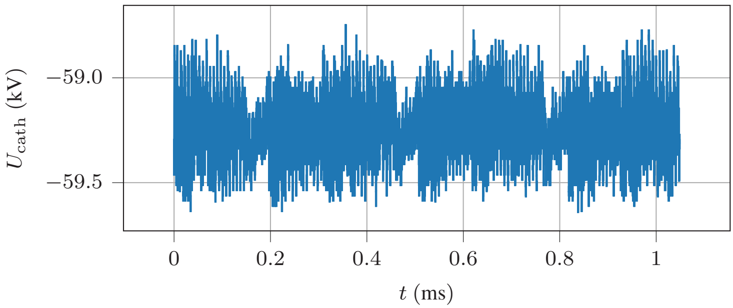

Figure 3.13: Noise of cathode power supply voltage

The noise on the cathode PS is characterized as 500 V peak-to-peak [116]. Although this is sufficient enough for the designed gyrotron ECRH operation at W7-X, the noise of the cathode PS is further investigated for the frequency stabilization circuit. Specifically, the frequency spectrum of the power supply is characterized. For the characterization, the cathode PS is operated loaded, and experiments with the gyrotron are conducted. The voltage of the cathode PS is measured during operation of the VGT8141A gyrotron with an accelerating voltage of 79.5 kV and a beam current of 36 A.

The cathode PS is set to a constant output voltage of 59.25 kV. The resulting curve is shown in Figure 3.13. The output voltage of the cathode PS is sampled with a frequency of 15.625 MHz. In the cathode voltage, periodic amplitude variations are present with a repetition rate of 0.3 ms (which corresponds to a frequency of 3.3 kHz).

To analyze the spectral noise of the PS, a Fourier transform of the cathode voltage is shown in Figure 3.14 from 0 kHz to 250 kHz and 0 kHz to 20 kHz. The cathode PS voltage is sampled with a frequency 488 kHz for a duration of 33.5 ms, which results in a frequency resolution of 29.8 Hz. In the lower frequency region, the

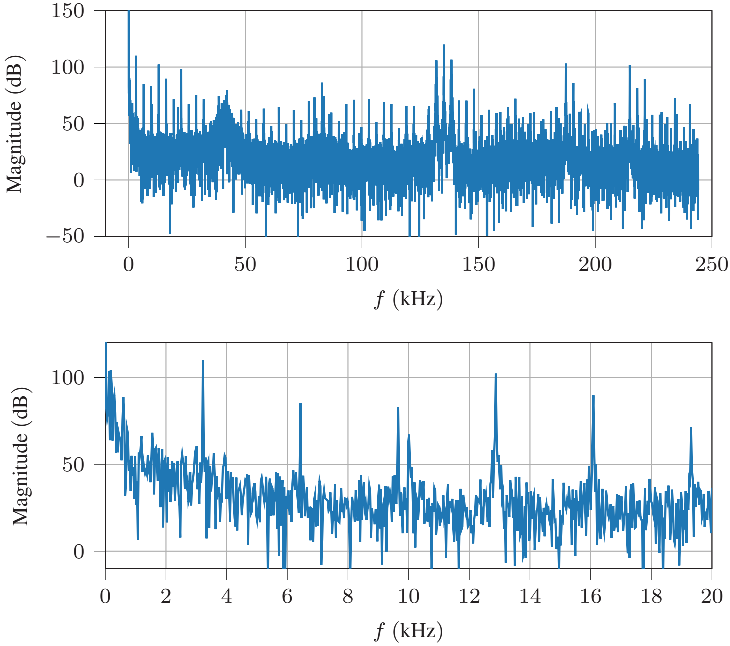

Figure 3.14: Spectrum of the cathode power supply noise from 0 kHz to 250 kHz and 0 kHz to 20 kHz

highest spectral line is at 3.3 kHz of which the harmonics are also present in the spectrum. The 3.3 kHz oscillations are also visible in the time domain in Figure 3.13. Other high spectral lines are near 135 kHz. Apart from the main peak at 135 kHz, side-bands arise at frequencies that are multiples of 3.3 kHz away from the main 135 kHz peak, which is a modulation of the 135 kHz oscillation with 3.3 kHz.

These spectral lines arise from the switching of the modules of the cathode PS and are inherent to the PSM technology. The same spectral lines at 3.3 kHz and 135 kHz are observed in all cathode power supplies at W7-X.

3.3 Implementation of the PLL System for W7-X

With the considerations in the previous section, a complete PLL system for the W7-X gyrotrons is design and implemented. Besides the earlier considerations, an easy integration into the W7-X systems is also important. An overview of the frequency stabilization system is shown in Figure 3.15. First, the gyrotron signal s_{gyro} is down converted from the mm-wave range to the required IF (in the MHz range). The resulting IF signal s_{IF} is fed into the digital PLL system, which outputs a control signal s_{ctrl}. The control signal is transmitted to the body PS and changes the body voltage to counteract the frequency variations. Furthermore, the IF signal is used to measure the gyrotron signal and determine the gyrotron spectrum.

Figure 3.15: Overview of the implemented frequency control system

The core implementation of the frequency stabilization system is done digitally, via a Field-Programmable Gate Array (FPGA). The digital implementation offers the advantage to change the control parameters without any changes of the hardware. Furthermore, the digital implementation also allows an easy integration into the W7-X systems. Thus, it can be used during experimental campaigns with the W7-X stellarator.

3.3.1 Frequency Down Conversion

A small part of the gyrotron mm-wave beam is picked up with a horn antenna at the mm-wave beam duct. This mm-wave gyrotron signal is transmitted over a waveguide system to the frequency down conversion system. In Figure 3.16, a diagram of the frequency down conversion is shown.

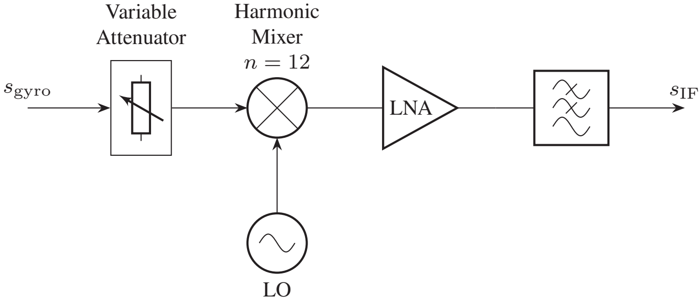

Figure 3.16: Frequency down conversion system

For the frequency down conversion, it is assumed that only the nominal TE mode is excited. Only the signal of the nominal TE mode is present and no other signal is in the image band of the frequency down conversion visible. Therefore, the image band does not need to be filtered out, and without the restrictions of an image band filter, the LO frequency can be placed as close as possible to the gyrotron frequency. The IF ranges from 10 MHz to 90 MHz.

To prevent damage to the mixer, the gyrotron signal is attenuated with a variable attenuator. The frequency down conversion is realized using a harmonic mixer. Compared to fundamental mixers, harmonic mixers have higher conversion losses. However, the frequency down conversion can afford higher losses, because the gyrotron signal has high power. The main advantage of harmonic mixers is the reduction on the requirements of the LO. Depending on the harmonic number, the LO does not need to be implemented in the mm-wave range but only in the 10 GHz to 20 GHz range. The frequency down conversion shall be used for the nominal 140 GHz operation and for the CTS diagnostic with a frequency at 174 GHz. A LO with a variable output frequency in the 10 GHz to 20 GHz range allows to use the same LO for the 140 GHz and 174 GHz operation.

The final implementation uses a harmonic mixer from manufacturer *RPG Radiometer Physics GmbH*. The harmonic mixer operates at the 12^{th} harmonic and is specified in D-band, ranging from 110 GHz to 170 GHz. However, since the cut-off frequency of the next upper mode is at 181.583 GHz, this mixer is also used for the 174 GHz gyrotron operation.

With the harmonic mixer operating at the twelfth harmonic, the LO needs a frequency of 11.67 GHz and 14.50 GHz to down convert the 140 GHz and 174 GHz, respectively. The Valon 5019 frequency synthesizer from manufacturer *Valon Technology* is used. The Valon 5019 operates up to 20 GHz with a maximal output power of 16 dBm.

After the harmonic mixer, the signal is amplified with a Low Noise Amplifier (LNA) and subsequently lowpass filtered with a cut-off frequency of 90 MHz.

3.3.2 PLL Implementation

After the frequency down conversion, the gyrotron signal is fed into the PLL system. The main components of the PLL system is the PFD and the PI filter.

The final system is implemented in a FPGA. Not only allows this for an easy integration into the W7-X system, but also allows for a flexible change in the control parameters. Moreover, the design can be changed for future advanced control systems. The low-cost off-the-shelf *CycloneV* from manufacturer *Intel* is used. The *CycloneV* is a System on Chip (SoC) combining FPGA and a Hard Processor System (HPS) with the operating system Linux. The Linux system allows to interface with the W7-X system and the PLL operating parameters are communicated over the HPS into the FPGA system.

Because the IF signal is a sinusoidal signal, it needs to be converted into a corresponding input signal for the FPGA. The input of the FPGA only accepts digital signals, where logic low corresponds to 0 V and logic high to 3.3 V. For the PFD, only the rising edges of the input signals are relevant. Therefore, the IF sinusoidal signal is converted into a rectangular waveform between 0 V to 3.3 V.

On the FPGA side of the *CycloneV*, the core of the PLL system is implemented: the N-divider, PFD and PI filter. The N-divider is a counter, which divides the frequency of the input signal by outputting a rising edge only every N^{th} rising edge of the input signal. The PFD from Figure 2.8 is implemented with two D-flip-flops. The duration of the UP and DOWN pulses from the PFD is captured with a 600 MHz counter, and the PI filter operates at a frequency of 100 MHz. After the PI filter, the signal is additionally lowpass filtered for the transmission to the body PS.

For the W7-X system, the control signal needs to be transmitted over fiber optics to the body PS. For this, a digital to fiber optics conversion is designed, which transforms the output of the PI filter into the transmission protocol that is used at W7-X.

4 Operation of a 140 GHz W7-X Gyrotron at 174 GHz for CTS Diagnostic

A CTS diagnostic at W7-X is implemented and first successful experiments are conducted for ion temperature measurements [121]. The CTS diagnostic uses one of the ECRH gyrotrons at its nominal frequency of 140 GHz as probing beam. During OP 1.2 at W7-X, the ion temperature measurements with the CTS diagnostic at 140 GHz are in reasonable agreement with the ion temperature measurements from the X-ray spectroscopy [121]. Operating the CTS diagnostic at the ECRH frequency results in strong noise from the electron cyclotron emission background (in the keV range), which deteriorates the SNR significantly [122]. Measuring other plasma parameters such as the fast ion velocity distribution function requires a SNR higher than ten [122], which is difficult to achieve with the electron cyclotron emission background at 140 GHz. Therefore, the CTS diagnostic is upgraded to an operating frequency of 174 GHz at which the electron cyclotron emission background is expected to be in the range of several electronvolt [123].

With the move to 174 GHz, the gyrotron also needs to change its operational frequency. Because the ECRH gyrotron is designed to operate at the plasma heating frequency of 140 GHz, the new operation at 174 GHz needs careful theoretical considerations. In [124], the operation at 174 GHz was theoretically investigated with simulation tools, specifically with *EURIDICE* [113], *Ariadne* [125] and *KarLESSS* [126].

Together with this, a new 7 T magnetic system is installed for the CTS gyrotron. Simulations with the new magnetic field profile of the 7 T system are conducted to find the optimal operating point, and the experimental results are presented.

4.1 Magnetic System for 174 GHz Operation

The new 7 T magnetic system is designed and manufactured by *Cryomagnetics*. A schematic of the new magnetic system is shown in Figure 4.1. The system consists of an Upper Main Coil (UMC), a Lower Main Coil (LMC), a High-field Main Coil (HMC), a Compensating Main Coil (CMC) and a Gun Trim Coil (GTC). The main difference to the existing magnetic system for the W7-X gyrotron is the HMC, which is located at the cavity midsection.

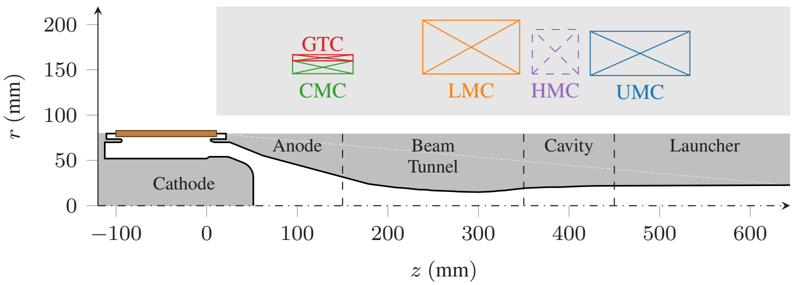

Figure 4.1: Coil configuration of the new 7 T magnetic system. The HMC coil is only added for the gyrotron operation at 174 GHz

Operation at 140 GHz using the new magnetic system requires the same magnetic field profile as with the originally used magnet. For the 140 GHz operation, the HMC is not used and the magnetic coil configuration is similar to the previous coil configuration. Thus, the magnetic field profile for the 140 GHz operation is also similar to the original magnetic field profile.

For the 174 GHz operation, the LMC and UMC cannot provide the required field strength of 7 T, and the HMC is included to obtain the required 7 T. The additional coil makes the field profile steeper than the one used for the calculations in [124], and simulations with the new magnetic system are conducted. The difference between the original and new magnetic field profile for 174 GHz operation are shown in Figure 4.2.

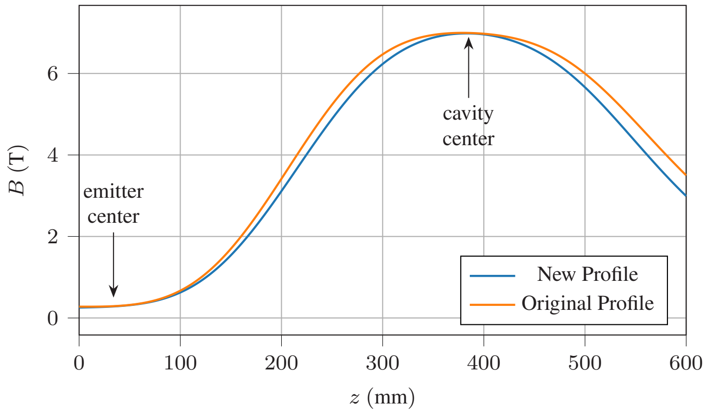

Figure 4.2: Comparison of the magnetic profile for the original and new magnetic system for the 7 T operation

4.2 Selection of Operating Mode

Possible operating modes for the 174 GHz operation are discussed in [124]. The most suitable modes are the $TE_{34,10}$ and $TE_{35,10}$ modes. Additionally, the $TE_{33,10}$ is also considered as candidate mode for the operation with the new magnetic system.

The reflection R of the diamond window is calculated with Equation 2.29 for the frequencies between 135 GHz to 180 GHz and is shown in Figure 4.3. The window has a thickness of $d_W = 1.799$ mm and is resonant for the frequencies

140 GHz and 175 GHz (as described with Equation 2.28). The cut-off frequency of each candidate mode is also shown in Figure 4.3, and the reflection for each candidate mode is evaluated.

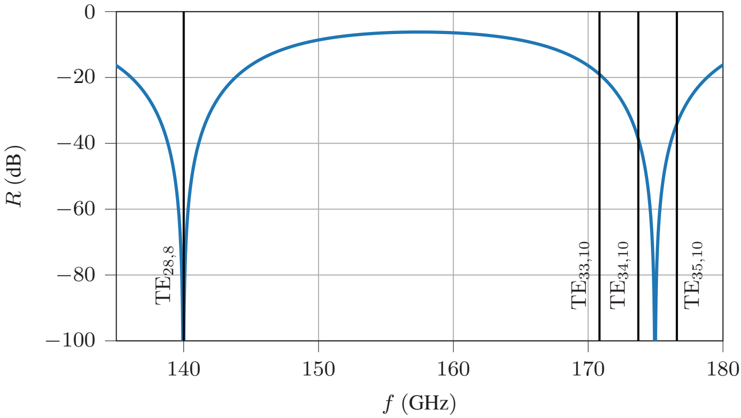

Figure 4.3: Reflection at the gyrotron window. The window is resonant for 140 GHz and 175 GHz. The frequencies of the different candidate modes are shown with the vertical black lines

In Table 4.1, the cut-off frequency, reflection at the window for the respective mode cut-off frequency and the relative caustic radius for each candidate mode are shown. As a reference, the mode parameters for the nominal 140 GHz $\mathrm{TE}_{28,8}$ are additionally given. The $\mathrm{TE}_{33,10}$ mode has the highest reflection at the window with 11.152 %.

The launcher is designed to convert the $\mathrm{TE}_{28,8}$ mode into a Gaussian-like beam. In order for the candidate modes to be optimally converted into a Gaussian-like beam, their caustic radius must be close to the caustic radius of the $\mathrm{TE}_{28,8}$ mode. In Table 4.1, the relative caustic radius is defined as:

$$r_{\mathrm{c,rel}} = \frac{r_{\mathrm{c}}}{r_{\mathrm{c},28,8}} \tag{4.1}$$

where r_c is calculated with Equation 2.24 for each candidate mode and $r_{\mathrm{c},28,8}$ is the caustic radius of the $\mathrm{TE}_{28,8}$ mode. In Table 4.1, the caustic radius of the $\mathrm{TE}_{35,10}$ mode is closest to the $\mathrm{TE}_{28,8}$ mode compared to the other candidate modes.

Table 4.1: Mode properties for nominal $\mathrm{TE}_{28,8}$ mode and each candidate mode

		$\mathrm{TE}_{28,8}$	$\mathrm{TE}_{33,10}$	$\mathrm{TE}_{34,10}$	$\mathrm{TE}_{35,10}$
Cut-off frequency at cavity	(GHz)	140.022	170.841	173.718	176.587
Reflection at window	(dB)	-94.0	-19.1	-38.6	-34.0
Reflection at window	(%)	0.002	11.152	1.176	1.996
Relative caustic radius		1	0.96	0.98	0.99

4.3 Simulation Results

The quasi-optical system is analyzed, and the results from [124] are verified with simulations of the new magnetic system. The electron beam parameters are calculated with *ESRAY* and the interaction is simulated with *EURIDICE*. The magnetic coil currents are determined to optimize excitation of the candidate modes inside the cavity, and the simulation results for each candidate mode are presented.

4.3.1 TE Mode Conversion into Gaussian TEM Mode

The quasi-optical system is analyzed for the candidate modes $\mathrm{TE}_{33,10}$, $\mathrm{TE}_{34,10}$ and $\mathrm{TE}_{35,10}$ with *KarLESSS*. The candidate modes must fulfill two requirements:

- the Gaussian-like beam exists the gyrotron window through the center and does not hit its copper cuff

- the Gaussian-like beam passes through the tunnel into the beam duct without hitting the tunnel wall

To determine if the two requirements are fulfilled, the electric field is evaluated at two different planes: (a) the gyrotron window and (b) the exit of the tunnel leading into the beam duct. The simulation setup is shown in Figure 4.4. The geometries of the launcher and three mirrors are used for the calculations with *KarLESSS*. For each simulation, the respective candidate mode is inserted at the entrance of the launcher.

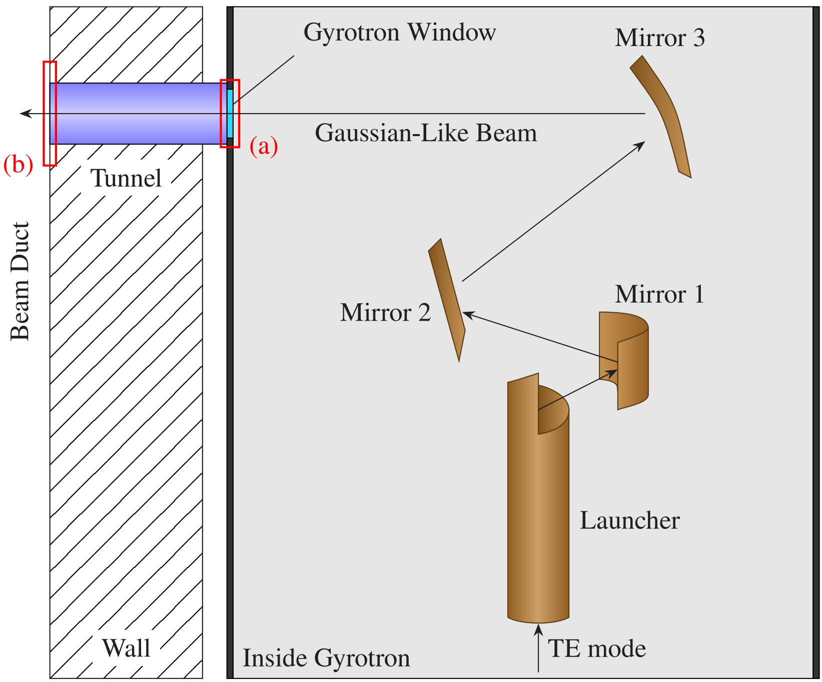

Figure 4.4: Geometry for the simulations of the quasi-optical system with *KarLESSS*. The electric field is evaluated at two different planes: (a) gyrotron window and (b) tunnel exit to beam duct.

In Figure 4.5, the calculated electric field distribution at the gyrotron window plane is shown for the nominal $TE_{28,8}$ and the candidate modes. The electric field profiles are normalized to the maximum value for each TE mode. The black ring represents the copper cuff of the window.

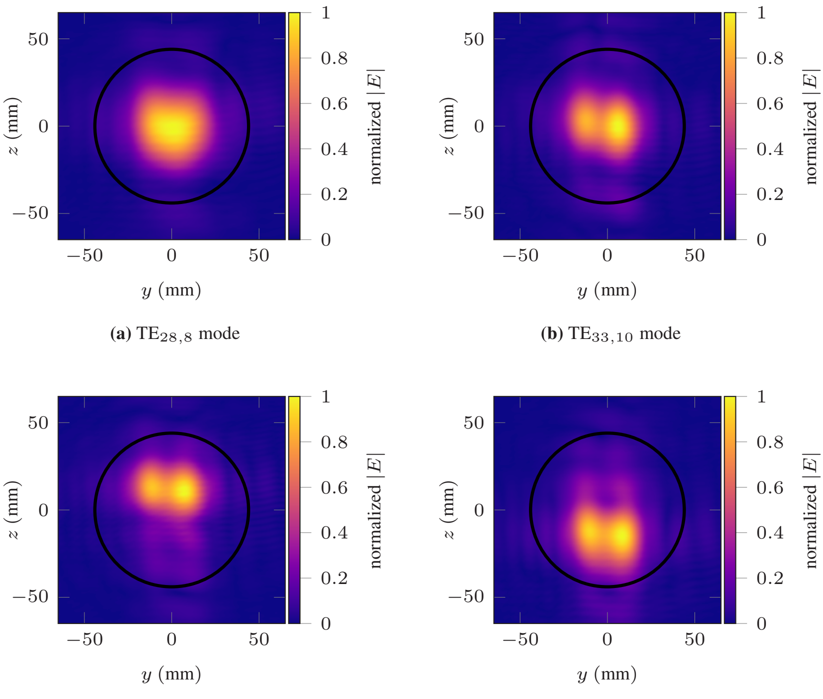

(a) $TE_{28,8}$ mode

(b) $TE_{33,10}$ mode

(c) $TE_{34,10}$ mode

(d) $TE_{35,10}$ mode

Figure 4.5: Calculated electric field distribution at the gyrotron window for different modes at the launcher entrance. The black ring represents the window copper cuff.

The calculated profile of the candidate modes differs significantly from an ideal Gaussian $TEM_{0,0}$ mode. For all candidate modes, the electric field is concentrated inside the gyrotron window. The calculated beam does not hit the window copper cuff, fulfilling the requirement.

Table 4.2: Gaussian mode content for each candidate mode and nominal $TE_{28,8}$ mode at the gyrotron window

		$TE_{28,8}$	$TE_{33,10}$	$TE_{34,10}$	$TE_{35,10}$
Gaussian mode content	(%)	98.23	91.39	89.74	90.05
y shift from center	(mm)	0.45	0.61	1.29	2.90
z shift from center	(mm)	0.44	1.09	11.14	13.76

The vector Gaussian Mode content is calculated by using the mode matching analysis. The electric field amplitude and phase values of the Gaussian $TEM_{0,0}$ mode is fitted to the electric field amplitude and phase values obtained by the calculations from *KarLESSS*. With the fitting calculations, the y- and z-shift from the center of the window are also obtained for the resulting $TEM_{0,0}$ mode. The calculated vector Gaussian mode content, y- and z-shift from the window center for each TE mode is shown in Table 4.2.

In Figure 4.6, the resulting electric field distribution at the beam tunnel exit is shown for the nominal $TE_{28,8}$ and the candidate modes. The electric fields are normalized to their maximum value for each TE mode. The black ring represents the beam duct tunnel wall. For all modes, the electric field is concentrated inside the tunnel, and the Gaussian-like beam exits the tunnel without hitting the tunnel border. As at the gyrotron window, the mm-wave beam of each candidate mode is not at the center of the tunnel. The first mirror in the beam duct [33] can correct this offset. Moreover, mode converting phase correcting mirrors with non-quadratic surface contour function [127], [128], which are placed in the matching optics unit in the beam duct, can further improve the quality of the mm-wave beam.

4.3.2 Optimum Guiding Center Radius

For each candidate mode, there exists a guiding center radius of the electron beam for which the interaction is optimal [65]. The guiding center radius at the cavity midsection is determined by the magnetic compression (as described with

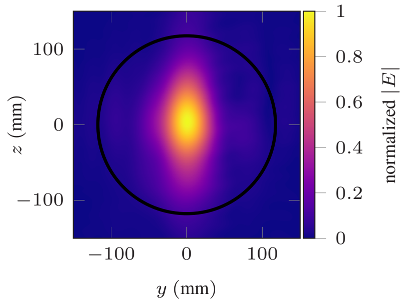

(a) $TE_{28,8}$ mode

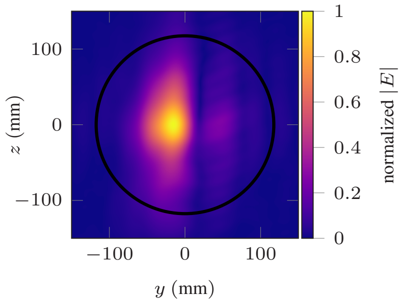

(b) $TE_{33,10}$ mode

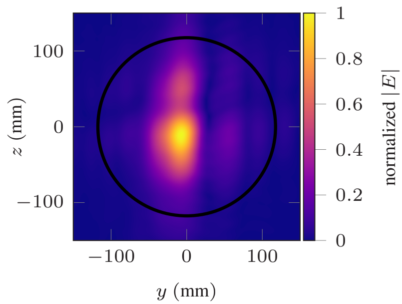

(c) $TE_{34,10}$ mode

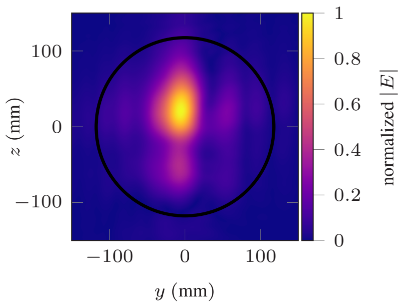

(d) $TE_{35,10}$ mode

Figure 4.6: Calculated electric field distribution at the beam duct tunnel exit for different excited TE modes at the launcher entrance. The black ring represents the tunnel wall.

Equation 2.12), which can be changed with the magnet coil currents. To find the optimum magnet coil currents, the optimum guiding center radius for each candidate mode is determined first.

The coupling between the electron beam and each candidate mode is calculated with Equation 2.26. In Figure 4.7, the normalized coupling is shown for different guiding center radii. The coupling factor is normalized to its maximum value for each candidate mode. The optimal guiding center radius is where the coupling factor is maximal and is calculated with Equation 2.27. In Table 4.3, the optimal guiding center radius is shown for each candidate mode.

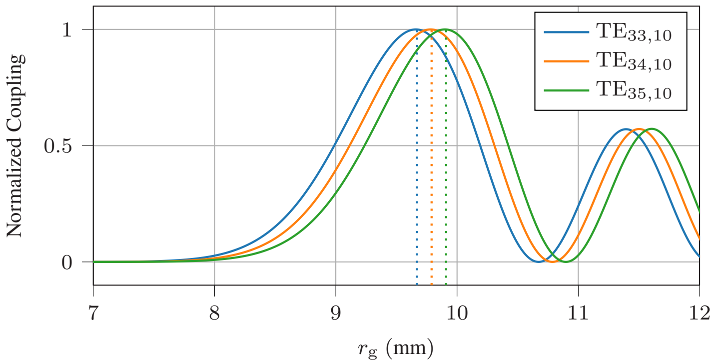

Figure 4.7: Coupling factor and optimal guiding center radius for each candidate mode

Table 4.3: Optimal guiding center radius for each candidate mode

	$TE_{33,10}$	$TE_{34,10}$	$TE_{35,10}$
$r_{g,opt}$ (mm)	9.67	9.79	9.91

4.3.3 Optimum Magnet Coil Currents

After the optimal guiding center radius is found, simulation of the MIG are conducted to obtain the electron beam parameters at the cavity. First, an operating point is defined for the electron gun simulations. The operating point serves as starting point for the simulations. As in [124], a valid starting point is an electron kinetic energy of 75 keV and a electron beam current of 40 A. Because the gyrotron shall operate for the CTS diagnostic with 10 ms pulses, the neutralization of the electron beam can be neglected.

A first estimation for the required magnetic field strength at the center of the cavity is calculated with Equation 2.3. The following assumptions are made:

- the TE modes are excited near their cutoff frequency [65]
- the required electron cyclotron frequency is 3 % lower than the excited frequency [129]

The resulting magnetic field strength for each candidate mode is shown in Table 4.4.

Table 4.4: Calculated optimal magnetic field strength at the cavity center B_{cav} for each candidate mode

	$\mathrm{TE}_{33,10}$	$\mathrm{TE}_{34,10}$	$\mathrm{TE}_{35,10}$
B_{cav} (T)	6.800	6.915	7.029

With these settings, the magnet coil currents are the only remaining free parameters that can be changed to obtain the desired electron beam parameters for each candidate mode. The HMC coil current I_{HMC} is fixed at 77 A, as required by the manufacturer *Cryomagnetics*. This leaves two parameters to sweep for finding the optimal electron beam parameters for each candidate mode:

- the main coil current I_{MC} of the LMC, UMC and CMC,
- the current I_{GTC} of the GTC.

The parameters of the electron beam at the middle of the cavity are calculated with *ESRAY*. The accelerating voltage between anode and cathode is set to 80 kV, the beam current to 40 A and the electron space charge neutralization to 0 %. The optimal values for the magnet coil currents are determined with the guiding center radius and the magnetic field at the center of the cavity for each candidate mode, which are shown in Figure 4.8.

The magnet coil currents I_{MC} and I_{GTC} for each candidate modes are chosen as follows. The mean guiding center radius does not change significantly for different I_{MC} values and mainly depends on I_{GTC}. Therefore, I_{GTC} is chosen to obtain the optimal guiding center radius, which is shown in Table 4.3 for each candidate mode. Then, I_{MC} is chosen to obtain the required calculated magnetic field strength at the cavity center (Table 4.4), because B_{cav} depends on I_{MC}.

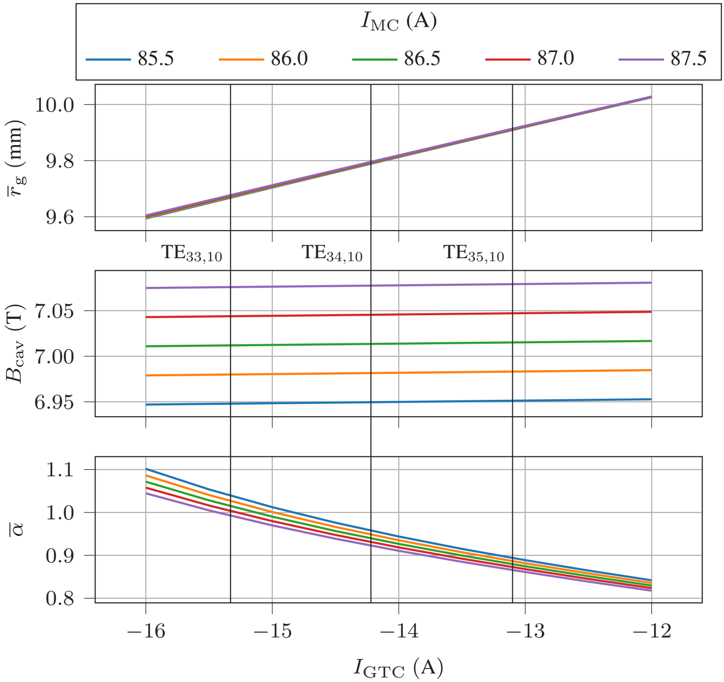

Figure 4.8: Mean electron beam guiding center radius, magnetic field strength, and mean pitch factor at the center of the cavity for different magnet coil currents

The pitch factor α is an important electron beam parameter for the interaction with the TE mode in the cavity. It determines the energy transfer from the electrons to the TE mode in the transverse plane. Overall, in Figure 4.8, the mean pitch factor is below 1.1, which is below the typical value of 1.1 to 1.3. In gyrotrons with diode-type MIG, the pitch factor cannot be changed independently, and the excitation of each candidate mode must be investigated for the resulting pitch factor value.

In Table 4.5, the optimal magnet coil currents and the resulting electron beam parameters at the center of the cavity are shown for each candidate mode. The guiding center radius and magnetic field strength coincide with their calculated optimal values from Table 4.4 and Table 4.3.

Table 4.5: Electron beam parameters at the cavity center from optimal magnet coil currents for each candidate mode

		$\mathrm{TE}_{33,10}$	$\mathrm{TE}_{34,10}$	$\mathrm{TE}_{35,10}$
I_{MC}	(A)	83.14	85.03	86.73
I_{GTC}	(A)	-15.33	-14.22	-13.10
I_{HMC}	(A)	77.00	77.00	77.00
B_{cav}	(T)	6.80	6.92	7.03
$\overline{r}_{\mathrm{g}}$	(mm)	9.66	9.79	9.91
Δr_{g}	(%)	1.60	1.58	1.52
$\overline{\alpha}$		1.11	0.97	0.88
$\Delta\alpha$	(%)	3.45	4.33	5.16
$\overline{\gamma}$		1.146	1.147	1.148
$\Delta\gamma$	(%)	0.023	0.023	0.027
$\overline{W}_{\mathrm{kin}}$	(keV)	74.63	75.10	75.40

4.3.4 Interaction Simulations

After the determination of the optimal operating points and the calculation of the electron beam parameters at the cavity, interaction simulations are conducted with *EURIDICE* to analyze the excitation of each candidate mode. The start-up scenario considers the increase of the accelerating voltage increases over time, and soft excitation of the TE modes.

For the start-up scenario, the electron beam parameters are calculated for different accelerating voltages. I_{MC} and I_{GTC} are kept constant as specified in Table 4.5 for each candidate mode. The electron beam parameters for the interaction simulations with *EURIDICE* are calculated in *ESRAY* for the corresponding accelerating voltages.

The interaction simulations with *EURIDICE* are carried out with 1300 electrons and with consideration of statistical variations of the electron beam parameters by including the spread values obtained from *ESRAY*. Furthermore, 42 possible competitive TE modes are included in the interaction simulations for each candidate mode. Modes are taken into account as competitors if their relative coupling with the electron beam is greater than 0.5 and their cut-off frequency is in the range between −5 % to 10 % of the candidate mode frequency.

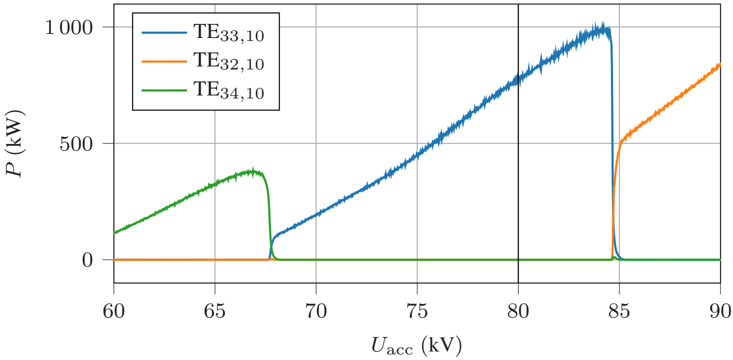

Figure 4.9: Multimode interaction simulation with *EURIDICE* at the calculated optimal operating point for the candidate $\mathrm{TE}_{33,10}$ mode

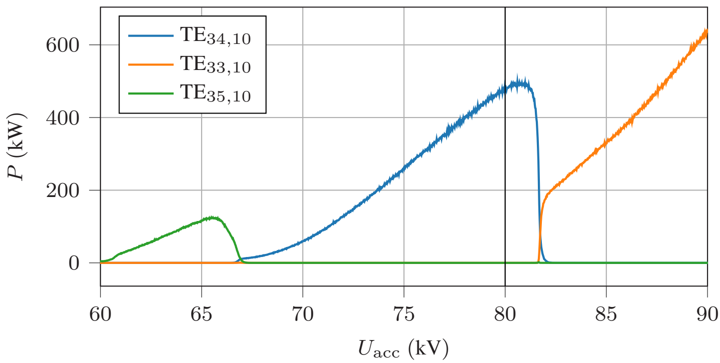

Figure 4.10: Multimode interaction simulation with *EURIDICE* at the calculated optimal operating point for the candidate $\mathrm{TE}_{34,10}$ mode

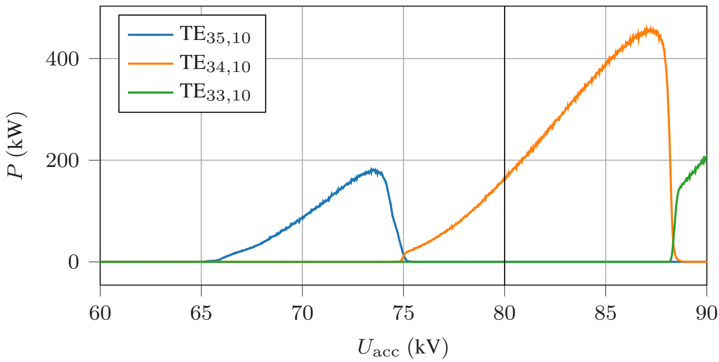

Figure 4.11: Multimode interaction simulation with *EURIDICE* at the calculated optimal operating point for the candidate $TE_{35,10}$ mode

In Figure 4.9, Figure 4.9 and Figure 4.9, the results of the simulations with *EURIDICE* are shown. For each candidate TE mode, the respective optimal operating point calculated in Section 4.3.3 is taken. The nominal accelerating voltage is 80 kV. In the interaction simulations, the $TE_{33,10}$ and $TE_{34,10}$ modes are successfully excited without any other competitive modes at the operating point. The $TE_{35,10}$ mode is not excited at the operating point from Table 4.5. Instead, the $TE_{34,10}$ mode is excited at 80 kV. A higher magnetic field is required to excite the $TE_{35,10}$ at 80 kV.

4.4 Gyrotron Operation for CTS Diagnostic

At W7-X, the new 7 T magnet system was delivered and installed for the TH1507 Maquette tube. Experiments are conducted to excite the $TE_{34,10}$ and $TE_{35,10}$ modes that were predicted in [124]. Additionally, the $TE_{33,10}$ mode is also excited during the experiments. The results and operating parameters obtained in Section 4.3 are used to find the excitation of the candidate TE modes.

During the experiments, it was not possible to excite the $\mathrm{TE}_{35,10}$ mode. Of all three candidate modes, the electron beam for the $\mathrm{TE}_{35,10}$ mode has the lowest pitch factor. Its excitation requires a higher beam current and higher magnetic field, which could not be achieved in the experiments. Specifically, the 7 T magnet is operated until its maximal rated current value for I_{MC}, resulting in the highest possible magnetic field for the $\mathrm{TE}_{35,10}$ mode.

4.4.1 Profile of the Gyrotron Output Beam

To determine if a candidate mode is excited, a target is placed at the exit of the tunnel leading into the beam duct. The location of the target is shown in Figure 4.4 at position (b). An infrared camera records the target surface temperature, which allows to determine the shape of the excited mm-wave beam.

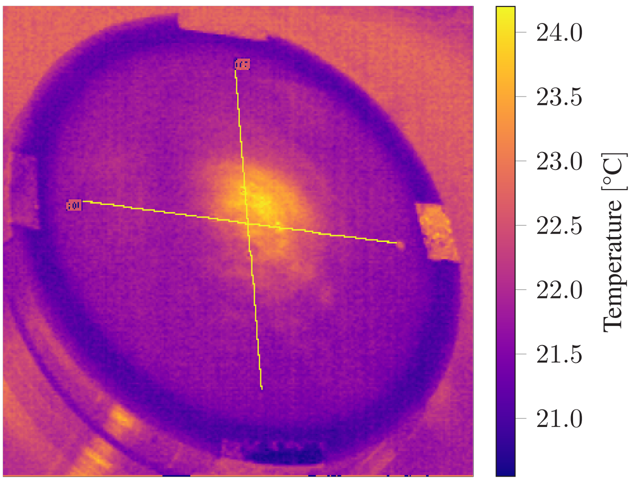

Figure 4.12: Shape of the gyrotron mm-wave output beam at the beam duct for the $\mathrm{TE}_{33,10}$

The operating parameters from Section 4.3.3 are used as starting point to excite the $TE_{33,10}$ and $TE_{34,10}$ modes. Short-pulses with a duration of 1 ms are conducted and the magnet coil currents are varied until the mm-wave beam is seen at the target.

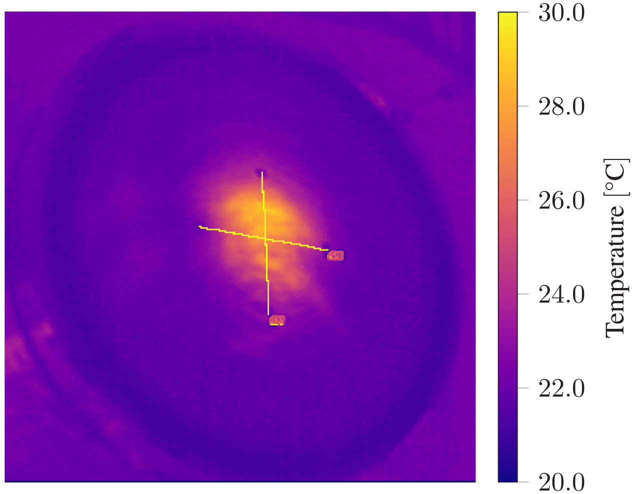

Figure 4.13: Shape of the gyrotron mm-wave output beam at the beam duct for the $TE_{34,10}$ mode

In Figure 4.12, the profile of the mm-wave beam at the exit of the beam duct tunnel is shown for the $TE_{33,10}$ mode. The mm-wave beam is concentrated in the middle of the tunnel, and does not hit the tunnel wall. The measured frequency of mm-wave beam is 171.04 GHz, which is consistent with the simulation results for the $TE_{33,10}$ mode.

In Figure 4.13, the profile of the gyrotron mm-wave beam at the exit of the beam duct tunnel is shown for the $TE_{34,10}$ mode. The mm-wave beam exits the tunnel and does not hit the tunnel wall. The measured frequency of mm-wave beam is 173.91 GHz.

4.4.2 Determination of the Optimum Operating Point

In Section 4.4.1, the $TE_{33,10}$ and $TE_{34,10}$ modes are successfully excited. Both mm-wave beams do not exit the tunnel through the center. The offset from the center is corrected by the first mirror in the beam duct [33]. For power measurements, the mm-wave beam is transmitted to the short pulse load in the beam duct. For the $TE_{33,10}$ and $TE_{34,10}$ modes, the operating point that obtains the maximum output power is determined. Experiments with pulse lengths of 10 ms are conducted.

Output Power of the $TE_{33,10}$ Mode

The optimum values for the magnet coil currents during the experiments are: $I_{\mathrm{MC}} = 84$ A and $I_{\mathrm{GTC}} = -14.75$ A. The beam current is set to 40 A for all pulses. The output power at the short-pulse load for different accelerating voltages during the experiments is shown in Figure 4.14 for the $TE_{33,10}$ mode. The highest output power is 550 kW, which is obtained with an accelerating voltage of 84 kV. With an accelerating voltage higher than 84.5 kV, the $TE_{33,10}$ mode could not no longer be excited.

With a frequency of 171.04 GHz, the reflection of the mm-wave beam at the gyrotron window is significantly high (11 %). The experiments with the $TE_{33,10}$ mode show that it is still possible to operate the gyrotron for pulse duration up to 10 ms.

Output Power of the $TE_{34,10}$ Mode

The optimal values for the magnet coil currents during the experiments are: $I_{\mathrm{MC}} = 86.3$ A and $I_{\mathrm{GTC}} = -14.0$ A. The beam current is 40 A for all pulses. The output power at the short-pulse load for different accelerating voltages during

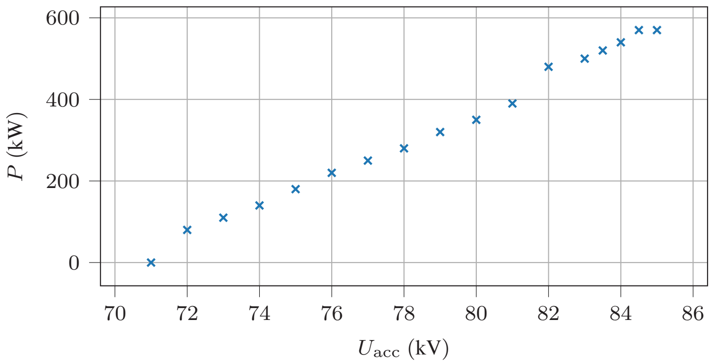

Figure 4.14: Measured output power of the operation with the $TE_{33,10}$ mode excitation at different accelerating voltages

the experiments is shown in Figure 4.15 for the $TE_{34,10}$ mode. The highest output power is 330 kW, which is obtained with an accelerating voltage of 82 kV. The $TE_{34,10}$ mode excitation is lost with an accelerating voltage higher than 83 kV.

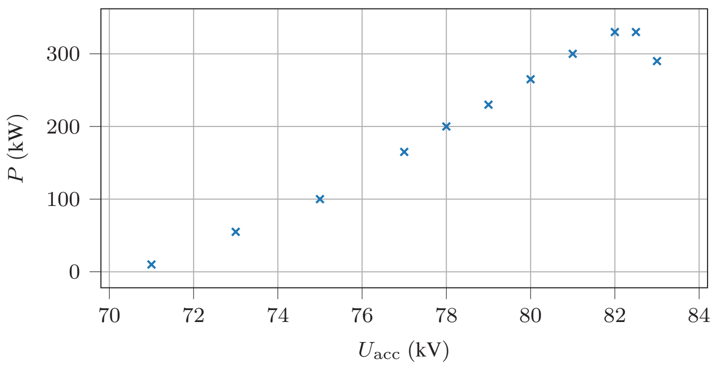

Figure 4.15: Measured output power of the operation with the $TE_{34,10}$ mode excitation at different accelerating voltages

4.5 Summary

The new 7 T magnetic system was successfully installed for the TH1507 Maquette gyrotron. Simulation results show that the candidate modes from [124] could be excited with the magnetic profile from the new 7 T magnet system. The new $TE_{33,10}$ candidate mode is also investigated.

Optimal operating points are theoretically investigated and the operating parameters for the experiments are determined. These theoretical optimal operating points serve as starting point for the experiments. The $TE_{33,10}$ and $TE_{34,10}$ mode are successfully excited during the experiments, while the $TE_{35,10}$ mode could not be excited. The obtained maximum output power is 550 kW at 171.04 GHz for the operation with $TE_{33,10}$ mode and 300 kW at 173.91 GHz for the operation with the $TE_{34,10}$ mode.

Although the excitation of the $TE_{33,10}$ mode achieved a higher output power than the $TE_{34,10}$ mode, the reflection at the gyrotron window is significantly higher. Moreover, the mm-wave beam needs to pass through another window to get into the W7-X plasma vessel. There, the reflection is also 11 %, resulting in even higher losses, and reflections into the beam duct. Therefore, the $TE_{34,10}$ mode is chosen as operating mode for the CTS diagnostic system. The reflection is with 1.176 % much lower, and the output power of 300 kW is sufficient for the CTS diagnostic.

5 Experiments with Frequency Stabilized MW-Class Gyrotrons

Experiments are conducted with the implemented PLL frequency stabilization system presented in Section 3.3 to investigate how accurate the gyrotron frequency can be stabilized. The setup is explained in Section 5.1. Experiments are conducted with the VGT8141A gyrotron from manufacturer *CPI* and TH1507 gyrotrons from manufacturer *THALES*. The experimental results for both Long-Pulse (LP) operation (> 1 s) and Short-Pulse (SP) operation (10 ms) are shown. For the long-pulse experiments, the frequency stabilization starts after the full frequency down shift at the beginning of the pulse. For the short-pulse experiments, the main objective is to determine if and for how long the frequency down shift can be counteracted.

5.1 Experimental Setup

The experimental setup for the gyrotron frequency stabilization is shown in Figure 5.1. The gyrotrons are located in the gyrotron hall (as shown in Figure 1.1), and their mm-wave beam is directed into either the LPL or SPL. A small part of the mm-wave beam is coupled out with a horn antenna. This mm-wave signal is transmitted through a waveguide system to the control room, where the frequency down conversion, the PLL frequency stabilization system and the measurement systems are located. After the frequency down conversion, the gyrotron IF signal goes into the PLL system and an oscilloscope. The PLL system outputs a control voltage to keep the gyrotron mm-wave beam at the set frequency. The value of the control voltage is transmitted digitally via fiber optics to the body power supply (Section 3.3.2).

At the body power supply, the digital control voltage is converted by an Analog-to-Digital Converter (ADC) into a voltage between 0 V to 5 V. For safety reasons, fixed upper and lower limits of the body voltage are set, preventing the PLL system from applying unsuitable body voltage during gyrotron operation. The maximal body voltage range with which the PLL system can modulate is 5 kV. For example, if the minimum body voltage is set to 22 kV and the maximum is set to 27 kV, a control voltage of 5 V results in a body voltage of 22 kV and a control voltage of 0 V results in a body voltage of 27 kV.

To measure the frequency of the gyrotron, two methods are used:

- Frequency Time Analyzer (FTA) that is a custom made system for IPP
- Capturing the IF signal in time domain with an oscilloscope

The FTA operates in the frequency range from 139.5 GHz to 141.5 GHz, and can not be used for the gyrotron CTS operation at 174 GHz. Internally, the FTA mixes the gyrotron signal down to a suitable IF band and further divides the frequency. Then, the FTA measures the period of the signal by counting the time between each rising zero crossing. The frequency accuracy is 152 kHz at 139.5 GHz and 305 kHz at 141.5 GHz. The output of the FTA is a voltage signal that is proportional to the gyrotron frequency. The FTA signal is continuously available during the gyrotron operation for all pulse lengths.

The second measurement system is an oscilloscope that captures the down converted gyrotron IF signal. The gyrotron IF signal is between 10 MHz to 100 MHz and is captured by the oscilloscope with a sampling rate of 250 MHz. Since the oscilloscope has only a maximal storage of twenty million samples, not more than 80 ms can be captured for each pulse. During the long-pulse experiments,

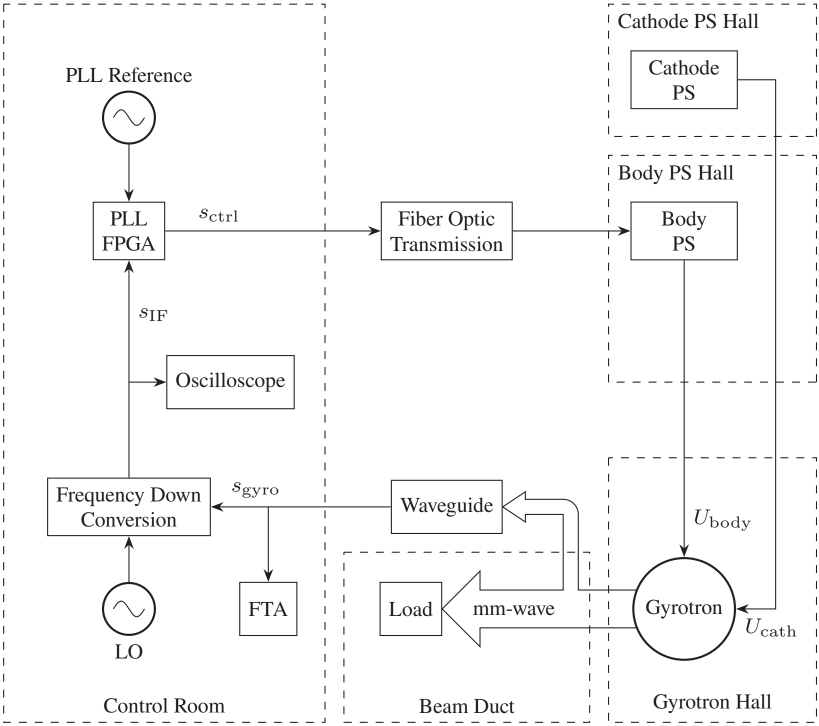

Figure 5.1: Experimental setup for the frequency stabilization experiments

the last 80 ms are captured. The obtained signal is digitally analyzed, and the gyrotron frequency spectrum is obtained with a Fast Fourier Transform (FFT) of the gyrotron IF signal.

The gyrotron operating parameters are also measured with the already existing measurement systems at W7-X. The following quantities are measured:

Cathode voltage The cathode voltage is measured to analyze the noise of the cathode power supply.

Body voltage The frequency control system modulates the body voltage to stabilize the gyrotron frequency. A measurement of the body voltage allows to see how well the signal of the frequency stabilization system are translated to the gyrotron body potential.

Output power The mm-wave output power over time is measured with a diode. A small part of the gyrotron mm-wave beam is coupled out in the beam duct and is transmitted to the measurement diode.

5.2 Experiments with VGT8141A Gyrotron

In this section, the LP and SP frequency stabilization experiments with the VGT8141A gyrotron from manufacturer *CPI* are presented. For each frequency stabilization experiment, a nominal gyrotron operating point is chosen, which includes fixed values for the static magnetic field, the cathode voltage and the beam current. The behavior of the PLL system is analyzed in the long-pulse experiments, and the gyrotron frequency spectrum using the PLL is determined. Furthermore, proof-of-principle experiments are conducted for the CTS diagnostic.

5.2.1 Long-Pulse Frequency Stabilization

Counteracting the frequency down shift at the start of the gyrotron pulse requires an accelerating voltage change larger than 10 kV, which would result in loss of excitation of the operating mode. Therefore, the frequency stabilization system is enabled after the frequency down shift, when the frequency variation of the free-running gyrotron is only in the MHz range. Frequency stabilization experiments are conducted with a pulse duration of 5 s and 60 s. The gyrotron frequency spectrum is analyzed. The control parameters are changed, and the stability of the

PLL system is evaluated. Furthermore, the gyrotron set frequency is changed and the influence of the set frequency on the output power is investigated. Finally, the gyrotron set frequency is changed during a pulse with a triangular modulation.

Stabilization to a Single Frequency

In Table 5.1, the operating parameters for the experiment are shown. A free-running gyrotron operation is conducted to compare it to a frequency stabilized gyrotron operation, and the body PS is set to a constant output voltage of 21 kV. In Figure 5.2, the body voltage, gyrotron frequency and output power over time are shown for the free-running operation. After 1 s, the frequency down shift from start-up has finished and the excited frequency settles at around 139.976 GHz. However, still smaller frequency variations in the MHz range are present.

Table 5.1: Operating parameters for frequency stabilization

Body voltage	16-21	kV
Cathode voltage	60	kV
Cathode current	40	A
Main coil current	86	A
Gun coil current	1.6	A

For the operation using the frequency stabilization, the body voltage is varied from 16 kV up to 21 kV. The results for the frequency stabilized operation are shown in Figure 5.2.

From the start of the pulse until 1 s, the body voltage is set to 19.75 kV. After 500 ms, the gyrotron frequency settles at 139.99 GHz, which is higher compared to the frequency obtained with a body voltage of 21 kV.

After 1 s, the PLL system is switched on, and the gyrotron is stabilized to a set frequency of 139.98 MHz. The PLL system detects that the actual frequency is higher than the set frequency, and immediately increases the body voltage to lower

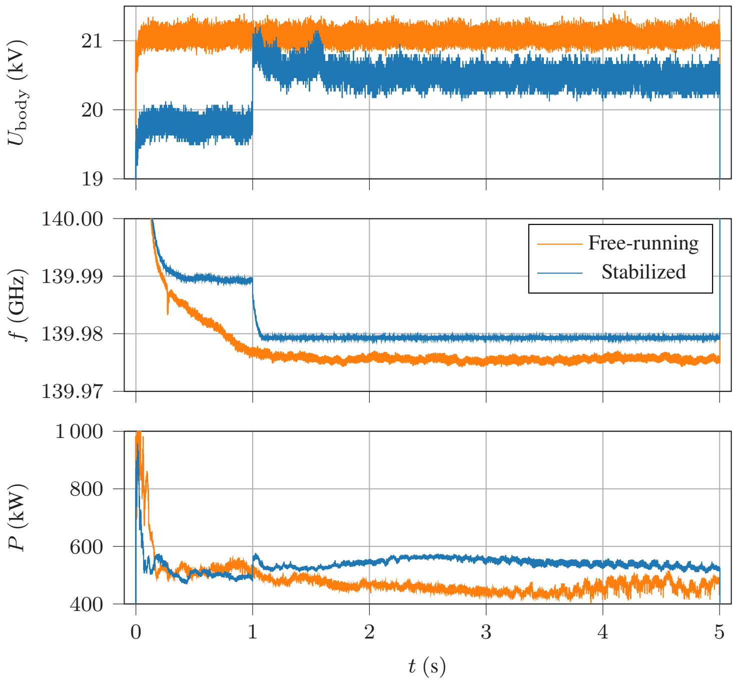

Figure 5.2: Free-running and frequency stabilized operation of the VGT8141A gyrotron. The set frequency for the frequency stabilization is 139.98 MHz

the gyrotron frequency. For a short time, the body voltage is a at the maximal value of 21 kV. However, the gyrotron frequency does not reach the set frequency immediately. Instead, it jumps at 1 s to 139.985 MHz and then exponentially reaches the set frequency of 139.98 MHz. The maximal body voltage of 21 kV is not sufficient for the gyrotron frequency to immediately reach the set frequency. However, due to the increase in body voltage, the output power also increases at 1 s. This increase is sufficient enough to heat the cavity, resulting in a frequency down shift as at the beginning of the pulse (as described in Section 3.1.5). Thus, the frequency dependence on the output power increases the capture range of the gyrotron PLL system.

When the gyrotron frequency reaches the set frequency, the PLL system starts decreasing the body voltage to prevent a further shift of the gyrotron frequency. After 1.1 ms, the gyrotron frequency remains stable at the set frequency, and compared to the free-running frequency, the stabilized frequency has no shifts in the MHz range.

When the frequency is stable, changes of the body voltage relate to frequency changes that would have happened with the free-running gyrotron frequency. For example, at 1.5 s, the body voltage increases, indicating that the gyrotron frequency would also have increased if the PLL would be disabled. Thus, with observing the body voltage (or control signal from the PLL), a conclusion of the gyrotron frequency behavior can be drawn, which could be used in more advanced control systems. Particularly, the PLL system could be used in combination with the automated mode recovery system described in [130], and the identification of a precursor signal before mode loss could be further investigated.

Although the PLL system controls the accelerating voltage, large power fluctuations do not occur during the stabilized operation. Only if the PLL system is enabled at 1 s, the jump of the body voltage results in a jump of the power. Afterwards, the power fluctuations are similar to the ones during free-running operation, because the average value of the body voltage does not change significantly. However, changing the set frequency results in a different average body voltage and output power.

Analysis of the Stabilized Frequency Spectrum

In Figure 5.3, the spectrum of free-running and frequency stabilized VGT8141A gyrotron is shown between −1 MHz to 1 MHz and −70 kHz to 70 kHz around the gyrotron set frequency. The spectrum is obtained with a Fourier transform of the gyrotron IF signal during the last 38 ms of the 5 s pulses from Figure 5.2.

The spectrum for the free-running operation is centered at 139.976 GHz, while the spectrum of the frequency stabilized operation is centered at 139.980 GHz. The magnitude of the frequency-stabilized spectrum is normalized to its highest

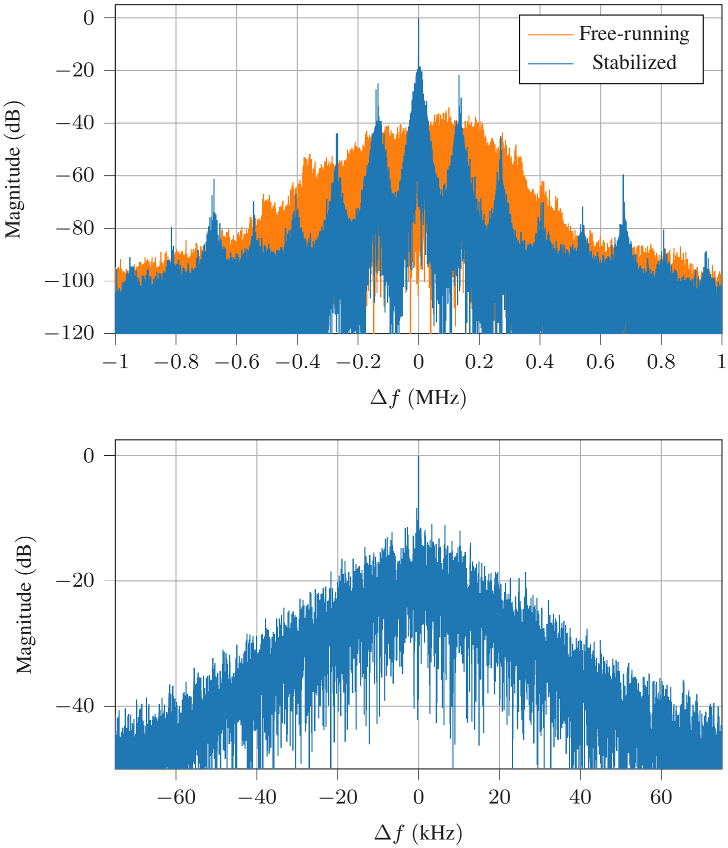

Figure 5.3: Spectrum of the free-running and frequency stabilized VGT8141A gyrotron. The free-running spectrum is centered at 139.976 GHz. The gyrotron is stabilized to a frequency of 139.980 GHz, where the main peak in the spectrum is located. A detailed frequency stabilized spectrum around the main peak from −70 kHz to 70 kHz is also shown.

frequency peak. To compare the free-running spectrum with the frequency stabilized spectrum, the free-running spectrum is normalized such that it has the same noise floor as the frequency stabilized spectrum.

For the free-running operation, not a single clear main peak is visible at a specific frequency in the spectrum, and the frequencies are spread over a band of frequencies with a full -20 dB bandwidth of 1 MHz. Since the spectrum is only calculated during the last 38 ms of the pulse shown in Figure 5.2, the spectrum is narrower than it would be over the whole pulse. Not accounting for the frequency down shift at the beginning of the pulse, the frequency for the free-running operation has larger frequency variations than in the captured 38 ms time period (frequency over time curve in Figure 5.2). Thus, the frequency spectrum over a time period of 1 s would be even broader than the one shown in Figure 5.3.

In comparison, a distinct main peak at exactly the set frequency of 139.980 GHz is present for the frequency stabilized operation. The width of the main peak is as narrow as one sample and has therefore the frequency resolution of the FFT, which is $\frac{1}{38\,\mathrm{ms}} = 26.3\,\mathrm{Hz}$. The next higher peak is 430 Hz from the main peak with a magnitude 10 dB lower than the main peak. More broadening noise arises 15 dB lower than the main peak. A full -20 dB bandwidth of below 100 kHz is achieved.

Furthermore, clear sidebands arise in the stabilized spectrum. These sidebands arise for different operating parameters and for different frequency stabilization parameters. Thus, these sidebands are inherent to the system. The analysis of the power supply noise in Section 3.2.5 shows that the same frequencies are present in the cathode power supply noise.

With the gyrotron IF signal, a frequency over time curve is calculated by taking the time between the positive zero crossings of the IF signal. In Figure 5.4, the spectrum of the resulting frequency over time curve is shown. Since the spectrum is obtained from the frequency over time curve of the gyrotron IF signal, the spectrum shows the frequency modulation of the gyrotron. In Figure 5.4, harmonics of 3.3 kHz are present as well as a high peak at 135 kHz. The spectrum is similar to the spectrum form the cathode power supply noise (see Figure 3.14), which also has harmonics of 3.3 kHz and a high peak at 135 kHz.

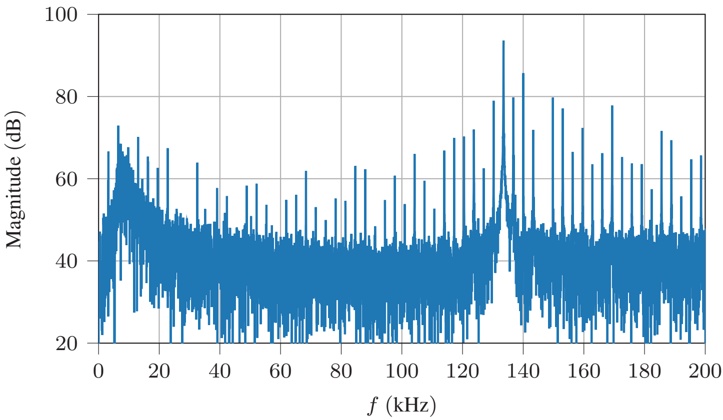

Figure 5.4: Spectrum of the f-vs-t gyrotron signal

The comparison shows that the PLL system is able to counteract the long-term frequency shifts. The remaining sidebands at 3.3 MHz and 135 MHz in the frequency spectrum, attributed to the cathode power supply fluctuations, cannot be compensated as the control bandwidth with the body PS is too low. To further improve the frequency stability of the gyrotron, the cathode PS noise must be reduced or the PLL control bandwidth increased.

Stability Analysis of Control Loop

The PLL control loop is stable with the control parameters $f_K = 16\,\text{kHz}$ and $f_\text{I} = 4\,\text{kHz}$ during the experiments. To further improve the stabilized gyrotron spectrum, the control loop requires to be faster, resulting in a higher control loop parameter f_K (see Section 2.2.1). However, with the body power supply dynamics, $f_K = 16\,\text{kHz}$ is already at the upper limit and further increasing f_K it results in unstable operation.

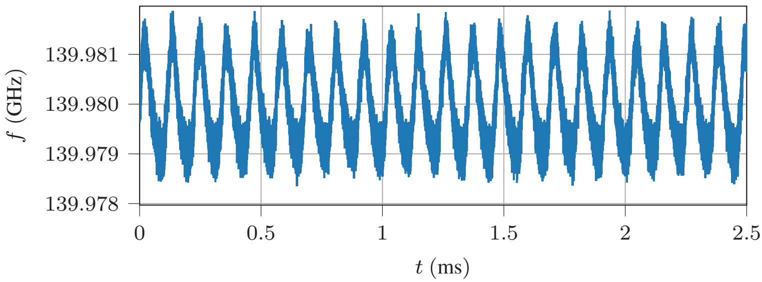

Figure 5.5: Gyrotron frequency with PLL control parameters $f_K = 21$ kHz and $f_\mathrm{I} = 5$ kHz resulting in unstable operation

In Figure 5.5, the frequency over time for 2.5 ms of a pulse is shown. The control parameters are $f_K = 21$ kHz and $f_\mathrm{I} = 5$ kHz. Oscillations of the gyrotron frequency occur and the PLL operation is unstable. The gyrotron frequency oscillations have a depth of 3 MHz and a frequency of 8.7 kHz.

Operation with Pulse Length of 60 s

To demonstrate that the PLL system stabilizes the gyrotron frequency also for longer pulses, experiments are conducted with a pulse duration of 60 s. In Figure 5.6, the body voltage, frequency and output power VGT8141A gyrotron (free-running and frequency stabilized) is shown for 60 s. For the free-running operation, the body voltage is constant at 20.8 kV. This results with a cathode voltage of 60 kV in an accelerating voltage of 80.8 kV.

During the free-running operation, the gyrotron frequency settles at 139.965 GHz after the frequency down shift. The output power increases from 650 kW at 5 s to 700 kW at 20 s, where it remains until the end of the pulse. The change in output power results in a change of the frequency due to cavity expansion. During the entire pulse, frequency variations in the MHz range are present.

For the operation with the PLL system, the gyrotron frequency is stabilized to 139.975 GHz after 1 s. At 1 s, the PLL system decreases the body voltage to pull the excited frequency from 139.969 GHz to the set frequency of 139.975 GHz.

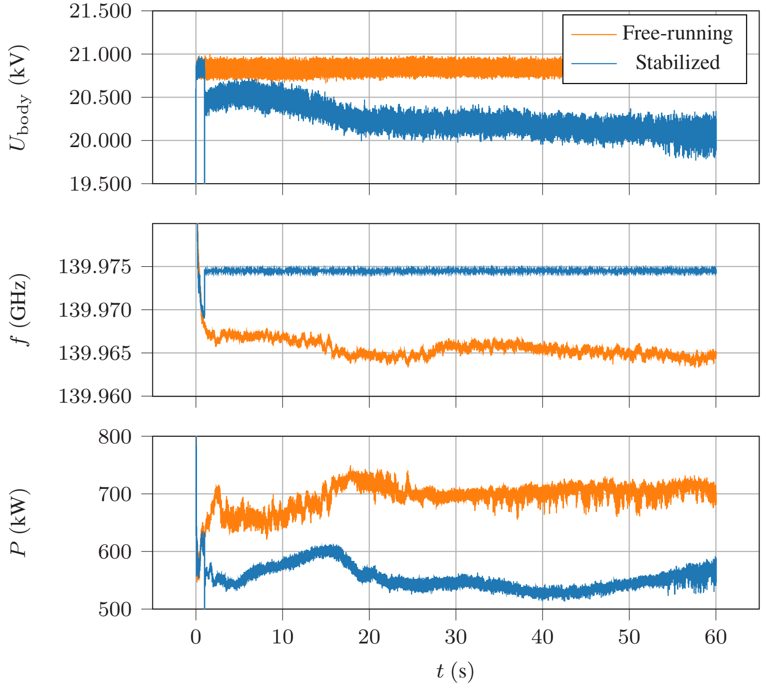

Figure 5.6: Body voltage, frequency and power of the free-running and frequency stabilized VGT8141A gyrotron for a 60 s pulse

After the excited frequency has reached the set frequency, it is stable until the end of the pulse (as with 5 s pulse in Figure 5.2). Compared to the free-running operation, the PLL system is a significant improvement of the gyrotron frequency during the entire 60 s pulse is achieved. The spectrum of the frequency stabilized gyrotron at the end of the pulse is similar to the one in Figure 5.3, and the distinct main peak at the set frequency is present. The sidebands at 3.3 kHz and 135 kHz are also present.

The change in accelerating voltage for the frequency stabilization results in a different output power than in the free-running operation. After 1 s, the body voltage is set to 20.5 kV, which results in an output power of 550 kW (150 kW less than with the free-running operation with 20.8 kV). After 10 s, the body voltage changes further to 20.2 kV to counteract the down shift of the free-running frequency. The lower output results from the choice of the set frequency for which a lower accelerating voltage than in the free-running operation is required.

Change of the Set Frequency

Experiments are conducted to determine the frequency range in which the gyrotron frequency can be stabilized. The PLL system only changes the accelerating voltage, while the static magnetic field in the cavity remains the same for each pulse. Therefore, for the stationary case, changing the set frequency changes the average accelerating voltage and output power.

In Figure 5.7, the gyrotron accelerating voltage, frequency and output power over time are shown for different set frequency values. The pulse duration is 5 s and the same operating parameters from Table 5.1 are used. The set frequency is changed from 139.96 GHz to 140.01 GHz. The average body voltage changes correspondingly, from 22.5 kV at 139.96 GHz to 19 kV at 140.01 GHz. The output power also varies with the change of the accelerating voltage; however, the changes are not as expected. The average output power decreases with increasing accelerating voltage, resulting in a reduction of the efficiency. Only at the lowest set frequency and at the highest accelerating voltage, the output power is at its highest (700 kW). The experiments show the importance of finding an optimal operating point. The same effect is observed in Figure 5.8, when the set frequency is modulated during a pulse.

Although the observed output power does not change as expected, the experiments show the dependence of the output power on the set frequency for PLL systems controlling the accelerating voltage. Setting the gyrotron to a specific set frequency also fixes the output power. However, this effect can be mitigated by changing other operating parameters that change the output power, such as the beam current or the static magnetic field (Section 3.1.3).

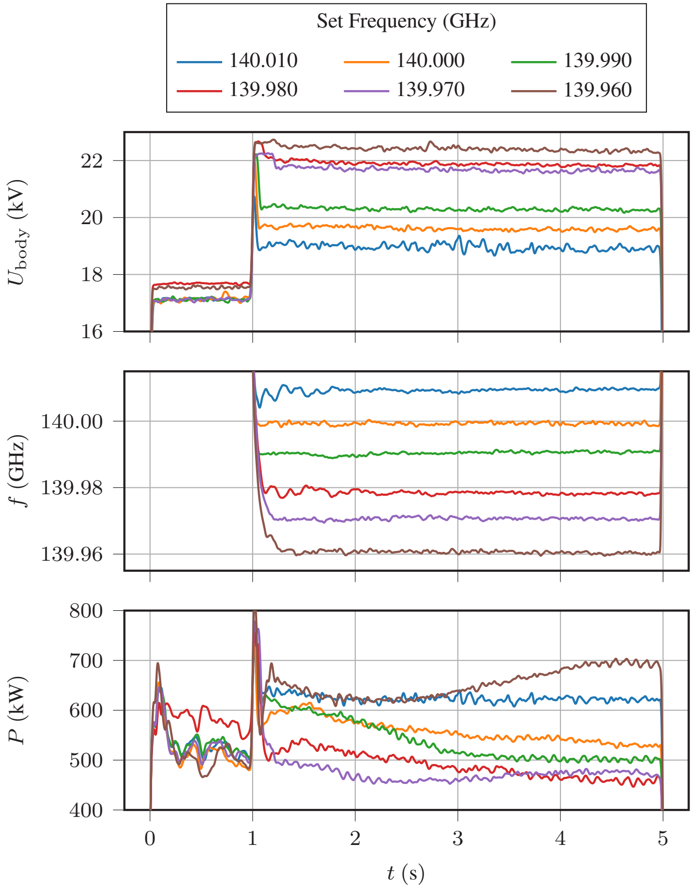

Figure 5.7: Frequency stabilization of the VGT8141A gyrotron with different set frequencies

Triangular Frequency Modulation

With the frequency stabilization system it is not only possible to stabilize the gyrotron frequency to a single set frequency, but also to precisely modulate the gyrotron frequency. This is done with modulating the PLL reference frequency.

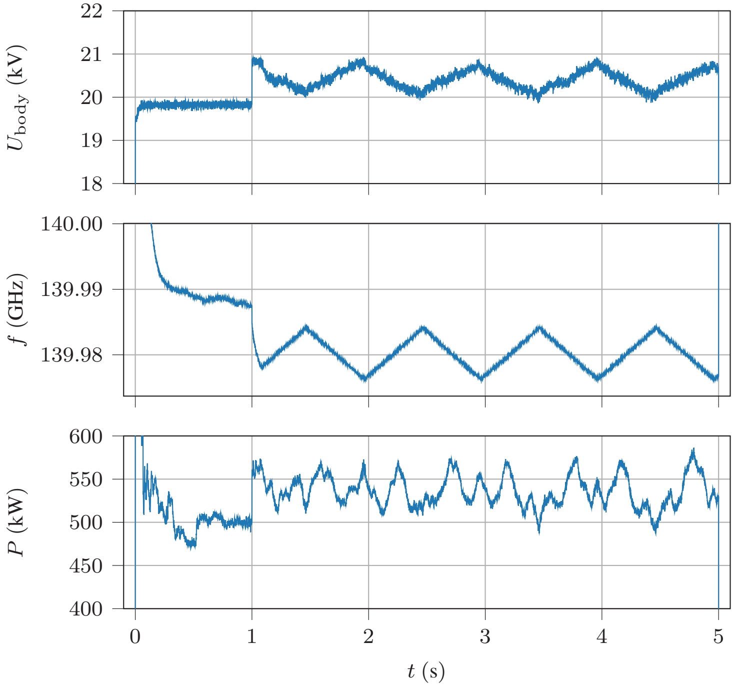

Figure 5.8: Triangular frequency modulation of the VGT8141A gyrotron

In Figure 5.8, the triangular frequency modulation of the VGT8141A gyrotron is shown. The PLL reference frequency is triangular frequency modulated with a modulation frequency of 1 Hz. The modulation depth of the gyrotron frequency is 8 MHz.

After 1 s, the gyrotron PLL is enabled and the gyrotron frequency is locked onto the reference frequency. The gyrotron frequency follows exactly a triangular shape. The body voltage is correspondingly controlled and is also a triangular. Because an increase in body voltage results in a decrease in frequency, the body voltage curve is the inverse of the frequency. The triangular shape of the body voltage curve is also distorted to counteract unwanted frequency changes during operation.

Under ideal conditions, the output power increases with the body voltage (higher accelerating voltage). However, the output power in Figure 5.8 does not follow the triangular modulation. For example, at 2.9 s and 3.9 s, the body voltage has reached its highest point (20.9 kV), but the output power is not at its highest point. Instead, the highest output power is reached at 2.7 s and 3.7 s, where the body voltage has 20.4 kV. Parasitic effects inside the gyrotron lead to a less favorable operating condition such that the output power deteriorates. This is also observed in Figure 5.7, where the set frequency is changed for different pulses. Overall, the average output power is 530 kW.

5.2.2 Short-Pulse Frequency Stabilization

After the successful frequency stabilization for long-pulse operation, short-pulse stabilization experiments are conducted with the VGT8141A gyrotron. The successful short-pulse frequency stabilization is an essential requirement for the CTS diagnostic. Although the TH1507 Maquette gyrotron at 174 GHz is used for the CTS diagnostic, proof-of-principle experiments are made at 140 GHz with the VGT8141A gyrotron. The main challenge is to counteract the frequency down shift for which the frequency stabilization control system needs to react fast enough. Furthermore, it is determined how fast the gyrotron frequency can be locked onto the set frequency.

Frequency Stabilization of Pulses with 10 ms Duration

The stabilization of the frequency down shift due to cavity heating and electron beam neutralization is analyzed with the SP experiments. The gyrotron pulses have a duration of 10 ms and the frequency stabilization is enabled immediately at the beginning of the pulse. The free-running gyrotron frequency is determined directly at the start of the pulse for the given operation point. For a fast frequency stabilization at the start of a pulse, the set frequency for the PLL is chosen close to the frequency excited immediately at the beginning of the pulse.

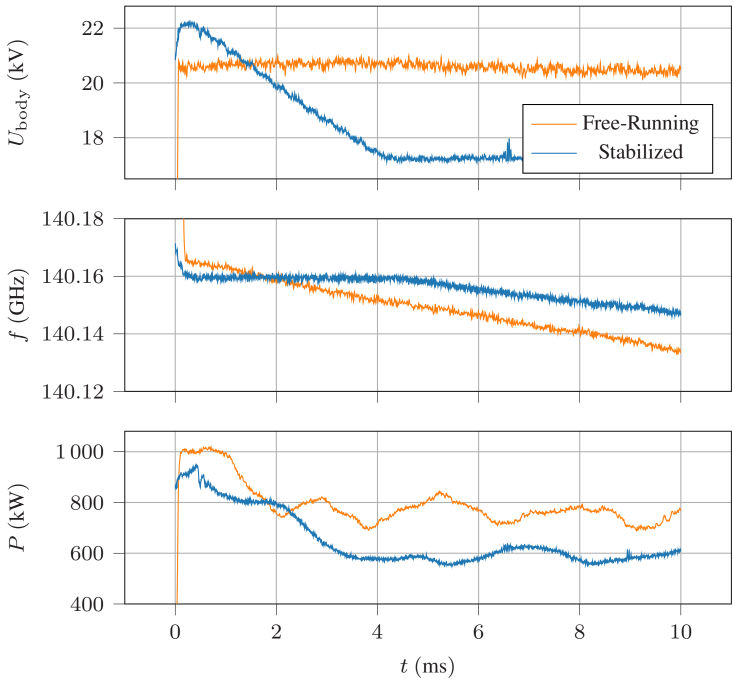

Figure 5.9: Body voltage, frequency and power of the free-running and frequency stabilized VGT8141A gyrotron for 10 ms

In Figure 5.9, the body voltage, frequency and power of the free-running and frequency stabilized VGT8141A gyrotron is shown for 10 ms. The body voltage for the free-running operation has a constant value of 20.5 kV and the gyrotron frequency starts at 140.165 GHz. For the frequency stabilized operation, a set frequency of 140.16 GHz is chosen.

At the start of the pulse, the PLL system measures that the excited frequency is higher than the set frequency, and increases the body voltage to lower the excited frequency until it reaches the set frequency (at 0.5 ms). Afterwards, the excited frequency would still decrease because of the cavity expansion and electron beam neutralization. However, the frequency stabilization system counteracts the frequency down shift by lowering the body voltage. The exited frequency is stabilized until 4 ms. Then, the body voltage has reached its lower limit of 17 kV and the frequency stabilization system can no longer counteract the frequency down shift. Thus, the duration of the frequency stabilization depends on the limits of the body voltage.

In Figure 5.9, the frequency is stabilized for 3.5 ms. Compared to the free-running operation, a frequency down shift of 15 MHz is counteracted with the PLL system.

The time at which the frequency is stabilized depends on:

- the excited frequency at the beginning of the pulse
- the set frequency
- how fast the frequency down shifts due to cavity expansion and electron beam neutralization

The set frequency needs to be determined correspondingly to achieve a stable excited frequency directly at the beginning of the pulse.

Because the body voltage is decreased, the output power also decreases compared to the free-running operation. However, the output power remains above 600 kW when the exited frequency is stable. Since a stable frequency is more important for the CTS diagnostic than higher output power, the obtained output power with the PLL system is sufficient. Additionally, power variations are not significant for the CTS diagnostic, because the final CTS spectrum is averaged over multiple pulses.

To counteract the frequency down shift for a longer duration, the body voltage needs to decrease further. This would bring the gyrotron out of its nominal operating point, less output would be achieved, and even loss of the nominal TE mode excitation would occur.

Frequency Stabilization of Multiple Consecutive Short-Pulses

After the successful stabilization of a single short-pulse, the scenario for the CTS diagnostic is repeated for multiple pulses. For the CTS, the probing beam gyrotron shall emit multiple short-pulses into the plasma. In the following experiments, the frequency stabilization for multiple short-pulses is analyzed. For short-pulses, the main challenge for the frequency stabilization system is to determine the excited gyrotron frequency at the start of the pulse. The cavity heats up due to losses during each pulse. Depending on the pulse repetition period, the cavity has not enough time to fully cool down to its initial state when the next pulse starts. Thus, the cavity temperature at the start of each pulse increases over time, resulting in an decrease of the excited frequency at the start of the pulse. At some point in time, a thermal equilibrium is reached and the cavity has the same temperature at the start of each pulse.

For the frequency stabilized operation, the same set frequency is chosen for all pulses. By choosing the frequency stabilization close to the thermal equilibrium frequency, the gyrotron stabilized correctly for almost all pulses except the first ones. Since the first pulses have a higher starting frequency, it takes longer until the excited frequency reaches the set frequency. Thus, for the first pulses, the frequency is not stabilized directly at the start of the pulse, but later it is.

In Figure 5.10, the body voltage, free-running frequency and output power for four consecutive short-pulses is shown. The body voltage is constant with 21 kV, resulting in an accelerating voltage of 81 kV. The pulses have a duration of 10 ms and are repeated every 50 ms, which corresponds to a duty cycle of 20 %. In Figure 5.10, the free-running frequency is lower for each consecutive pulse. For the first pulse, the free-running frequency starts at 140.160 GHz, for the second at 140.150 GHz, for the third at 140.140 GHz and for the fourth at 140.137 GHz. While for the first three pulses, the frequency at the start of the pulse is 10 MHz lower than the pulse before, the change of the fourth pulse is with 3 MHz already much lower. As with the frequency stabilization of a single short-pulse (see Figure 5.9), the duration of the frequency stabilization depends on the limits of the body voltage.

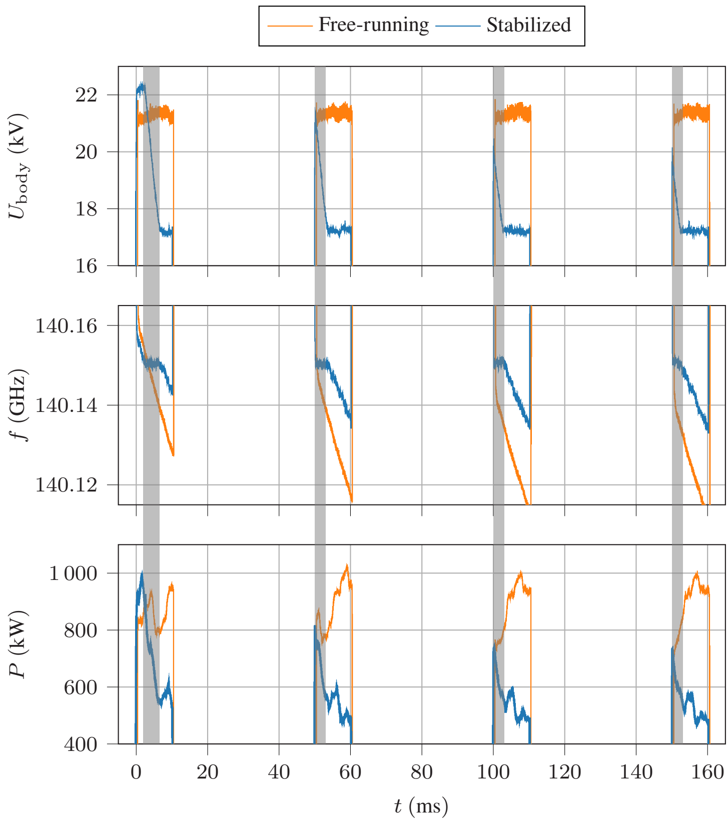

Figure 5.10: Body voltage, frequency and power of the frequency stabilized VGT8141A gyrotron for multiple short-pulses. The gyrotron is stabilized to a frequency of 140.151 GHz and the gray areas indicate when the gyrotron is frequency stabilized.

The experiments show that after four consecutive pulses, the cavity has reached its thermal equilibrium, and the frequency at the start of the pulse does not change significantly. The PLL system successfully stabilizes the gyrotron frequency during the first 3 ms of each consecutive pulse. Thus, the PLL system can be used for the CTS diagnostics.

5.3 Experiments with TH1507 Gyrotron

After the successful frequency stabilization experiments with the VGT8141A gyrotron, the PLL system is used with the TH1507 gyrotrons. During the free-running operation of the TH1507 gyrotrons, sudden frequency jumps are observed in [49], [131]. These sudden frequency jumps are analyzed, because their behavior disturbs the frequency stabilization with the PLL system. The main challenge is to avoid the frequency jumps and to have a stable gyrotron frequency during the whole pulse. In addition, short-pulse experiments at 174 GHz are conducted that are relevant for the CTS diagnostic.

5.3.1 Frequency Jumps of the TH1507 gyrotron

The frequency jumps in the TH1507 gyrotron were already described in [49], [131]. These frequency jumps are also observed in all nine TH1507 gyrotrons at W7-X. In Figure 5.11, the frequency jumps are shown for the gyrotrons TH1507 SN7i (A1) and TH1507 SN1 (C1). The labeling of the gyrotrons is explained in Section 1.2.

During the frequency down shift at the start of the pulse, the frequency does not shift down continuously, but jumps down. After the frequency down shift (0.8 s), the frequency jumps up and down. These frequency jumps occur until the end of the pulse, and different jump heights (ranging from 1 MHz to 10 MHz) are observed. Furthermore, the frequency shifts up during the first 5 s, which is most prominent for the C1 gyrotron in Figure 5.11. After the frequency down shift at start-up, the C1 gyrotron frequency settles at 139.950 GHz. The gyrotron frequency jumps up and down around 139.950 GHz until 3 s. Then, the frequency jumps from 139.950 GHz to 139.980 GHz in multiple steps, which is a frequency change of 50 MHz. The frequency of the A1 gyrotron changes by 10 MHz from 1 s to 5 s. In comparison, the frequency of the VGT8141A gyrotron changes less than 5 MHz after 1 s.

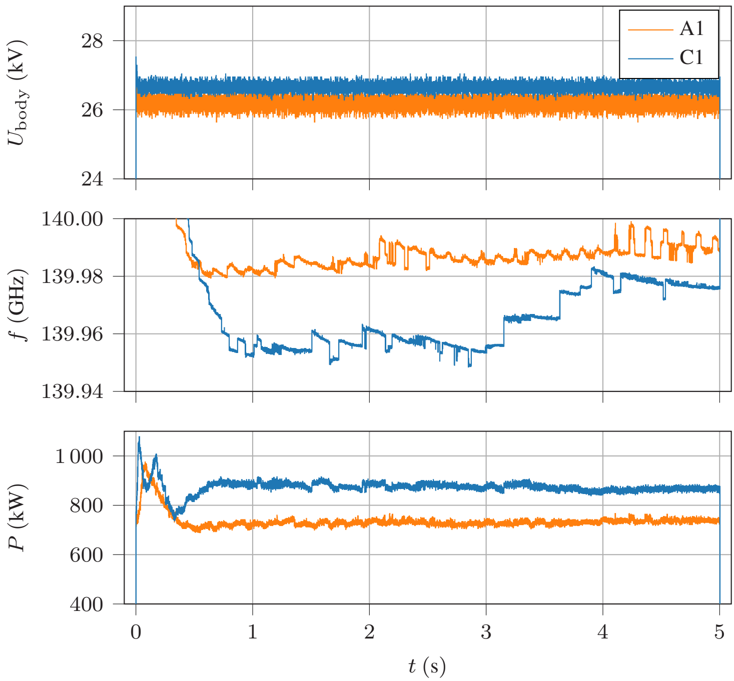

Figure 5.11: Frequency jumps of TH1507 SN7i (A1) and TH1507 SN1 (C1) gyrotrons for a 5 s pulse

The frequency jumps also occur during the 174 GHz operation of the TH1507 Maquette (B1) gyrotron. In Figure 5.12, the frequency over time of the gyrotron is shown for the first 10 ms. The gyrotron frequency changes from 173.934 GHz to 173.912 GHz, resulting in a frequency change of 22 MHz during 10 ms. The frequency down shift is not continuous and distinct frequency jumps appear at 0.2 ms, 3.8 ms, 5.0 ms and 6.5 ms. The frequency jumps have a height of 3 MHz.

A detailed look of a single frequency jump is shown in Figure 5.12 (a). The frequency jump happens on a fast time scale, in the range of µs. In Figure 5.12 (b), multiple jumps occur consecutively. The jump period is 7.399 µs, which results in a frequency of 135 kHz. The frequency jumps do not appear regularly and some jump periods are missed. The jump period coincides with the 135 kHz cathode power supply noise. However, in the cathode power supply noise, such sudden jumps in voltage are not observed. The frequency variations due to the 135 kHz cathode PS noise are shown in Figure 5.12 (a) (before and after the jump). These frequency variations are below 1 MHz, which is much smaller compared to the 3 MHz jumps. For a direct causality, the cathode voltage requires to have distinct jumps in the µs regime, which is not observed. Nevertheless, the jump repetition in Figure 5.12 (b) is an indication that the cathode power supply noise indirectly triggers the frequency jumps.

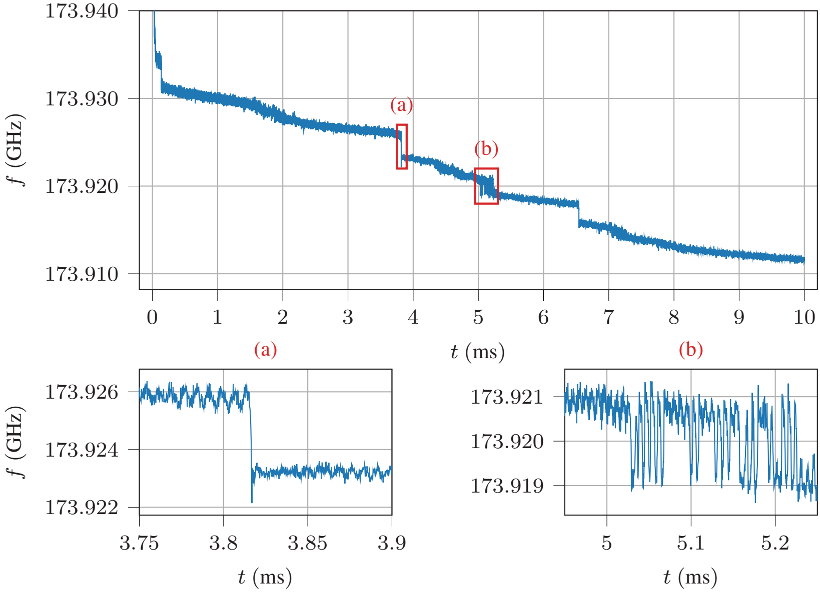

Figure 5.12: Frequency jumps at 174 GHz of the TH1507 Maquette gyrotron (B1) during the first 10 ms of a pulse. (a) and (b) show the frequency jumps more detailed.

5.3.2 Short-Pulse Experiments at 174 GHz

The new 7 T magnet allows the gyrotron operation at 174 GHz (Chapter 4). The operation with the PLL system at 174 GHz is similar to 140 GHz operation. Only the LO frequency of the mixer needs to be changed for the frequency stabilized operation at 174 GHz.

In Figure 5.13, the frequency stabilization of a 10 ms pulse is shown and compared to the free-running operation. The operating parameters are shown in Table 5.2. For the free-running operation, the frequency down shifts during the 10 ms by 45 MHz (from 173.950 GHz to 173.915 GHz). The frequency jumps described in Section 5.3.1 also appear.

Table 5.2: Operating parameters for frequency stabilization at 174 GHz

Cathode voltage	60	kV
Cathode current	40	A
Main coil current	86	A
Center coil current	77	A
Gun coil current	1.6	A

For the frequency stabilized operation, the gyrotron frequency is stabilized to 173.945 GHz. The PLL system is enabled directly at the start of the pulse. At the start of the pulse, the gyrotron frequency is excited at 173.955 GHz. Until 1.8 ms, the PLL system increases the body voltage to decrease the gyrotron frequency and at 1.8 ms, the gyrotron frequency reaches the set frequency of 173.945 GHz. Afterwards, the PLL system decreases the body voltage such that the gyrotron frequency remains at 173.9415 GHz. In Figure 5.13, the gyrotron frequency is stable from 1.8 ms until the end of the pulse, which is a significant improvement compared to the 35 MHz frequency down shift during the free-running operation (from 1.8 ms until the end of the pulse).

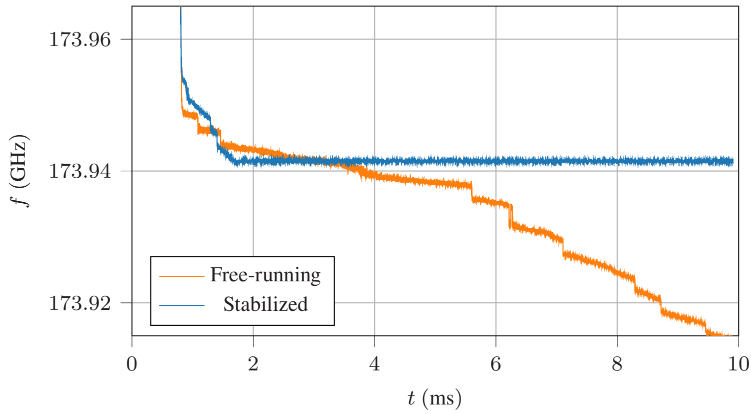

Figure 5.13: Free-running and frequency stabilized (to 173.9415 GHz) operation of the TH1507 Maquette gyrotron (B1) at 174 GHz for 10 ms

In Figure 5.13, no frequency jumps occur during the frequency stabilized operation. However, changing the gyrotron set frequency leads to frequency jumps with the PLL system. In Figure 5.14, frequency jumps during the PLL stabilized gyrotron operation are shown. The set frequency for the gyrotron is 173.940 GHz, which is reached after 2.25 ms. The PLL system tries to stabilize the gyrotron frequency to the set frequency. However, the gyrotron frequency does not reach the set frequency of 173.940 GHz. Instead, the frequency oscillates around 173.940 GHz (between 173.939 GHz and 173.941 GHz).

The body voltage has similar oscillations, which are caused by the PLL system due to the frequency jumps. The PLL system controls the body voltage with which it attempts to stabilize the gyrotron frequency to 173.940 GHz. As soon as the PLL system pulls the gyrotron frequency near 173.940 GHz, the frequency immediately jumps to another frequency. As the gyrotron frequency repeatedly jumps to another frequency and does not remain at 173.940 GHz, the PLL system attempts to counteract the frequency jumps, resulting in the oscillations of the body voltage and the gyrotron frequency around 173.940 GHz.

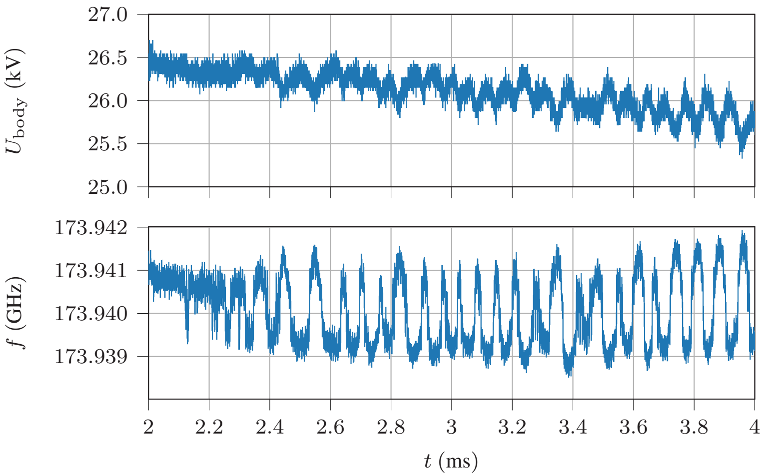

Figure 5.14: Frequency stabilized operation to 173.940 GHz of the TH1507 Maquette gyrotron (B1). The PLL system cannot stabilize the gyrotron frequency to 173.940 GHz due to frequency jumps, resulting in oscillations of the gyrotron frequency around 173.940 GHz.

To further investigate the oscillations and frequency jumps, the body voltage and gyrotron frequency at 3.8 ms in Figure 5.14 is analyzed. At 3.8 ms, the gyrotron frequency is at 173.941 GHz. The PLL system evaluates that the measured frequency is higher than the set frequency (173.940 GHz) and increases the body voltage. With the increasing body voltage, the gyrotron frequency decreases. Without the frequency jumps, the PLL system increases the body voltage until the gyrotron frequency reaches the set frequency. However, in Figure 5.14, the gyrotron frequency does not reach 173.940 GHz, but jumps to 173.939 GHz. Now, the PLL system evaluates that the gyrotron frequency is lower than the set frequency and decreases the body voltage to increase the gyrotron frequency. Again, the gyrotron frequency does not reach 173.940 GHz, but jumps to 173.941 GHz and the process repeats itself.

The PLL system does not cause the oscillations of the gyrotron frequency around 173.940 GHz in Figure 5.14. Oscillations due to control parameters that lead to an unstable operation are excluded. The control parameters used for the gyrotron pulse in Figure 5.14 are the same as the ones used for the gyrotron pulse in Figure 5.13. Moreover, the exact gyrotron operating parameters are used for both gyrotron pulses. Only the set frequency of the PLL system was changed.

Several experiments are conducted to analyze when the frequency jumps occur with the PLL system. It is concluded that the gyrotron frequency can be stabilized without any frequency jumps as in Figure 5.13 when choosing a suitable set frequency. This is a strong indication that the operating TE mode in the TH1507 gyrotron does not oscillate at some specific frequencies. If the gyrotron frequency reaches these frequencies, the frequency jumps to a frequency that has better oscillation conditions.

5.3.3 Long-Pulse Experiments

The short-pulse frequency stabilization from Section 5.3.2 shows that it is possible to frequency stabilize the TH1507 gyrotron without frequency jumps by using an appropriate set gyrotron frequency. The following experiments conducted with the TH1507 gyrotron investigate whether no frequency jumps occur with the PLL system for long pulses (> 1 s) by choosing a suitable set frequency.

In Figure 5.15, the frequency stabilized operation of the TH1507 gyrotron (A1) for a 5 s pulse is shown. When the PLL system is enabled at 1 s, the gyrotron frequency is too low and the PLL system controls the body voltage to stabilize the gyrotron frequency to 140.000 GHz. However, frequency jumps occur during the entire pulse duration, and cause significant interference with the PLL system. Only during certain time periods no frequency jumps occur, and the gyrotron frequency is stable.

The frequency jumps occur consecutively as with the short-pulse experiments when an unfavorable set frequency is chosen. Distinct frequency jump series are visible in Figure 5.15. An example of a frequency jump series is at 1.75 s. The frequency jumps up and down around the set frequency, because the PLL system tries to stabilize the gyrotron frequency onto the set frequency (as explained in

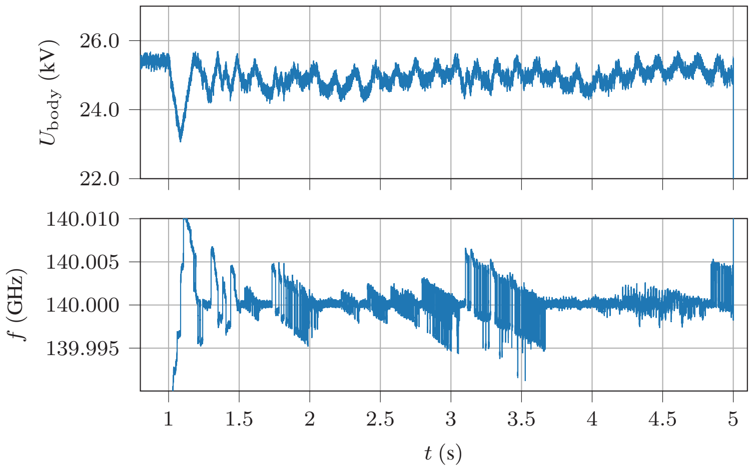

Figure 5.15: Frequency stabilized operation to 140.000 GHz of the TH1507 gyrotron (A1) with frequency jumps

Section 5.3.2). The first frequency onto which the gyrotron jumps to is 4.5 MHz higher than the set frequency. With each consecutive frequency jump, the upper and lower jump frequencies decrease. When the jump frequency reaches the set frequency, the frequency jumps disappear and the gyrotron frequency is stable until a new frequency jump series starts again.

Several experiments are conducted and it was not possible to find a suitable set frequency at which no frequency jumps appear for the entire pulse.

5.3.4 Discussion

In this section, the frequency stabilization of the TH1507 gyrotrons is investigated. As opposed to the VGT8141A gyrotron, the main challenges are the frequency jumps that are only observed with the TH1507 gyrotrons. For the short-pulse operation, the frequency is stabilized successfully as with the VGT8141A gyrotron.

This fulfills the requirements for the CTS diagnostic. If a suitable set frequency is chosen, the frequency of the TH1507 gyrotron at 174 GHz is stabilized for the last 8 ms of the pulse and no frequency jumps occur.

With the PLL system, the frequency jumps of the TH1507 gyrotrons are further analyzed and new insights into the frequency jumps are obtained. The short-pulse experiments in Section 5.3.2 show that the TH1507 gyrotrons prefer to oscillate on some frequencies and avoid oscillations on other frequencies. If the gyrotron frequency reaches the frequencies at which the gyrotron avoids excitation, frequency jumps occur. With the PLL system, these frequency jumps are enforced if a suitable set frequency is chosen (Figure 5.14). A reasonable explanation for why the sudden frequency jumps occur and how they behave has not yet been found.

5.4 Summary

The implemented PLL system from Section 3.3.2 is successfully applied to the W7-X gyrotrons. The experiments show a significant increase in the frequency stability of the W7-X gyrotrons. During LP experiments, the VGT8141A gyrotron was frequency stabilized onto a desired set frequency. In the frequency spectrum, a clear main peak is visible at the set frequency and a full -20 dB bandwidth of below 100 kHz was achieved.

For the CTS diagnostic, the TH1507 Maquette gyrotron is successfully frequency stabilized at 174 GHz during 10 ms. The frequency jumps of the TH1507 gyrotrons are investigated, and can be avoided during the frequency stabilized short-pulse operation. Frequency jumps do not occur with the TH1507 Maquette gyrotron during the first 10 ms if a suitable set frequency is chosen. The requirements for the CTS diagnostics are fulfilled and the CTS diagnostic uses the PLL system in the W7-X OP 2.1.

6 Considerations on Triode-Type Operation for TH1507U Gyrotron

So far, the implemented frequency stabilization system has been designed for gyrotrons with a diode-type MIG, but it can also be used for gyrotrons with a triode-type MIG. Instead of controlling the body voltage, the frequency of the gyrotron is changed by controlling the modulation anode voltage. An advantage of the triode-type MIG is that the pitch factor can be independently changed. Thus, it is possible to change the output power and frequency of the gyrotron independently. For future gyrotron operation, a more advanced control system can be used to control output power and frequency. Furthermore, the capacitance of the modulation anode is smaller than the capacitance of the body [55]. This allows a faster control of the modulation anode, because smaller currents are needed to charge the modulation anode capacitance.

Design changes are not required for the PLL system. however, the control voltage from the PLL system needs to be applied on the modulation anode, and a suitable power supply needs to be available. Furthermore, the control parameters need to be changed for the new setup. To find the optimal control parameters, the gyrotron frequency behavior on the modulation anode is investigated.

The theoretical investigations on the triode-type operation are conducted on the W7-X upgrade gyrotron TH1507U [38]. The current design of the TH1507U gyrotron has a diode-type MIG. Changes on the existing diode-type MIG of the TH1507U gyrotrons are investigated to modify it into a triode-type MIG. The influence of the altered MIG on the electron beam parameter and interaction is analyzed by using *ESRAY* and *EURIDICE*. Finally, the frequency behavior on the modulation anode is theoretically determined.

6.1 Changes on the Electron Gun of the TH1507U Gyrotron

The design of the TH1507U gyrotron is presented in [38]. The TH1507U gyrotron has an output power of 1.5 MW and its oscillating mode is the $\mathrm{TE}_{28,10}$ mode. In Figure 6.1a, the geometry from the diode-type MIG to the middle of the cavity is shown.

In a triode-type MIG, the anode is divided into an additional modulation anode and the main anode. The electric potential of the modulation anode and main anode are changed independently, giving an additional degree of freedom for the gyrotron operation. While the potential difference between the cathode and main anode determines the kinetic energy of the electrons at the cavity, the potential of the modulation anode is used to change the pitch factor of the electrons independently.

To achieve different potentials between modulation anode and main anode, an insulation is needed. For triode-type configuration of the TH1507U gyrotron, the possible insulator positions between the anode and the start of the cavity are investigated.

To keep a consistent notation with the diode-type configuration, the following terminology is used :

- **Cathode:** The cathode remains as is. The cathode potential is denoted with U_{cath}.

- **Body:** All gyrotron sub-components that have the same potential as the cavity are referred to as body. The body potential is denoted with U_{body} and determines (with the cathode potential) the kinetic energy of the electrons at the cavity. The accelerating voltage is the difference between cathode and body potential.

- **Modulation anode:** The modulation anode for the triode-type MIG can have a different potential than the cavity. The potential of the modulation anode is denoted with U_{mod}. U_{mod} can also be used for power modulations.

Furthermore, the TH1507U gyrotron has a depressed collector, which is on ground potential.

To change the TH1507U diode-type MIG to a triode-type MIG, the new design shall be as close to the design with diode-type MIG to ensure a similar operation. Moreover, if the U_{mod} is the same as U_{body} for the triode-type MIG, the electron beam parameters at the center of the cavity shall be the same as for the diode-type MIG. Without changing the geometry of the TH1507U gyrotron, the only free parameter for the triode-type configuration is the position of the insulator.

In this chapter, two positions are investigated that are also suitable to implement for the TH1507U gyrotron:

- Between the beam tunnel and the cavity. With this position, the beam tunnel has the same potential as the modulation anode.

- Between the anode and beam tunnel. With this position, the beam tunnel has the same potential as cavity.

In Figure 6.1, the position for the insulator is shown for both cases. As a reference, the diode-type geometry is also shown. The geometry shown in Figure 6.1 is used for the simulation of the electron beam parameters. The insulation is simulated by a gap. The position of the insulation is investigated and its impact on the electron beam parameters is determined.

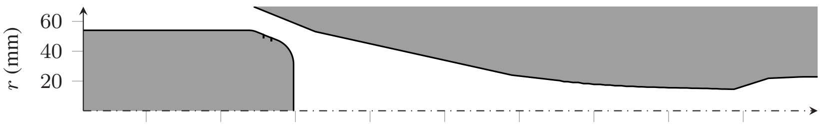

(a) Existing diode-type MIG

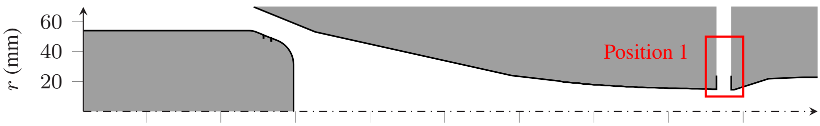

(b) Insulator position 1 for triode-type MIG

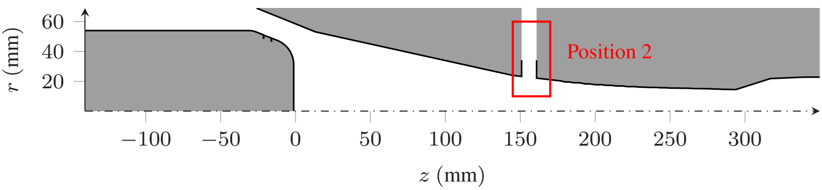

(c) Insulator position 2 for triode-type MIG

Figure 6.1: Geometry from the MIG to the center of the cavity of the TH1507U gyrotron for the diode-type MIG and triode-type MIG with different insulator positions

6.2 Simulations of the Triode-Type MIG

The MIG is simulated using *ESRAY* for the diode-type and triode-type configuration with the two insulator positions. The influence of different modulation anode voltages on the electron beam parameters is investigated. The operating parameters for all simulations are shown in Table 6.1.

First the electron beam parameters along the trajectory of the electrons are analyzed for different values of U_{mod}. In the simulation, the operating parameters from Table 6.1 are used, only the modulation anode voltage U_{mod} is changed. The

Table 6.1: Operating parameters

Main coil current	I_{MC}	87.20	A
Gun coil current	I_{GTC}	-1.07	A
Magnetic field	B_{cav}	5.56	T
Cathode potential	U_{cath}	-55.00	kV
Body potential	U_{body}	27.75	kV
Beam current	I_{beam}	55	A
Neutralization	η_{neut}	67	%

influence of the different insulator positions on the mean electron kinetic energy W_{kin} and mean pitch factor α along the electron trajectory from the emitter to the center of the cavity is shown in Figure 6.2. For comparison, W_{kin} and α are also shown from the diode-type configuration. The different values for the U_{mod} are shown for the triode-type configurations. The U_{mod} has the values 22.75 kV (dash dotted), 27.75 kV (dashed) and 32.75 kV, while the body voltage U_{body} has always 27.75 kV. In Figure 6.2, the trajectory of the electrons is from the emitter (-30 mm) to the center of the cavity (350 mm). Both insulator positions are marked with the gray areas.

If in both triode-type configurations the U_{mod} is equal to U_{body}, the curves of W_{kin} and α follow without any significant difference the curves of the diode-type configuration. Therefore, with equal U_{mod} and U_{body}, the insulator has does not change the electron beam parameters, and the triode-type configurations behave as the diode-type configuration.

With different values for U_{mod}, the curves of the kinetic energy and pitch factor change along the electron trajectory. At the cavity center, the electron beam has always similar mean W_{kin} (80 keV), because the cavity is for all configurations at the same potential ($U_{\mathrm{body}} = 27.75$ kV). The kinetic energy along the electron trajectory depends on the insulator position. If U_{mod} is different than U_{body},

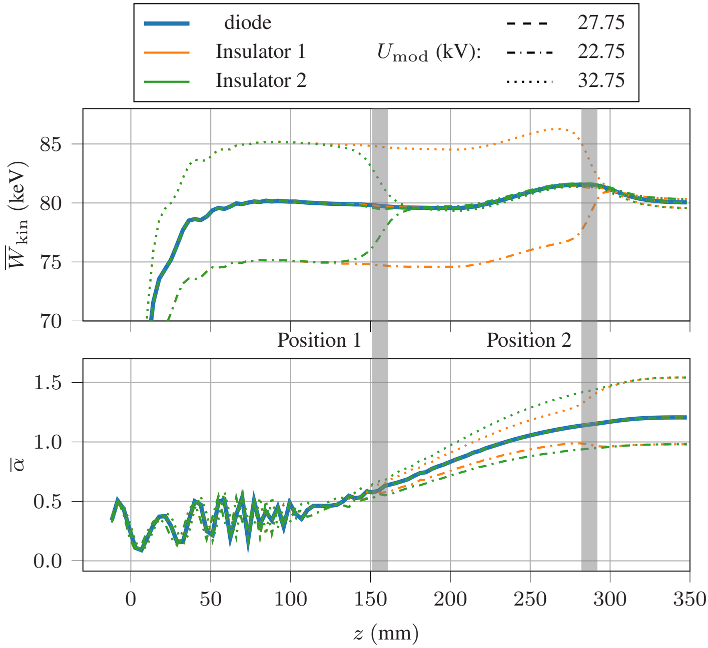

Figure 6.2: Mean electron beam parameters for different MIG configurations along the electron trajectory from emitter (−30 mm) to the center of the cavity (350 mm): W_{kin} and α. Diode-type configuration is shown in blue, insulator position 1 in orange and insulator position 2 in green. The body voltage U_{body} is 27.75 kV and the electron beam parameters for different modulation anode voltages are shown.

the kinetic energy is also different from the diode-type configuration until the insulator position. The position at which W_{kin} changes in Figure 6.2 is at the respective insulator position.

While the kinetic energy at the cavity center does not change for different U_{mod} values, the pitch factor at the cavity center depends on U_{mod}. Along the electron trajectory, the pitch factor also jumps at the insulator position, as with W_{kin}.

At the cavity center, the electron beam parameters differ not significantly for the two insulator positions if the same U_{mod} and U_{body} is applied. Other simulations with different insulator positions show the same results. As long as the insulator position is not too close to the cathode, the insulator position does not change the electron beam parameters at the cavity. Therefore, in the following simulations, only the results of insulator position 2 are shown.

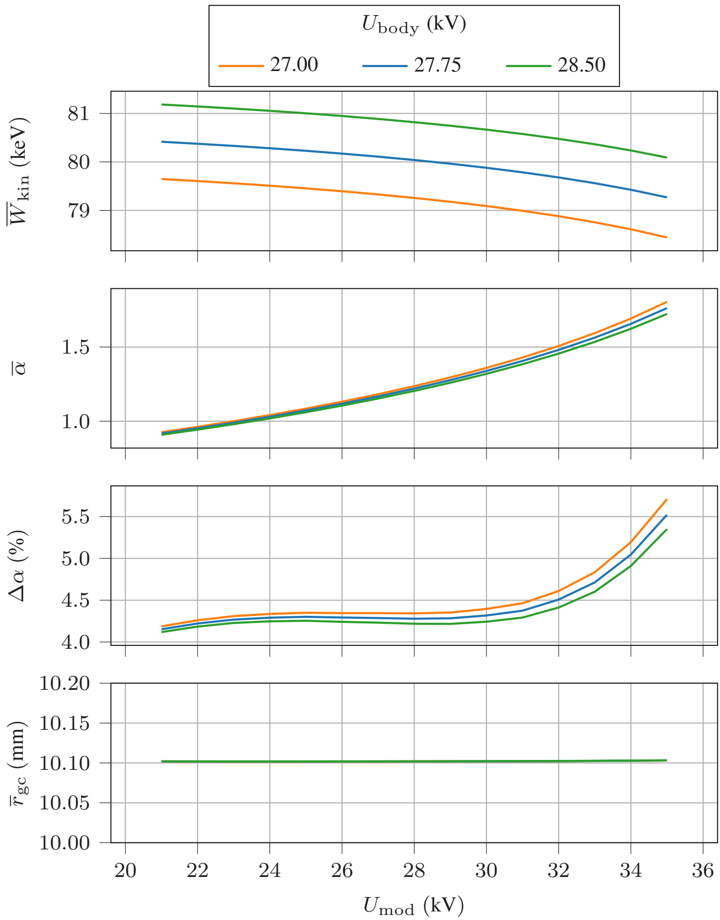

Figure 6.3: Electron beam parameters at the center of the cavity for different values of U_{body} and U_{mod}

The dependence of the electron beam parameters at the cavity on the modulation anode voltage is further investigated. In Figure 6.3, the mean kinetic energy, mean pitch factor α, pitch factor spread and mean guiding center radius at the cavity for different U_{mod} are shown. The U_{mod} is varied between 21 kV to 35 kV. Furthermore, the influence of U_{body} is also shown in Figure 6.3 and the electron beam parameters are evaluated for body voltages of 26.5 kV, 27 kV and 27.5 kV.

In Figure 6.3, the guiding center radius r_{g} does not dependent on U_{mod}. r_{g} only depends on the magnet coil currents, which are constant in these simulations. On the other hand, the value for α at the center of the cavity clearly changes with U_{mod}. This allows to vary α independently of the other electron beam parameters, and provides an additional degree of freedom for the gyrotron operation.

The influence of U_{mod} on the pitch factor is high and α increases with increasing U_{mod}. A linear regression of the curve results in a linear dependence of the pitch factor on U_{mod} with a slope of 0.047/kV. Furthermore, the pitch factor mainly depends on U_{mod} and the influence of the body voltage on the pitch factor is negligible.

The pitch factor spread also depends on U_{mod}. However, the pitch factor spread increases only significantly for U_{mod} values above 32 kV, where the mean pitch factor is above 1.5. The pitch factor spread for U_{mod} between 22 kV to 30 kV is nearly constant and below 4.5 %.

The mean kinetic energy is also influenced by U_{mod} and decreases with increasing U_{mod} (with U_{body} potential). The dependence of the mean kinetic energy on U_{mod} is indirect. Because the pitch factor changes, the electron beam charge also changes. The voltage depression of the electron beam is higher for higher pitch factor (Equation 2.13), resulting in a lower electron kinetic energy. The mean electron kinetic energy changes by 0.5 keV if U_{mod} changes by 7 kV.

6.3 Interaction Simulations

With the electron beam parameters from Section 6.2, the interaction with the nominal $\mathrm{TE}_{28,10}$ mode is analyzed by using *EURIDICE*. The interaction simulations with *EURIDICE* are conducted as single mode simulations and the operating parameters from Table 6.1 with the electron beam parameters calculated by *ESRAY* are used. The $\mathrm{TE}_{28,10}$ mode is excited with different electron beam parameters, that are obtained for different U_{body} and U_{mod} values. The power at the output of the cavity and the excited frequencies are obtained by averaging over time when the $\mathrm{TE}_{28,10}$ mode is excited.

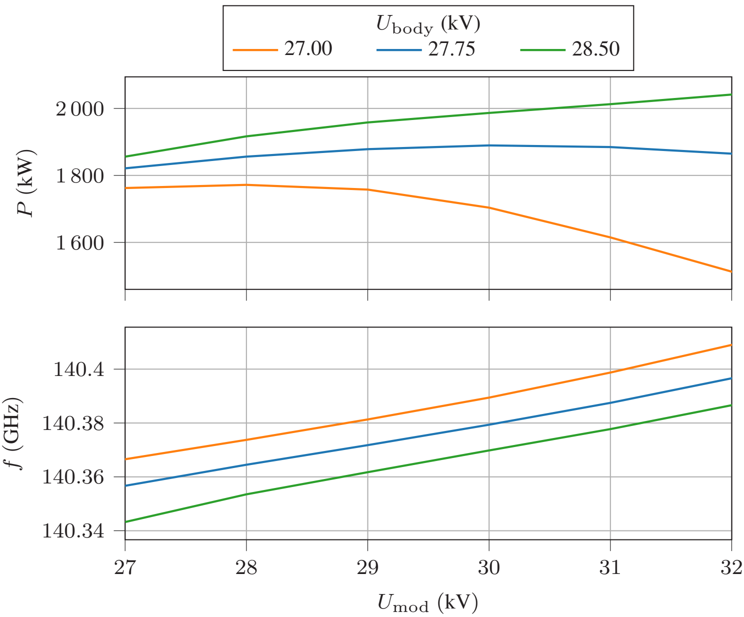

Figure 6.4: Output power at the end of the cavity and frequency for different U_{mod} and U_{body}

In Figure 6.4, the output power and frequency for different U_{mod} and U_{body} is shown. For modulation anode voltages below 25 kV, the $\mathrm{TE}_{28,10}$ mode could not be excited, because the pitch factor changes to values that are too low excitation (< 1.1). Increasing the U_{mod} from 25 kV to 28 kV results in a higher output power, which is expected due to the increasing pitch factor. However, further increasing U_{mod} decreases the output power. Even though the pitch factor increases, the kinetic energy also decreases. At some point, the pitch factor does not increase enough to compensate for the decrease in kinetic energy, resulting in a lower output power.

For the frequency stabilization system, the dependence of the excited frequency on U_{mod} is important. In Figure 6.4, the excited frequency depends nearly linearly on U_{mod} between 25 kV to 31 kV. The linear dependence also does not change with different body voltages. In Table 6.2, the slope of the linear regression of the frequency dependence on U_{mod} is shown for different values of U_{body}.

Table 6.2: Linear frequency dependence on U_{mod}

U_{body} (kV)	Slope ($\frac{\mathrm{MHz}}{\mathrm{kV}}$)
82.00	8.8
82.75	8.2
83.50	8.3

For the nominal body voltage of 27.75 kV, the power varies by 100 kW for modulation anode voltages between 27 kV to 32 kV. In this U_{mod} range, the frequency can be changed in a range of 40 MHz. In comparison, changing the set frequency through the accelerating voltage with a diode-type MIG results in larger power changes.

6.4 Summary

The step towards a triode-type MIG for the W7-X TH1507U gyrotron has been theoretically analyzed. For a triode-type MIG, an insulation between modulation anode and cavity is necessary. The position of the insulator was investigated. Changing the position of the insulator does not change the electron beam parameters at the cavity for the same operating point. The simulations with *ESRAY* show that the pitch factor of the electrons can be changed independently from the other electron beam parameters.

For the frequency stabilization system, the frequency dependence on the modulation anode voltage was analyzed. At the nominal operating point with a body voltage of 27.75 kV, the frequency dependence on the modulation anode voltage is 8.2 MHz/kV. The main advantage of controlling the frequency with the body voltage is that the gyrotron output power depends much less on the modulation anode voltage. Furthermore, the additional degree of freedom can be used to decouple the output frequency from the output power. Thus, more elaborated control systems that control the gyrotron output power and frequency simultaneously are possible.

7 Conclusion and Outlook

For the first time, a PLL based frequency stabilization system for megawatt-class gyrotrons with a diode-type MIG has been developed and experimentally tested. The experiments demonstrate its capabilities and future challenges. The introduction of frequency-stabilized gyrotrons using PLL systems paves the way for a significant technological advance in applications using MW-class gyrotrons. The PLL system not only enhances the performance of the CTS diagnostic by providing a stable, narrowband gyrotron frequency, but it also enables new applications such as plasma experiments with direct ion heating via beat waves with two gyrotrons.

To use a PLL on MW-class gyrotrons, the frequency dependence of gyrotrons on several operating parameters is investigated. For gyrotrons with a diode-type MIG, the most suitable operating parameter for frequency stabilization is the accelerating voltage, as it can be adjusted faster than the magnetic field strength. The frequency dependence on the accelerating voltage is linearized for a fixed operating point, and the gyrotron is modeled as a VCO for the PLL system.

The PLL system has been implemented for the ECRH gyrotrons at the W7-X stellarator to demonstrate its capabilities. The frequency is controlled with the body high-voltage power supply, which allows modulating the accelerating voltage with frequencies of up to 20 kHz. Frequency stabilization experiments with the gyrotrons VGT8141A from manufacturer *CPI* and TH1507 from manufacturer *THALES* are conducted.

In long-pulse experiments, the VGT8141A gyrotron is frequency stabilized after 1 s for up to 60 s. When operated free-running, the frequency of the VGT8141A gyrotron drifts during this time period in the range of 5 MHz. The PLL system substantially reduces these long-term frequency drifts. During the experiments, the VGT8141A gyrotron is stabilized in a frequency range between 139.960 GHz to 140.010 GHz.

The significant improvement in frequency stability with the PLL system is most evident in the frequency spectrum. Compared to the free-running operation, where the frequency spectrum spreads over a band of frequencies and lacks a distinct main peak, the gyrotron spectrum during the frequency stabilized operation has one distinct main peak at the set frequency. A full -20 dB bandwidth of below 100 kHz is achieved. The remaining frequency fluctuations appear as sidebands in the frequency spectrum, the most prominent ones occurring at harmonics of 3.3 kHz and 135 kHz. These frequencies are identical to the spectral lines in the measured noise of the cathode power supply, which is based on the PSM principle. Based on these findings, it can be concluded that the body power supply cannot be modulated fast enough to effectively counter this noise from the cathode power supply.

For the frequency stabilization of the TH1507 gyrotrons, the sudden frequency jumps pose a challenge to the PLL system. For short-pulses in the range of 10 ms, the PLL system successfully stabilizes the gyrotron frequency for a specific set frequency, where the frequency jumps are avoided. However, for the long-pulse frequency stabilization, the sudden frequency jumps still occur and cannot be completely avoided with the PLL system. The sudden frequency jumps, which are until now only observed in the TH1507 gyrotrons, require further investigation.

The CTS diagnostic system at W7-X requires a stable gyrotron frequency for the first 9 ms of a pulse at 174 GHz. The 174 GHz operation of the TH1507 Maquette gyrotron is theoretically and experimentally investigated. During the experiments, the $TE_{34,10}$ mode is successfully excited with an output power of 300 kW. In addition, short-pulse experiments with the PLL system are conducted at 174 GHz. The free-running 30 MHz frequency drift, which is caused by cavity heating and electron beam neutralization, is successfully stabilized for a time duration of 9 ms. The PLL system allows the gyrotron frequency to be precisely matched to the notch filter of the CTS receiver, allowing a successful use of the CTS diagnostic at W7-X during the operation phase 2.1 in March 2023.

The ability to precisely set the gyrotron frequency is also an essential requirement for plasma experiments on direct ion heating with beat waves generated from two frequency stabilized gyrotrons. A second PLL system for the TH1507 Upgrade gyrotron will be implemented in conjunction with the PLL system for the VGT8141A gyrotron to enable beat wave experiments in the future.

The experimental results show that the power supplies are the main limitation for the frequency stabilization of high-power gyrotrons. To further enhance the gyrotron frequency stability, two improvements are identified: stricter requirements on the power supply noise and ripple, or increasing the PLL control bandwidth. Reducing the noise on power supply systems with PSM technology is challenging to implement due to the inherent switching noise. Increasing the PLL control bandwidth for gyrotrons with diode-type MIG requires a faster control of the accelerating voltage. Investigations will be conducted to place a fast amplifier, which can be modulated in the 1 kV range, in series to the body power supply for faster frequency control with the PLL system.

When stabilizing the frequency with the accelerating voltage, the output power and frequency cannot be changed independently. Specifically, the output power depends on the chosen set gyrotron frequency. Gyrotrons with a triode-type MIG enable the use of advanced control systems with which it is possible to control output power and frequency. In addition, the size of the modulation anode is smaller than the size of the gyrotron body, resulting in a smaller capacitance and possible faster modulation speeds.

List of Figures

List of Tables

Bibliography

[1] F. F. Chen, *An Indispensable Truth*. New York, NY: Springer, 2011, ISBN: 978-1-4419-7819-6. DOI: 10.1007/978-1-4419-7820-2

[2] T. R. Karl and K. E. Trenberth, “Modern Global Climate Change,” *Science*, vol. 302, no. 5651, pp. 1719–1723, Dec. 2003. DOI: 10.1126/science.1090228

[3] J. Sheffield, “The physics of magnetic fusion reactors,” *Reviews of Modern Physics*, vol. 66, no. 3, pp. 1015–1103, Jul. 1994. DOI: 10.1103/RevModPhys.66.1015

[4] V. Flyagin, A. Gaponov, I. Petelin, and V. Yulpatov, “The Gyrotron,” *IEEE Transactions on Microwave Theory and Techniques*, vol. 25, no. 6, pp. 514–521, Jun. 1977. DOI: 10.1109/TMTT.1977.1129149

[5] S. B. Korsholm, H. Bindslev, V. Furtula, F. Leipold, F. Meo, P. K. Michelsen, D. Moseev, S. K. Nielsen, M. Salewski, and M. Stejner, “Collective Thomson scattering capabilities to diagnose fusion plasmas,” *Nuclear Instruments and Methods in Physics Research Section A: Accelerators, Spectrometers, Detectors and Associated Equipment*, 1rs International Conference on Frontiers in Diagnostics Technologies, vol. 623, no. 2, pp. 677–680, Nov. 2010. DOI: 10.1016/j.nima.2010.05.003

[6] H. P. Laqua, D. Moseev, P. Helander, P. Aleynikov, S. Marsen, N. B. Maruschenko, and T. Stange, “Generation of electrostatic oscillations in the ion cyclotron frequency range by modulated ECRH,” *Nuclear Fusion*, vol. 58, no. 10, p. 104 003, Aug. 2018. DOI: 10.1088/1741-4326/aad754

[7] R. E. Best, *Phase-Locked Loops: Design, Simulation, and Applications*, 6. ed. New York: McGraw-Hill, 2007, ISBN: 978-0-07-149375-8

[8] A. Fokin, M. Glyavin, G. Golubiatnikov, L. Lubyako, M. Morozkin, B. Movschevich, A. Tsvetkov, and G. Denisov, "High-power sub-terahertz source with a record frequency stability at up to 1 Hz," *Scientific Reports*, vol. 8, Mar. 2018. DOI: `10.1038/s41598-018-22772-1`

[9] G. Denisov, A. Kuftin, M. Glyavin, A. Tsvetkov, G. Golubiatnikov, E. Tai, E. Soluyanova, M. Bakulin, A. Fokin, M. Shmelev, and B. Movshevich, "Experimental tests of a high-stable 170 GHz/25 kW gyrotron as a master oscillator for frequency locking of megawatt level microwave sources," in *2021 22nd International Vacuum Electronics Conference (IVEC)*, Apr. 2021, pp. 1–2. DOI: `10.1109/IVEC51707.2021.9722456`

[10] A. Piel, *Plasma Physics: An Introduction to Laboratory, Space, and Fusion Plasmas*. Springer Berlin Heidelberg, 2010, ISBN: 978-3-642-10490-9. DOI: `10.1007/978-3-642-10491-6`

[11] J. D. Lawson, "Some Criteria for a Power Producing Thermonuclear Reactor," *Proceedings of the Physical Society. Section B*, vol. 70, no. 1, p. 6, Jan. 1957. DOI: `10.1088/0370-1301/70/1/303`

[12] O. Mitarai, C. Xiao, D. McColl, M. Dreval, A. Hirose, and M. Peng, "Plasma current start-up by the outer ohmic heating coils in the Saskatchewan TORus Modified (STOR-M) iron core tokamak," *Review of Scientific Instruments*, vol. 86, no. 3, p. 033 508, Mar. 2015. DOI: `10.1063/1.4915316`

[13] R. Hemsworth, H. Decamps, J. Graceffa, B. Schunke, M. Tanaka, M. Dremel, A. Tanga, H. P. L. D. Esch, F. Geli, J. Milnes, T. Inoue, D. Marcuzzi, P. Sonato, and P. Zaccaria, "Status of the ITER heating neutral beam system," *Nuclear Fusion*, vol. 49, no. 4, p. 045 006, Apr. 2009. DOI: `10.1088/0029-5515/49/4/045006`

[14] F. Mirizzi, A. Cardinali, R. Maggiora, L. Panaccione, G. Ravera, and A. Tuccillo, "Conceptual Design of the ICRH and LHCD Systems for FT-3," in *2007 IEEE 22nd Symposium on Fusion Engineering*, Jun. 2007, pp. 1–4. DOI: `10.1109/FUSION.2007.4337936`

[15] R. C. Wolf, S. Bozhenkov, A. Dinklage, *et al.*, "Electron-cyclotron-resonance heating in Wendelstein 7-X: A versatile heating and current-drive method and a tool for in-depth physics studies," *Plasma Physics and Controlled Fusion*, vol. 61, no. 1, p. 014 037, Nov. 2018. DOI: `10.1088/1361-6587/aaeab2`

[16] C. Luttrell, E. Coffey, I. Griffith, G. Hanson, A. Lumsdaine, and C. Schaich, "Analysis of the ITER ECH Waveguide Transmission Line Expansion Unit," *Fusion Science and Technology*, vol. 72, no. 3, pp. 312–317, Oct. 2017. DOI: `10.1080/15361055.2017.1333847`

[17] H. P. Laqua, J. Baldzuhn, H. Braune, *et al.*, "High-performance ECRH at W7-X: experience and perspectives," *Nuclear Fusion*, vol. 61, no. 10, p. 106 005, Aug. 2021. DOI: `10.1088/1741-4326/ac1a1b`

[18] T. Ruess, "A First 2 MW-Class (136)/170/204 GHz Multi-Frequency Gyrotron Pre-Prototype for DEMO: Design, Construction and Key Components Verification," Ph.D. dissertation, Karlsruhe Institute of Technology, 2023, DOI: `10.5445/IR/1000159505`

[19] H. P. Laqua, K. A. Avramidis, H. Braune, *et al.*, "The ECRH-Power Upgrade at the Wendelstein 7-X Stellarator," *EPJ Web of Conferences*, vol. 277, p. 04 003, 2023. DOI: `10.1051/epjconf/202327704003`

[20] C. Darbos, M. Henderson, F. Albajar, *et al.*, "ECRH System For ITER," *AIP Conference Proceedings*, vol. 1187, no. 1, pp. 531–538, Nov. 2009. DOI: `10.1063/1.3273807`

[21] J. Jelonnek, "Untersuchung des Lastverhaltens von Gyrotrons," Ph.D. dissertation, Technischen Universität Hamburg-Harburg, Düsseldorf, 2000, ISBN: 3-18-329721-3

[22] A. S. Gilmour Jr., *Microwave tubes*. Dedham, MA : Artech House, Dec. 1986, 490 pp., ISBN: 978-0-89006-181-7

[23] G. Giruzzi, J. F. Artaud, V. Basiuk, J. Garcia, F. Imbeaux, and M. Schneider, "Integrated modelling of ITER hybrid scenarios with ECCD," in *Electron Cyclotron Emission and Electron Cyclotron Resonance Heating (EC-15)*, WORLD SCIENTIFIC, Apr. 2009, pp. 307–312, ISBN: 978-981-281-463-0. DOI: `10.1142/9789812814647_0043`

[24] F. M. Poli, E. Fredrickson, M. A. Henderson, N. Bertelli, D. Farina, L. Figini, and E. Poli, "EC power management in ITER for NTM control: the path from the commissioning phase to demonstration discharges," *EPJ Web of Conferences*, vol. 157, p. 03 041, 2017. DOI: `10.1051/epjconf/201715703041`

[25] G. Grieger, W. Lotz, P. Merkel, *et al.*, "Physics optimization of stellarators," *Physics of Fluids B: Plasma Physics*, vol. 4, no. 7, pp. 2081–2091, Jul. 1992. DOI: `10.1063/1.860481`

[26] F. Warmer, C. D. Beidler, A. Dinklage, R. Wolf, and the W7-X Team, "From W7-X to a HELIAS fusion power plant: motivation and options for an intermediate-step burning-plasma stellarator," *Plasma Physics and Controlled Fusion*, vol. 58, no. 7, p. 074 006, Jun. 2016. DOI: `10.1088/0741-3335/58/7/074006`

[27] T. Klinger, A. Alonso, S. Bozhenkov, *et al.*, "Performance and properties of the first plasmas of Wendelstein 7-X," *Plasma Physics and Controlled Fusion*, vol. 59, no. 1, p. 014 018, Oct. 2016. DOI: `10.1088/0741-3335/59/1/014018`

[28] C. Beidler, G. Grieger, F. Herrnegger, E. Harmeyer, J. Kisslinger, W. Lotz, H. Maassberg, P. Merkel, J. Nührenberg, F. Rau, J. Sapper, F. Sardei, R. Scardovelli, A. Schlüter, and H. Wobig, "Physics and Engineering Design for Wendelstein VII-X," *Fusion Technology*, vol. 17, no. 1, pp. 148–168, Jan. 1990. DOI: `10.13182/FST90-A29178`

[29] H.-S. Bosch, R. C. Wolf, T. Andreeva, *et al.*, "Technical challenges in the construction of the steady-state stellarator Wendelstein 7-X," *Nuclear Fusion*, vol. 53, no. 12, p. 126 001, Nov. 2013. DOI: `10.1088/0029-5515/53/12/126001`

[30] J. Nührenberg, W. Lotz, P. Merkel, C. Nührenberg, U. Schwenn, E. Strumberger, and T. Hayashi, "Overview on Wendelstein 7-X Theory," *Fusion Technology*, vol. 27, no. 3, pp. 71–78, Apr. 1995. DOI: 10.13182/FST95-A11947048

[31] A. Dinklage, C. D. Beidler, P. Helander, *et al.*, "Magnetic configuration effects on the Wendelstein 7-X stellarator," *Nature Physics*, vol. 14, no. 8, pp. 855–860, Aug. 2018. DOI: 10.1038/s41567-018-0141-9

[32] V. Erckmann, P. Brand, H. Braune, *et al.*, "Electron Cyclotron Heating for W7-X: Physics and Technology," *Fusion Science and Technology*, vol. 52, no. 2, pp. 291–312, Aug. 2007. DOI: 10.13182/FST07-A1508

[33] T. Stange, H. P. Laqua, M. Beurskens, *et al.*, "Advanced electron cyclotron heating and current drive experiments on the stellarator Wendelstein 7-X," *EPJ Web of Conferences*, vol. 157, p. 02 008, 2017. DOI: 10.1051/epjconf/201715702008

[34] R. C. Wolf, A. Alonso, S. Äkäslompolo, *et al.*, "Performance of Wendelstein 7-X stellarator plasmas during the first divertor operation phase," *Physics of Plasmas*, vol. 26, no. 8, p. 082 504, Aug. 2019. DOI: 10.1063/1.5098761

[35] J. Ongena, A. Messiaen, D. Van Eester, *et al.*, "Study and design of the ion cyclotron resonance heating system for the stellarator Wendelstein 7-X," *Physics of Plasmas*, vol. 21, no. 6, p. 061 514, Jun. 2014. DOI: 10.1063/1.4884377

[36] M. Thumm, S. Alberti, A. Arnold, *et al.*, "EU Megawatt-Class 140-GHz CW Gyrotron," *IEEE Transactions on Plasma Science*, vol. 35, no. 2, pp. 143–153, Apr. 2007. DOI: 10.1109/TPS.2007.892144

[37] M. Blank, K. Felch, P. Borchard, P. Cahalan, S. Cauffman, T. S. Chu, and H. Jory, "Demonstration of a high-power long-pulse 140-GHz gyrotron oscillator," *IEEE Transactions on Plasma Science*, vol. 32, no. 3, pp. 867–876, Jun. 2004. DOI: 10.1109/TPS.2004.828815

[38] K. A. Avramidis, Z. C. Ioannidis, G. Aiello, *et al.*, “Towards a 1.5 MW, 140 GHz gyrotron for the upgraded ECRH system at W7-X,” *Fusion engineering and design*, vol. 164, p. 112 173, 2021. DOI: `10.1016/j.fusengdes.2020.112173`

[39] W. Kasparek, L. Empacher, V. Erckmann, G. Gantenbein, F. Hollmann, P.-G. Schüller, K. Schwörer, and M. Weißgerber, “The Multi-Beam Transmission System for 140 GHz Electron Cyclotron Heating on the Stellarator W7-X: Concept, Design and First Tests,” *Frequenz*, vol. 55, no. 9, pp. 263–269, Sep. 2001. DOI: `10.1515/FREQ.2001.55.9-10.263`

[40] W. Kasparek, P. Brand, H. Braune, *et al.*, “Status of the 140GHz, 10MW CW transmission system for ECRH on the stellarator W7-X,” *Fusion Engineering and Design*, Proceedings of the 23rd Symposium of Fusion Technology, vol. 74, no. 1, pp. 243–248, Nov. 2005. DOI: `10.1016/j.fusengdes.2005.06.247`

[41] W. Kasparek, M. Petelin, D. Shchegolkov, V. Erckmann, B. Plaum, A. Bruschi, I. Greifswald, F. Karlsruhe, and I. Stuttgart, “FaDiS, a fast switch and combiner for high-power millimetre wave beams,” in *2007 Joint 32nd International Conference on Infrared and Millimeter Waves and the 15th International Conference on Terahertz Electronics*, Sep. 2007, pp. 389–390. DOI: `10.1109/ICIMW.2007.4516546`

[42] W. Kasparek, M. I. Petelin, D. Y. Shchegolkov, V. Erckmann, B. Plaum, A. Bruschi, E. G. a. I. Greifswald, F. Z. K. Karlsruhe, and I. P. F. Stuttgart, “A fast switch, combiner and narrow-band filter for high-power millimetre wave beams,” *Nuclear Fusion*, vol. 48, no. 5, p. 054 010, May 2008. DOI: `10.1088/0029-5515/48/5/054010`

[43] W. Kasparek, M. Petelin, V. Erckmann, A. Bruschi, F. Noke, F. Purps, F. Hollmann, Y. Koshurinov, L. Lubyako, B. Plaum, and W. Wubie, “High-power microwave diplexers for advanced ECRH systems,” *Fusion Engineering and Design*, Proceeding of the 25th Symposium on Fusion Technology, vol. 84, no. 2, pp. 1002–1005, Jun. 2009. DOI: `10.1016/j.fusengdes.2008.11.070`

[44] V. Erckmann, W. Kasparek, Y. Koshurinov, L. Lubyako, M. I. Petelin, D. Y. Shchegolkov, F. Hollmann, G. Michel, F. Noke, and F. Purps, "Power Combination of Two 140-GHz Gyrotrons and Fast Switching of the Combined Beam," *Fusion Science and Technology*, vol. 55, no. 1, pp. 23–30, Jan. 2009. DOI: `10.13182/FST09-A4050`

[45] T. L. Rhodes, W. A. Peebles, K. H. Burrell, G. R. McKEE, J. Lohr, C. C. Petty, X. V. Nguyen, E. J. Doyle, C. M. Greenfield, L. Zeng, and G. Wang, "ETG Scale Turbulence and Transport in the DIII–D Tokamak," Chengdu, China, Oct. 2006

[46] A. Fasoli, J. A. Dobbing, C. Gormezano, J. Jacquinot, J. B. Lister, S. E. Sharapov, and A. Sibley, "Alfven eigenmode excitation by ICRH beat waves," *Nuclear Fusion*, vol. 36, no. 2, pp. 258–263, Feb. 1996. DOI: `10.1088/0029-5515/36/2/I13`

[47] K. Sassenberg, M. Maraschek, P. J. M. Carthy, W. Bobkov, M. García-Muñoz, N. Hicks, V. Igochine, P. Lauber, and S. G. and, "ICRH beatwave excited toroidicity induced Alfvén eigenmodes in ASDEX Upgrade," *Nuclear Fusion*, vol. 50, no. 5, p. 052 003, May 2010. DOI: `10.1088/0029-5515/50/5/052003`

[48] A. Schlaich, C. Wu, I. Pagonakis, K. A. Avramidis, S. Illy, G. Gantenbein, J. Jelonnek, and M. Thumm, "Separation of thermal expansion and beam charge neutralization effects in high power 140 GHz CW gyrotrons," in *2014 IEEE 41st International Conference on Plasma Sciences (ICOPS) held with 2014 IEEE International Conference on High-Power Particle Beams (BEAMS)*, May 2014, pp. 1–1. DOI: `10.1109/PLASMA.2014.7012317`

[49] A. Schlaich, "Time-dependent spectrum analysis of high power gyrotrons," Ph.D. dissertation, Karlsruhe Institute of Technology, 2015, DOI: `10.5445/KSP/1000046919`

[50] G. G. Denisov, M. Y. Glyavin, A. E. Fedotov, and I. V. Zotova, "Theoretical and Experimental Investigations of Terahertz-Range Gyrotrons with Frequency and Spectrum Control," *Journal of Infrared, Millimeter, and Terahertz Waves*, Mar. 2020. DOI: `10.1007/s10762-020-00672-8`

[51] M. Y. Glyavin, G. G. Denisov, M. L. Kulygin, and Y. V. Novozhilova, "Stabilization of gyrotron frequency by reflection from nonresonant and resonant loads," *Technical Physics Letters*, vol. 41, no. 7, pp. 628–631, Jul. 2015. DOI: `10.1134/S106378501507007X`

[52] M. Y. Glyavin, G. G. Denisov, M. L. Kulygin, M. M. Mel'nikova, Y. V. Novozhilova, and N. M. Ryskin, "Gyrotron Frequency Stabilization by a Weak Reflected Wave," *Radiophysics and Quantum Electronics*, vol. 58, no. 9, pp. 673–683, Feb. 2016. DOI: `10.1007/s11141-016-9639-0`

[53] M. M. Melnikova, A. G. Rozhnev, N. M. Ryskin, A. V. Tyshkun, M. Y. Glyavin, and Y. V. Novozhilova, "Frequency Stabilization of a 0.67-THz Gyrotron by Self-Injection Locking," *IEEE Transactions on Electron Devices*, vol. 63, no. 3, pp. 1288–1293, Mar. 2016. DOI: `10.1109/TED.2015.2512868`

[54] H. Guo, D. Hoppe, J. Rodgers, R. Perez, J. Tate, B. Conroy, V. Granatstein, A. Bhanji, P. Latham, G. Nusinovich, L. Naiman, and S.-H. Chen, "Phase-locking of a second-harmonic gyrotron oscillator using a quasi-optical circulator to separate injection and output signals," *IEEE Transactions on Plasma Science*, vol. 23, no. 5, pp. 822–832, Oct. 1995. DOI: `10.1109/27.473201`

[55] G. Y. Golubiatnikov, A. F. Krupnov, L. V. Lubyako, A. G. Luchinin, A. B. Pavelyev, M. I. Petelin, and A. Fernandez Curto, "Gyrotron frequency control by a phase lock system," *Technical Physics Letters*, vol. 32, no. 8, pp. 650–652, Aug. 2006. DOI: `10.1134/S1063785006080037`

[56] K. A. Yakunina, A. P. Kuznetsov, and N. M. Ryskin, "Injection locking of an electronic maser in the hard excitation mode," *Physics of Plasmas*, vol. 22, no. 11, p. 113 107, Nov. 2015. DOI: `10.1063/1.4935847`

[57] V. L. Bakunin, G. G. Denisov, and Y. V. Novozhilova, "Principal Enhancement of THz-Range Gyrotron Parameters Using Injection Locking," *IEEE Electron Device Letters*, vol. 41, no. 5, pp. 777–780, May 2020. DOI: 10.1109/LED.2020.2980218

[58] M. M. Melnikova, N. V. Grigorieva, and N. M. Ryskin, "Influence of reflected or external signal on gyrotron operation," in *Fourth International Conference on Terahertz and Microwave Radiation: Generation, Detection, and Applications*, vol. 11582, SPIE, Nov. 2020, pp. 118–125. DOI: 10.1117/12.2580073

[59] N. V. Grigorieva and N. M. Ryskin, "Study of Injection Locking of a Gyrotron by Using the Modified Quasilinear Theory," in *2021 14th UK-Europe-China Workshop on Millimetre-Waves and Terahertz Technologies (UCMMT)*, Sep. 2021, pp. 1–3. DOI: 10.1109/UCMMT53364.2021.9569876

[60] P. Brücker, K. A. Avramidis, A. Marek, M. Thumm, and J. Jelonnek, "Theoretical Investigation on Injection Locking of the EU 170 GHz 2 MW TE34,19-Mode Coaxial-Cavity Gyrotron," in *2021 46th International Conference on Infrared, Millimeter and Terahertz Waves (IRMMW-THz)*, Aug. 2021, pp. 1–2. DOI: 10.1109/IRMMW-THz50926.2021.9567563

[61] F. M. Gardner, *Phaselock Techniques*. John Wiley & Sons, Ltd, Jul. 2005, ISBN: 978-0-471-43063-6. DOI: https://doi.org/10.1002/0471732699

[62] A. V. Chirkov, G. G. Denisov, and A. N. Kuftin, "Perspective gyrotron with mode converter for co- and counter-rotation operating modes," *Applied Physics Letters*, vol. 106, no. 26, p. 263 501, Jun. 2015. DOI: 10.1063/1.4923269

[63] J. Jin, G. Gantenbein, S. Illy, J. Jelonnek, and M. Thumm, "Improved Synthesis of Quasi-Optical Launchers Used in Injection Locked Gyrotrons," in *2023 24th International Vacuum Electronics Conference (IVEC)*, Apr. 2023, pp. 1–2. DOI: 10.1109/IVEC56627.2023.10157968

[64] S. E. Tsimring, *Electron Beams and Microwave Vacuum Electronics*. John Wiley & Sons, Ltd, Apr. 2006, ISBN: 978-0-470-05376-8. DOI: 10.1002/0470053763

[65] M. V. Kartikeyan, E. Borie, and M. K. A. Thumm, *Gyrotrons: High-Power Microwave and Millimeter Wave Technology* (Advanced Texts in Physics). Springer Berlin Heidelberg, 2004, ISBN: 978-3-642-07288-8. DOI: 10.1007/978-3-662-07637-8

[66] J. Forshaw and G. Smith, *Dynamics and Relativity* (Manchester Physics Series). Wiley, 2009, ISBN: 978-0-470-72152-0

[67] G. S. Nusinovich, *Introduction to the Physics of Gyrotrons*. JHU Press, Aug. 2004, 366 pp., ISBN: 978-0-8018-7921-0

[68] V. N. Manuilov and S. A. Polushkina, "Behavior of helical electron beams in gyrotrons with high pitch factors," *Radiophysics and Quantum Electronics*, vol. 52, no. 10, pp. 714–721, Oct. 2009. DOI: 10.1007/s11141-010-9179-y

[69] C. Edgecombe, *Gyrotron Oscillators*. London: CRC Press, Oct. 2019, 448 pp., ISBN: 978-0-429-08105-7. DOI: 10.1201/9781482272369

[70] F. F. Chen, *Introduction to Plasma Physics and Controlled Fusion*. Springer International Publishing, 2016, ISBN: 978-3-319-22309-4. DOI: 10.1007/978-3-319-22309-4

[71] A. L. Gol'denberg and M. I. Petelin, "The formation of helical electron beams in an adiabatic gun," *Radiophysics and Quantum Electronics*, vol. 16, no. 1, pp. 106–111, Jan. 1973. DOI: 10.1007/BF01080801

[72] H. Busch, "Berechnung der Bahn von Kathodenstrahlen im axialsymmetrischen elektromagnetischen Felde," *Annalen der Physik*, vol. 386, no. 25, pp. 974–993, 1926. DOI: 10.1002/andp.19263862507

[73] L. Groening, C. Xiao, and M. Chung, "Extension of Busch's theorem to particle beams," *Physical Review Accelerators and Beams*, vol. 21, no. 1, p. 014 201, Jan. 2018. DOI: 10.1103/PhysRevAccelBeams.21.014201

[74] I. G. Pagonakis, K. A. Avramidis, G. Gantenbein, T. Rzesnicki, A. Samartsev, and J. Jelonnek, “Magnetic field profile analysis for gyrotron experimental investigation,” *Physics of Plasmas*, vol. 24, no. 3, p. 033 102, Mar. 2017. DOI: 10.1063/1.4977460

[75] G. Dammertz, “Vacuum requirements in high power microwave tubes,” *Vacuum*, vol. 46, no. 8, pp. 785–788, Aug. 1995. DOI: 10.1016/0042-207X(95)00039-9

[76] B. Piosczyk, “Compensation of the beam space charge and consequences for the design of a gyrotron,” in *15th International Conference on Infrared and Millimeter Waves*, vol. 1514, SPIE, 1990, pp. 507–509

[77] I. G. Pagonakis, J.-P. Hogge, S. Alberti, K. A. Avramides, and B. Piosczyk, “Preliminary numerical study of the beam neutralization effect in the EU 170 GHz, 2 MW coaxial gyrotron,” in *2008 IEEE 35th International Conference on Plasma Science*, Jun. 2008, pp. 1–1. DOI: 10.1109/PLASMA.2008.4590838

[78] A. Schlaich, C. Wu, I. G. Pagonakis, K. Avramidis, S. Illy, G. Gantenbein, J. Jelonnek, and M. Thumm, “Frequency-Based Investigation of Charge Neutralization Processes and Thermal Cavity Expansion in Gyrotrons,” *Journal of Infrared, Millimeter, and Terahertz Waves*, vol. 36, no. 9, pp. 797–818, Sep. 2015. DOI: 10.1007/s10762-015-0177-1

[79] J. Jelonnek, F. Albajar, S. Alberti, *et al.*, “From Series Production of Gyrotrons for W7-X Toward EU-1 MW Gyrotrons for ITER,” *IEEE Transactions on Plasma Science*, vol. 42, no. 5, pp. 1135–1144, May 2014. DOI: 10.1109/TPS.2014.2301839

[80] K. R. Chu, “The electron cyclotron maser,” *Reviews of Modern Physics*, vol. 76, no. 2, pp. 489–540, May 2004. DOI: 10.1103/RevModPhys.76.489

[81] S. Ruess, “Pushing the KIT 2 MW Coaxial-Cavity Short-Pulse Gyrotron Towards a DEMO Relevant Design,” Ph.D. dissertation, Karlsruhe Institute of Technology, 2020, DOI: 10.5445/KSP/1000117846

[82] E. L. Murphy and R. H. Good, "Thermionic Emission, Field Emission, and the Transition Region," *Physical Review*, vol. 102, no. 6, pp. 1464–1473, Jun. 1956. DOI: 10.1103/PhysRev.102.1464

[83] J. A. Eichmeier and M. K. Thumm, Eds., *Vacuum Electronics: Components and Devices*, Springer Berlin, Heidelberg, 2008, ISBN: 978-3-540-71928-1. DOI: 10.1007/978-3-540-71929-8

[84] A. Kumar, U. Singh, N. Kumar, N. Kumar, V. Vyas, and A. K. Sinha, "Design of a Triode Magnetron Injection Gun for a 1-MW 170-GHz Gyrotron," *IEEE Transactions on Plasma Science*, vol. 40, no. 9, pp. 2126–2132, Sep. 2012. DOI: 10.1109/TPS.2012.2205710

[85] K. Kajiwara, Y. Oda, A. Kasugai, K. Takahashi, and K. Sakamoto, "Development of Dual-Frequency Gyrotron with Triode Magnetron Injection Gun," *Applied Physics Express*, vol. 4, no. 12, p. 126 001, Nov. 2011. DOI: 10.1143/APEX.4.126001

[86] D. M. Pozar, *Microwave Engineering*, 4th Edition. Wiley, 2011, ISBN: 978-1-118-21363-6

[87] S. Kern, "Numerische Simulation der Gyrotron- Wechselwirkung in koaxialen Resonatoren," Ph.D. dissertation, Fakultät für Elektrotechnik, Universität Karlsruhe, 1996, DOI: 10.5445/IR/55396

[88] J. H. Flamm, "Diffraction and Scattering in Launchers of Quasi-Optical Mode Converters for Gyrotrons," Ph.D. dissertation, Karlsruhe Institute of Technology, 2012, ISBN: 9783866448223

[89] J. Jin, G. Gantenbein, J. Jelonnek, T. Rzesnicki, and M. Thumm, "Development of Mode Conversion Waveguides at KIT," *EPJ Web of Conferences*, vol. 87, p. 04 003, 2015. DOI: 10.1051/epjconf/20158704003

[90] M. Thumm, "MPACVD-diamond windows for high-power and long-pulse millimeter wave transmission," *Diamond and Related Materials*, Proceedings of the 7th International Conference on New Diamond Science and Technology(ICNDST-7), vol. 10, no. 9, pp. 1692–1699, Sep. 2001. DOI: 10.1016/S0925-9635(01)00397-1

[91] H.-U. Nickel, "Plane transverse waveguide windows: survey of formulas for reflection, transmission, and absorption," in *16th International Conference on Infrared and Millimeter Waves*, vol. 1576, Proc. SPIE, Oct. 1991, pp. 444–445. DOI: 10.1117/12.2297936

[92] H.-U. Nickel, "Hochfrequenztechnische Aspekte zur Entwicklung rückwirkungsarmer Ausgangsfenster für Millimeterwellengyrotrons hoher Leistung," Ph.D. dissertation, Universität Karlsruhe, 1995, DOI: 10.5445/IR/46595

[93] G. Dammertz, S. Illy, B. Piosczyk, M. Schmid, and D. Bariou, "Collector sweeping systems for high power gyrotrons," in *2005 Joint 30th International Conference on Infrared and Millimeter Waves and 13th International Conference on Terahertz Electronics*, vol. 1, Sep. 2005, 293–294 vol. 1. DOI: 10.1109/ICIMW.2005.1572524

[94] M. Schmid, S. Illy, G. Dammertz, V. Erckmann, and M. Thumm, "Transverse field collector sweep system for high power CW gyrotrons," *Fusion Engineering and Design*, Proceedings of the 24th Symposium on Fusion Technology, vol. 82, no. 5, pp. 744–750, Oct. 2007. DOI: 10.1016/j.fusengdes.2007.06.008

[95] H. Braune, V. Erckmann, S. Illy, H. P. Laqua, G. Michel, F. Noke, and F. Purps, "Transverse field collector sweeping for the W7-X gyrotrons — Modulation techniques," in *2009 34th International Conference on Infrared, Millimeter, and Terahertz Waves*, Sep. 2009, pp. 1–2. DOI: 10.1109/ICIMW.2009.5325739

[96] B. Piosczyk, C. Iatrou, G. Dammertz, and M. Thumm, "Single-stage depressed collectors for gyrotrons," *IEEE Transactions on Plasma Science*, vol. 24, no. 3, pp. 579–585, Jun. 1996. DOI: 10.1109/27.532940

[97] C. Wu, I. G. Pagonakis, K. A. Avramidis, G. Gantenbein, S. Illy, M. Thumm, and J. Jelonnek, "Gyrotron multistage depressed collector based on E × B drift concept using azimuthal electric field. I. Basic design," *Physics of Plasmas*, vol. 25, no. 3, p. 033 108, Mar. 2018. DOI: 10.1063/1.5016296

[98] B. Ell, C. Wu, G. Gantenbein, S. Illy, I. G. Pagonakis, T. Rzesnicki, S. Stanculovic, M. Thumm, J. Weggen, and J. Jelonnek, “Design of a Two-Stage Depressed Collector for Continuous Wave Operation of MW-Class Gyrotrons,” presented at the 23rd International Vacuum Electronics Conference (IVEC 2022), Online, 25.04.2022 – 29.04.2022, 2022

[99] H. De Bellescize, “La reception synchrone,” *L’Onde Electrique*, vol. 11, pp. 230–240, 1932

[100] B. Boashash, “Estimating and interpreting the instantaneous frequency of a signal. I. Fundamentals,” *Proceedings of the IEEE*, vol. 80, no. 4, pp. 520–538, Apr. 1992. DOI: `10.1109/5.135376`

[101] N. Kamal, S. Al-Sarawi, and D. Abbott, “An accurate analytical spur model for an integer-N phase-locked loop,” in *2012 4th International Conference on Intelligent and Advanced Systems (ICIAS2012)*, vol. 2, Jun. 2012, pp. 659–664. DOI: `10.1109/ICIAS.2012.6306096`

[102] P.-E. Su and S. Pamarti, “Fractional-N Phase-Locked-Loop-Based Frequency Synthesis: A Tutorial,” *IEEE Transactions on Circuits and Systems II: Express Briefs*, vol. 56, no. 12, pp. 881–885, Dec. 2009. DOI: `10.1109/TCSII.2009.2035258`

[103] S. Soliman, F. Yuan, and K. Raahemifar, “An overview of design techniques for CMOS phase detectors,” in *2002 IEEE International Symposium on Circuits and Systems. Proceedings (Cat. No.02CH37353)*, vol. 5, May 2002, pp. V–V. DOI: `10.1109/ISCAS.2002.1010739`

[104] M. Soyuer and R. Meyer, “Frequency limitations of a conventional phase-frequency detector,” *IEEE Journal of Solid-State Circuits*, vol. 25, no. 4, pp. 1019–1022, Aug. 1990. DOI: `10.1109/4.58298`

[105] G. Ascheid and H. Meyr, “Cycle Slips in Phase-Locked Loops: A Tutorial Survey,” *IEEE Transactions on Communications*, vol. 30, no. 10, pp. 2228–2241, Oct. 1982. DOI: `10.1109/TCOM.1982.1095423`

[106] N. S. Ginzburg, A. S. Sergeev, and I. V. Zotova, "Time-domain self-consistent theory of frequency-locking regimes in gyrotrons with low-Q resonators," *Physics of Plasmas*, vol. 22, no. 3, p. 033 101, Mar. 2015. DOI: `10.1063/1.4913672`

[107] K. Koppenburg, G. Dammertz, M. Kuntze, B. Piosczyk, and M. Thumm, "Fast frequency-step-tunable high-power gyrotron with hybrid-magnet-system," *IEEE Transactions on Electron Devices*, vol. 48, no. 1, pp. 101–107, Jan. 2001. DOI: `10.1109/16.892175`

[108] R. Hirose, T. Kamikado, Y. Okui, H. Miyata, K. Shibutani, O. Ozaki, and K. Sakamoto, "Development of 7 T Cryogen-free Superconducting Magnet for Gyrotron," *IEEE Transactions on Applied Superconductivity*, vol. 18, no. 2, pp. 920–923, Jun. 2008. DOI: `10.1109/TASC.2008.922296`

[109] C. Wu, G. Aiello, K. A. Avramidis, *et al.*, "Basic design considerations for a frequency step-tunable electron cyclotron wave system to suppress NTMs in DEMO," *Fusion Engineering and Design*, vol. 173, p. 112 931, Dec. 2021. DOI: `10.1016/j.fusengdes.2021.112931`

[110] E. M. Khutoryan, T. Idehara, A. N. Kuleshov, and K. Ueda, "Gyrotron Output Power Stabilization by PID Feedback Control of Heater Current and Anode Voltage," *Journal of Infrared, Millimeter, and Terahertz Waves*, vol. 35, no. 12, pp. 1018–1029, Dec. 2014. DOI: `10.1007/s10762-014-0105-9`

[111] K. Sakamoto, A. Kasugai, R. Minami, K. Takahashi, and N. Kobayashi, "Development of Long Pulse and High Power 170GHz Gyrotron," *Journal of Physics: Conference Series*, vol. 25, no. 1, p. 8, Jan. 2005. DOI: `10.1088/1742-6596/25/1/002`

[112] G. Michel and J. Sachtleben, "An integrated gyrotron controller," *Fusion Engineering and Design*, Proceedings of the 26th Symposium of Fusion Technology (SOFT-26), vol. 86, no. 6, pp. 776–779, Oct. 2011. DOI: `10.1016/j.fusengdes.2010.12.013`

[113] K. A. Avramides, I. G. Pagonakis, C. T. Iatrou, and J. L. Vomvoridis, "EURIDICE: A code-package for gyrotron interaction simulations and cavity design," *EPJ Web of Conferences*, vol. 32, p. 04 016, 2012. DOI: 10.1051/epjconf/20123204016

[114] S. Illy, J. Zhang, and J. Jelonnek, "Gyrotron electron gun and collector simulation with the ESRAY beam optics code," in *2015 IEEE International Vacuum Electronics Conference (IVEC)*, Apr. 2015, pp. 1–2. DOI: 10.1109/IVEC.2015.7223779

[115] P. Brand and G. A. Mueller, "Circuit design and simulation of a HV-supply controlling the power of 140 GHz 1 MW gyrotrons for ECRH on W7-X," *Fusion Engineering and Design*, 22nd Symposium on Fusion Technology, vol. 66-68, pp. 573–577, Sep. 2003. DOI: 10.1016/S0920-3796(03)00133-9

[116] H. Braune, P. Brand, R. Krampitz, W. Leonhardt, D. Mellein, G. Michel, G. Mueller, J. Sachtleben, M. Winkler, and the W7-X ECRH teams at IPP, IPF and FZK, "HV-system for CW-gyrotrons at W7-X and the relevance for ITER," *Journal of Physics: Conference Series*, vol. 25, pp. 56–65, Jan. 2005. DOI: 10.1088/1742-6596/25/1/008

[117] K. Baltzis, "The FEMM Package: A Simple, Fast, and Accurate Open Source Electromagnetic Tool in Science and Engineering.," *Journal of Engineering Science & Technology Review*, vol. 1, no. 1, 2008

[118] The MathWorks Inc., *MATLAB version: 9.13.0 (R2022b)*, Natick, Massachusetts, United States, 2022

[119] Cadence Design Systems Inc., *PSpice*, San Jose, California, United States, 2022

[120] N. Tomljenovic, W. Schminke, and H. G. Mathews, "Solid-State DC Power Supplies for Gyrotrons and NBI Sources," in *Fusion Technology 1992*, Oxford: North-Holland, Jan. 1993, pp. 952–956, ISBN: 978-0-444-89995-8. DOI: 10.1016/B978-0-444-89995-8.50184-3

[121] D. Moseev, M. Stejner, T. Stange, *et al.*, "Collective Thomson scattering diagnostic at Wendelstein 7-X," *Review of Scientific Instruments*, vol. 90, no. 1, p. 013 503, Jan. 2019. DOI: `10.1063/1.5050193`

[122] D. Moseev, H. P. Laqua, T. Stange, *et al.*, "Collective Thomson Scattering Diagnostic for Wendelstein 7-X at 175 GHz," *Journal of Instrumentation*, vol. 15, no. 5, p. C05035, May 2020. DOI: `10.1088/1748-0221/15/05/C05035`

[123] J. W. Oosterbeek, N. Chaudhary, M. Hirsch, U. Höfel, and R. C. Wolf, "Assessment of ECH stray radiation levels at the W7-X Michelson Interferometer and Profile Reflectometer," *EPJ Web of Conferences*, vol. 203, p. 03 010, 2019. DOI: `10.1051/epjconf/201920303010`

[124] L. Krier, I. G. Pagonakis, K. A. Avramidis, G. Gantenbein, S. Illy, J. Jelonnek, J. Jin, H. P. Laqua, A. Marek, D. Moseev, and M. Thumm, "Theoretical investigation on possible operation of a 140 GHz 1 MW gyrotron at 175 GHz for CTS plasma diagnostics at W7-X," *Physics of Plasmas*, vol. 27, no. 11, p. 113 107, Nov. 2020. DOI: `10.1063/5.0022151`

[125] J. G. Pagonakis and J. L. Vomvoridis, "The self-consistent 3D trajectory electrostatic code ARIADNE for gyrotron beam tunnel simulation," in *Infrared and Millimeter Waves, Conference Digest of the 2004 Joint 29th International Conference on 2004 and 12th International Conference on Terahertz Electronics, 2004.*, Sep. 2004, pp. 657–658. DOI: `10.1109/ICIMW.2004.1422262`

[126] A. Marek, J. Jin, J. Jelonnek, M. Thumm, and A.-S. Müller, "Development of an advanced vector analysis code for simulation of electromagnetic fields in quasi-optical systems of high power gyrotrons," in *2017 Eighteenth International Vacuum Electronics Conference (IVEC)*, Apr. 2017, pp. 1–2. DOI: `10.1109/IVEC.2017.8289599`

[127] A. A. Bogdashov, A. V. Chirkov, G. G. Denisov, D. V. Vinogradov, A. N. Kuftin, V. I. Malygin, and V. E. Zapevalov, "Mirror synthesis for gyrotron quasi-optical mode converters," *International Journal of Infrared and Millimeter Waves*, vol. 16, no. 4, pp. 735–744, Apr. 1995. DOI: 10.1007/BF02066633

[128] J. Jin, B. Piosczyk, M. Thumm, T. Rzesnicki, and S. Zhang, "Quasi-Optical Mode Converter/Mirror System for a High-Power Coaxial-Cavity Gyrotron," *IEEE Transactions on Plasma Science*, vol. 34, no. 4, pp. 1508–1515, Aug. 2006. DOI: 10.1109/TPS.2006.877627

[129] Κ. Αβραμίδης, "Σχεδίαση και προσομοίωση ομοαξονικών γυροτρονίων (με έμφαση στη λειτουργία δεύτερης αρμονικής)," Ph.D. dissertation, Εθνικό Μετσόβιο Πολυτεχνείο (ΕΜΠ). Σχολή Ηλεκτρολόγων Μηχανικών και Μηχανικών Υπολογιστών. Τομέας Ηλεκτρομαγνητικών Εφαρμογών, Ηλεκτροοπτικής και Ηλεκτρονικών Υλικών, 2006, DOI: 10.12681/eadd/16296

[130] F. Wilde, "Automated Mode Recovery and Electronic Stability Control for Wendelstein 7-X Gyrotrons," Ph.D. dissertation, Karlsruhe Institute of Technology, 2021, DOI: 10.5445/IR/1000137957

[131] A. Schlaich, G. Gantenbein, S. Illy, J. Jelonnek, and M. Thumm, "Observation of Discrete Frequency Hopping in MW-Class Gyrotrons During Long-Pulse Operation," *IEEE Transactions on Electron Devices*, vol. 62, no. 9, pp. 3049–3055, Sep. 2015. DOI: 10.1109/TED.2015.2455023